MOLECULAR DYNAMICS SIMULATIONS OF NONCONTACT ATOMIC FORCE MICROSCOPY AND OF RELEVANT SILICON SYSTEMS

INAUGURALDISSERTATION

ZUR
ERLANGUNG DER WÜRDE EINES DOKTORS DER PHILOSOPHIE
VORGELEGT DER
PHILOSOPHISCH-NATURWISSENSCHAFTLICHEN FAKULTÄT
DER UNIVERSITÄT BASEL

VON
ABDUXUKUR ABDURIXIT
AUS ÜRÜMQI, XINJIANG, V. R. CHINA

UNI
BASEL

BASEL, 2000

Genehmigt von der Philosophisch-Naturwissenschaftlichen Fakultät
auf Antrag der Herren:

Prof. Dr. E. Meyer
Dr. A. Baratoff

Basel, den 20. Juni 2000

Prof. Dr. Andreas Zuberbühler, Dekan

Contents

List of Figures

List of Tables

Foreword

This thesis is an account of work carried out by the author during his PhD study at the Department of Physics and Astronomy, University of Basel during the period of December, 1997 to June 2000 thanks to financial support provided by the Swiss National Foundation for Scientific Research under the special program NFP36 "Nanosciences".

First of all, I thank Prof. Dr. Güntherodt and Prof. Dr. E. Meyer for giving me an opportunity to work in their group, for their support in scientific research and other aspects, and especially my thesis supervisor Dr. A. Baratoff for his continuous support and for numerous discussions.

This work could have not been performed without the tight-binding(TB) and molecular dynamics(MD) computer codes initially developed and provided by Dr Giulia Galli and Dr Thomas Bonner and their valuable assistance in the initial stage of this work.

During my stay I have benefited enormously from discussions with many colleagues, friends and collaborators. In particularly I am grateful to Alexandre Bouhelier, Dr Laurent Pizzagalli, Rainer Härle, Dr Mark Lantz, PD Dr H.-J. Hug, Dr Roland Bennewitz and Martin Guggisberg.

I also would like to thank all other colleagues in the group of Profs. H.-J. Güntherodt and E. Meyer.

I thank the Computing Center of Basel University for providing me access to their "super computer" on which the TB computations were done.

My special thanks also go to our secretary Jacqueline Vetter for taking care of administrative matters. I also thank our Institute secretaries Elisabeth Holdermann, Esther Meyer, Astrid Kalt und Barbara Kammermann.

This thesis is dedicated to my wife Gülnar and our son Waris for their support and encouragement during my study abroad. I hope that the final result compensates to some extent for the last four years that they spent on their own while I was pursuing my graduate studies in Trieste and Basel.

Most of the MD computations were performed on two Pentium PC's acquired by our group.

I also wish to thank numerous providers of free advice and free software on the Internet, the people behind RedHat Linux, in particular, for greatly facilitating a huge variety of bookkeeping, programming and computational tasks.

Introduction

After the invention of the scanning tunneling microscope (STM), many scanning probe methods have been developed and applied in many areas to study optical, mechanical, electronic, magnetic, chemical, biological properties of materials. Scanning force microscopy (SFM) is one the most widespread scanning probe methods.

The history of Atomic Force Microscopy (AFM) started in 1986 by the pioneering work of Binnig, Quate and Gerber [1]. AFM is a tool which allows routine investigation of surface structures by probing the spatial variations of the total force between a sharp tip and a sample. However, images taken in the repulsive *contact mode* were not able to resolve individual surface defects since the tip sample interaction involves many surface and tip atoms. Contact AFM can only resolve the periodicity of an ordered lattice; it was not able to image reactive surfaces since the surface structure was destroyed. Atomic resolution was finally obtained by maintaining a small constant frequency shift Δf via feedback control of the cantilever perpendicular displacement [2, 3]. This shift can be measured very accurately using frequency demodulation [4]. Since then, many investigators have obtained atomically-resolved images of the Si(111)-7×7 surface in ultra high vacuum (UHV) using large-amplitude dynamic force microscopy (DFM) under various feedback conditions and different tip material [5, 6, 7, 8, 9, 10].

Owing to its distinctive features, the surface in question is an ideal benchmark sample for validating scanning probe methods capable of resolving atomic-scale structures. The DFM experiments indeed revealed the salient features of the so-called DAS reconstruction model [11, 12]. The AFM contrast on the Si(111)-7×7 surface can be attributed to a partially filled dangling bond on the apex atom of the sharp tip interacting with nearby dangling bonds on the top layer adatoms. This interpretation was strongly reinforced by the ab-inition calculations of Perez et al [13]. The validity of the interpretation has been confirmed by recent experiments in our institute [14]; the range and magnitude of the short range interaction potential above the adatoms is in good agreement with the chemical bonding force calculated by Perez et al. This work indicated that the observed contrast is due to incipient chemical bonding and is attained when the tip-sample interaction is attractive, before the maximum attractive tip-adatom force is reached, i.e. without irreversible deformations or material transfer. For the sake of accuracy, we restrict the commonly used name *non-contact* AFM to experiments performed under such conditions.

Despite the increasing use of DFM and a growing body of experimental and theoretical work, the mechanisms which give rise to the observed atomic scale contrast are still not completely understood. One reason for this is the scarcity of direct comparisons between theoretical and experimental work. Direct comparisons are complicated by the fact that most theoretical work has focused on the calculation of tip-sample interaction forces, whereas experimentally, forces are usually only indirectly measured. The measured frequency shift generally results from short range as well as long-range forces such as van der Waals and electrostatic forces. The strength of these long-range interactions depends on the microscopic tip shape which varies between experiments and is generally not known, thus complicating comparisons. Giessibl [15] was the first to relate the frequency shift to distance-dependent interaction forces, this providing a basis for comparison. The interpretation of image contrast is still not straightforward because the relative contribution of short and long-range forces to the frequency shift is not known a priori.

In this thesis, I discuss computer simulations of important silicon surfaces, of silicon model tips and finally of atomic force microscopy of reconstructed silicon surface using model silicon tips.

The first chapter describes the computational techniques employed: classical and linear scaling tight-binding(TB) molecular dynamics(MD) methods, integration and temperature control algorithms.

The second chapter deals with calculations performed with the linear scaling tight-binding method. Representative structures of common Si surfaces, namely 2x1 and 5x5 reconstructions of the (111) surface and the c(4x2) reconstruction on the (001) surface have been studied to test this rather novel method. We also studied the main properties of the ubiquitous type-C defect on that surface. Finally we applied the method to [001] oriented pyramidal silicon clusters to model an experimental AFM tip. We used relaxation and simulated annealing techniques to investigate the apex structure and thermal stability of such tips. The tight-binding method yielded encouraging results, comparable in quality to those obtained by more accurate methods on known systems. However, despite speedup attempts it proved to be too time-consuming to perform the numerous computations required to simulate a tip interacting with and displaced relative to the surface of a sample under various conditions.

The third chapter deals with classical molecular dynamics simulations to which we resorted in order to understand many issues raised by recent nc-AFM experiments on the famous Si(111)-7x7 surface, like importance of the tip shape and of different interactions on the observed scans in various operation modes, e.g. constant height, constant force, or constant frequency shift. By oscillating the tip above selected surface sites valuable insights are obtained into possible energy dissipation mechanisms in nc-AFM. Finally attempts to identify controlled manipulation paths for an added Si atom on the Si(111)-7x7 surface are discussed.

The last chapter summarizes conclusions based on results described in the preceding chapters.

Appendix A describes the parametrized matrix elements at the heart of the empirical tight-binding of covalently bonded carbon or silicon-based systems.

Appendices B and D describe the input parameters in the tight-binding code and all options of the classical MD program, including new ones implicated in the course of our work.

In Appendix C, the influence of various factors affecting the rather complex O(N) tight-binding computations is discussed.

Chapter 1

Simulation Techniques

1.1 Introduction

Most physical systems are collections of interacting objects. For example, a drop of water is a collection of more than 10^{21} water molecules. In general, there is no analytical solution for an interacting system with more than two objects, the alternative is to use numerical computer simulation techniques.

There are different kinds of computer simulation methods, the most popular techniques being *molecular dynamics* (MD) and *Monte-Carlo* (MC).

In this thesis we use variants of the molecular dynamics method, first dealing with generally applicable aspects[16].

1.1.1 Periodic Boundary Conditions

The problem of computationally accessible system size can be partly overcome by implementing *periodic boundary conditions*(PBC). A box with planar boundaries is replicated throughout space to form an infinite lattice. In the course of the simulations, as an atom moves in the original box, its periodic images in each of the neighboring boxes then move exactly the same way. Thus, as an atom leaves the central box, one of its images must enter through the opposite face. There are no real walls at the boundary of the central box, and no surface atoms in the case of bulk. A two-dimensional illustration of such a system is shown in Fig. 1.1.

The optimum size of the simulation box depends both on the range of the interatomic potential and the phenomenon under investigation. If the size of the box is larger than the cut-off radius of the interatomic potential(see next subsection), then most atoms will not 'sense' the influence of the periodic images.

In simulations of surface properties slabs of finite thickness are used with periodic boundary conditions applied in two orthogonal directions parallel to the slab surface.

1.1.2 Potential Truncation

As mentioned above, the size of the box has to be larger than the cut-off radius of the interaction potential. The question is how to define this cut-off radius.

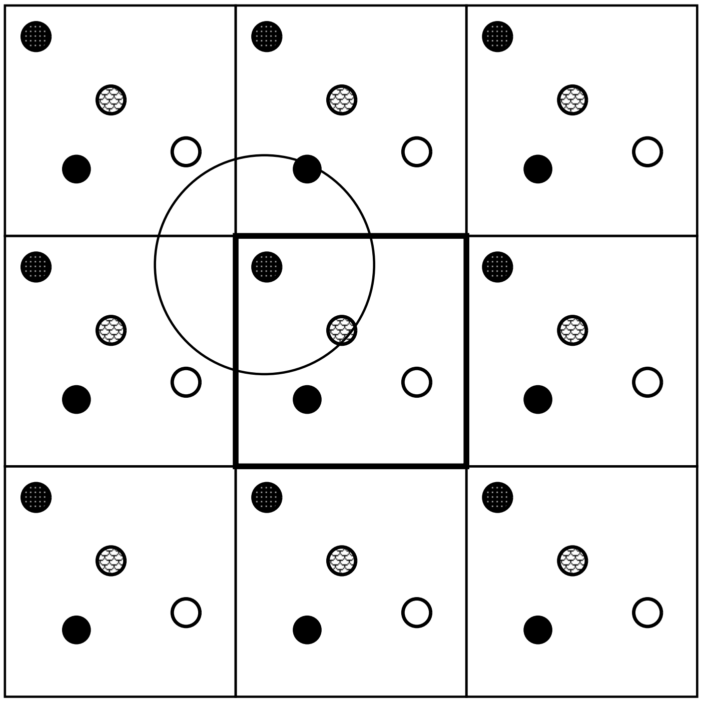

Figure 1.1: Schematic view of periodic boundary conditions of two-dimensional system and spherical interaction cut-off interaction region

In order to calculate the interaction energy of a particular atom, we consider the interactions between all atoms in a cubic simulation box of size $L \times L \times L$ and the atom which we consider. If for simplicity we assume pairwise additivity, there are N-1 terms in the sum. In principle, this sum includes all images of the atom, i.e. has an infinite number of terms. But if the interaction has a certain decay length, we can make an approximation to the summation. If we consider each atom at the center of a box which has the same shape and same size, then this atom interacts only with the atoms in this region and just a few periodic images. In this so-called *minimum image convention* the calculation of the potential energy due to pairwise additive interactions involves only $\frac{1}{2}N(N-1)$ terms. This can still be a time-consuming calculation for a system of 1000 atoms. A further approximation can improve this situation. The main contribution to the potential and force comes from neighboring atoms of the atom which we are considering, so that a spherical cutoff is justified beyond a certain radius r_c; the interaction is neglected in the region $r \geq r_c$. In this way the number of active neighbors reduced by a factor of $4\pi r_c^3/3L^3$. Of course, the cut-off radius has to be smaller than $\frac{1}{2}L$ in order to satisfy the minimum image convention and the spherical cut-off should have small perturbation.

Even a reasonable cut-off produces truncation errors that manifest themselves as unphysical noise in the forces and extra fluctuation and/or drift in the total energy of the system. This creates problems, especially in MD simulations where energy conservation is required. One way to avoid these errors is to multiply the potential by a switching function, for instance, a third order polynomial $P(x)$ without discontinuities at the first and second cutoff distances r_1 and r_2 as shown in Fig. 1.2. By using such a switching function the potential is smooth and energy conservation is preserved up to the accuracy of the integration algorithm employed.

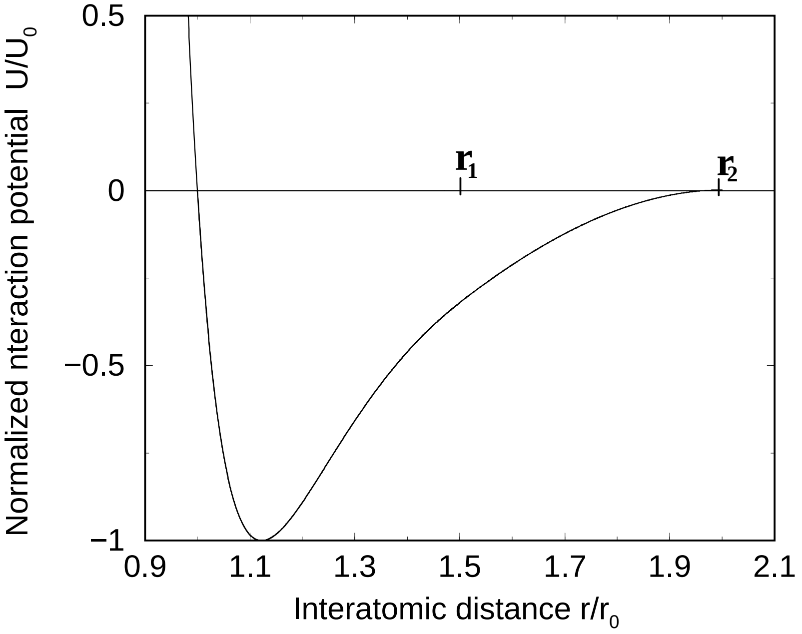

Figure 1.2: Interaction potential forced to zero smoothly between r_1 and r_2

1.1.3 Starting up

In a molecular dynamics simulation, the numerical integration of Newton's equation of motion to the next step produces new atomic positions and velocities from previous step values. It is expedient to construct an initial configuration so that the system can quickly relax and distribute the velocities during the equilibration period.

How long should the equilibration period be? This depends on the interaction, the density and temperature of the system, as well as on the particular starting configuration. The more improbable the initial state, generally the longer one must run the simulation before retaining configurations for the calculating unbiased average properties. It is general practice to monitor a few properties, such as the system energy, to determine when the system has equilibrated. From an initial high-energy, low-probability state of the system, the energy will decrease until it levels off and fluctuates about the equilibrium value. In the case of an imposed uniform or periodic energy transfer from a subsystem to a second subsystem, the internal energy of the latter will rather increase or decrease linearly with time on the average.

Suppose that we have saved a configuration from a previous simulation for the exact same starting conditions. If we use this configuration as a starting point for the next simulation, we can begin computing property averages immediately because we know that the probability of that configuration is adequately high. After all, it was generated from a simulation of finite length. If on the other hand, we arbitrarily construct an initial configuration, its probability may not be very high. If we include that configuration in our averages, the results will be biased because the simulations are usually not run long enough to appropriately weight a low probability state.

1.1.3.1 Initial positions

Initial coordinates can be set up according to some known properties of the system we are going to study using experimental or theoretical atomic bulk spacing if there are no previous calculations under similar conditions. The simulation is started right after this initialized system is placed in an appropriate simulation cell defining the periodic boundary conditions applied and enough vacuum space beyond the potential cut-off radius if surface properties are going be studied.

1.1.3.2 Initial velocities

The Newtonian equations of motion used for molecular dynamics have the property that the total linear momentum of the particles is a constant of the motion. Thus, if the particles are initialized with a non-zero total linear momentum, they will retain this throughout the duration of the simulation thus generating a net flow. While there is nothing in principle wrong with this, it can lead to misleading results if, for example, one tries to determine the temperature of the system simply by calculating the average kinetic energy of the particles, because this kinetic energy will include a contribution from the net flow. Hence, it is best to initialize the velocities so that the net linear momentum of the particles is zero. Another way is to ensure that the center-of-mass velocity is zero. A typical method for initializing velocities is to give all the particles random velocities in the x, y, and z directions by choosing random numbers from the classical Maxwell distribution

$$\rho(v_{i\alpha}) = (m_i/2\pi k_B T)^{1/2} e^{-\frac{1}{2}m_i v_{i\alpha}^2/k_B T}$$

where $\rho(v_{i\alpha})$ is the probability density for velocity component $\alpha = x$, y or z. The center of mass velocity is computed and then subtracted from the velocity of each molecule. The velocities are then adjusted so that the average kinetic energy matches that of a prescribed temperature T, but it will not be even approximately maintained unless the initial positions are consistent with a state close to thermodynamic equilibrium.

1.2 Molecular Dynamics with Empirical Potentials

In molecular dynamics, all atoms are treated as classical, and effects of electronic structure are absorbed in empirical interaction potentials fitted to chosen properties in the state of interest(crystal, liquid, gas, etc). An adequate description is usually limited to small deviations from that state.

1.2.1 Linked-cell method

In the inner loops of a molecular dynamics program, we consider an atom i and loop over N atoms j satisfying the minimum image convention. If atoms are separated by a distance greater than the potential cutoff, the program skips to the end of the inner loop, thus avoiding expensive calculations, and considers another neighbor. In this method, the time to examine all pair separations is proportional to N^2. The computational speed can be improved by maintaining a list of the neighbors of a particular atom, which is updated at intervals. Between updates of the neighbor list, the program does not check through all the j atoms, but just those appearing on the list. This saves time in looping through j, checking minimum images, calculating and checking r_{ij}^2 against the cutoff, for all those particles not on the list.

As the number of the atoms in the simulated system increases towards 1000, the above neighbor list becomes too large to store. An alternative way to keep track of neighbours is the linked cell method[16]. In the case of two-dimensional slab, the rectangular simulation box is subdivided into a regular lattice of $L \times M$ cells such that the size of each cell is larger than twice the cutoff radius. Then there are approximately $N_c = N/LM$ atoms in each cell. If we keep a separate list for each cell, the searching process is restricted to that cell and mirror images in the neighboring cells because of the minimum image convention. Then the search operation involves $4.5NN_c$ steps by avoiding double counting. This is the key factor to achieve *linear* or so-called *O(N) scaling* of the computational time with the number of atoms.

1.2.2 Empirical Potentials for Silicon

Any potential energy function Φ describing interactions among N identical particles can quite generally be resolved into one-body, two-body, three-body, etc. contributions as follows:

$$\Phi(1,\ldots\ldots,N) = \sum_i v_1(i) + \sum_{i>j} v_2(i,j) + \sum_{i>j>k} v_3(i,j,k) + \cdots\cdots + v_N(1,\ldots\ldots,N) \tag{1.1}$$

For this representation to be useful it is necessary that the component functions v_n converge quickly to zero with increasing n. Although valid for most substances, as suggested by the success of chemical bonding concepts, a proper description of covalently bonded materials, silicon in particular, must reflect bond directionality, i.e. at least include three-body interactions.

The single particle potential v_1 normally describes walls and external forces to which the system is subject. These will be neglected for the time being, so that the expansion in Eq.(1.1) begins with the pair interaction term v_2.

An empirical potential is an explicit analytical expression describing the potential energy of interaction between atoms. There are many empirical potentials available for silicon; the most popular ones are compared in Ref. [17]. Here we only briefly introduce a few relevant ones for our calculations.

1.2.2.1 Lennard-Jones

Lennard-Jones potential [18] has been applied to describe phase transitions of noble gases and other model systems. It is a simple two-body interaction characterized by two physical meaningful parameters,

$$v_{LJ} = -4\varepsilon[(\sigma/r_{ij})^{12} - (\sigma/r_{ij})^{6}]$$

Here r_{ij} is the interatomic spacing between atoms i and j. The parameter ε is the minimal potential energy at the equilibrium distance $2^{1/6}\sigma$ and σ is the characteristic range of the interaction. Although it is a simple and attractive potential for simulations, such a potential is not adequate for covalent materials like silicon, because it fails for the directionality of forces (bond angles).

1.2.2.2 Stillinger-Weber

This model potential-energy function comprising both two- and three-atom contributions has been proposed and fitted to describe interactions in solid and liquid forms of Si.

The two- and three body parts of this potential are [19]:

$$\mathrm{v}_2(r_{ij}) = \varepsilon f_2(r_{ij}/\sigma)$$

and

$$v_3(r_i,r_j,r_k) = \varepsilon f_3(r_i/,r_i/\sigma,r_j/\sigma,r_k/\sigma)$$

where ε is chosen to give f_2 depth -1, and σ is chosen to make $f_2(2^{1/6})$ vanish. That f_2 must be a function only of scalar distance is obvious; similarly, f_3 must possess full translational and rotational symmetry.

The reduced pair potential was selected from the following five parameter family:

$$f_2(r) = \begin{cases} A(Be^{-p} - r^{-q})e^{\frac{1}{r-a}} & r < a \\ 0 & r \geq a \end{cases}$$

where A, B, p, and a are positive; their fitted values are:

$$\begin{array}{lll} A = 7.049556277 & B = 0.6022245584 & \\ p = 4 & q = 0 & a = 1.8 \\ \lambda = 21.0 & \gamma = 1.20 & \end{array} \qquad (1.2)$$

This generic form automatically cuts off at r=a without discontinuities in any r derivatives, which is a distinct advantage in any molecular dynamics simulation application. This pair potential is shown in Fig. 1.3.

The same cutoff procedure is extended to the three-body interaction f_3

$$f_3(r_i,r_j,r_k) = h(r_{ij},r_{ik},\theta_{jik}) + h(r_{ji},r_{jk},\theta_{ijk}) + h(r_{ki},r_{kj},\theta_{ikj})$$

specified in an invariant fashion in terms of bond angles, e.g. θ_{jik} is the angle between r_j and r_k subtended at vertex i, etc. The function h belongs to a two parameter family (λ , $\gamma > 0$). Provided that both r_{ij} and r_{ik} are smaller than the previously introduced cutoff a, it has the following form:

$$h(r_{ij}, r_{ik}, \theta_{jik}) = \lambda e^{\gamma/(r_{ij}-a)+\gamma/(r_{ik}-a)}(\cos\theta_{jik} + \frac{1}{3})^2 \tag{1.3}$$

otherwise h vanishes identically. The "ideal" tetrahedral bonding angle θ_t is such that

$$\cos\theta_t = -\frac{1}{3}$$

so that the trigonometric part of Eq.(1.3) clearly discriminates in favor of pairs of bonds emanating from vertex i with the bulk geometry in the common diamond like structure of silicon.

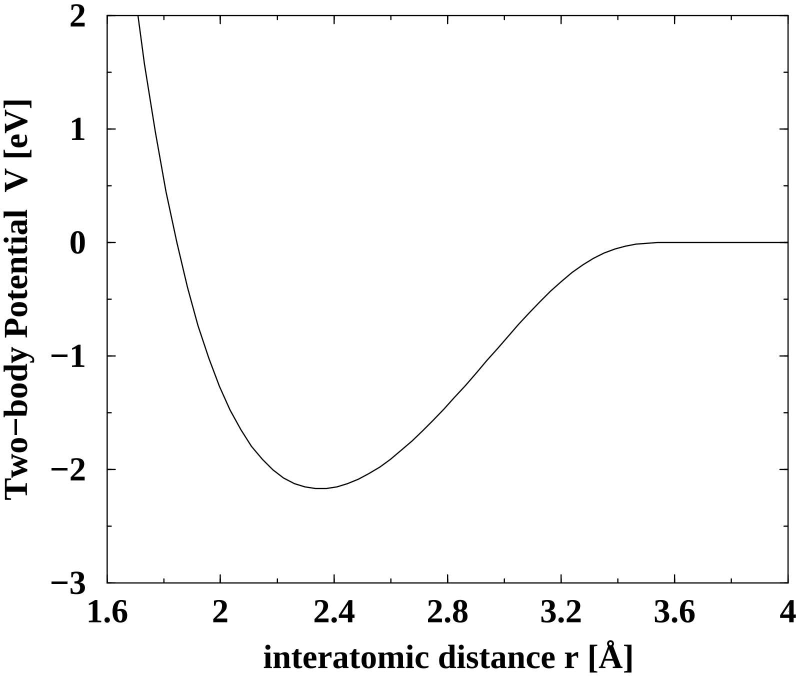

Figure 1.3: Pair part of the Stillinger-Weber potential

1.2.2.3 Biswas-Hamann

Biswas-Hamann potential [20] is a multiparameter potential fitted to the cohesive energies of a set of bulk phases, the formation energies of self-interstitials, and the surface energies of diamond Si(111)-1x1 and of metallic simple hexagonal and cubic (100) surfaces obtained from an *ab-initio* linearized augmented plane-wave(LAPW) calculation. The cut-off radius of this potential is larger than that of the Stillinger-Weber potential. Its three-body term is computationally very time-consuming to evaluate. For this reason we have used only the two-body part. The two-body part of this potential is a generalized Morse potential with 4 fitting parameters

$$V_2(r) = A_1 e^{-\lambda_1 r} + A_2 e^{-\lambda_2 r} \tag{1.4}$$

here $\lambda_1 = 3.946668$ Å^{-1} , $\lambda_2 = 1.191187$ Å^{-1}, $A_1 = 26829.3$ eV and $A_2 = -42.59863$ eV. The shape of the potential is shown in Fig. 1.4.

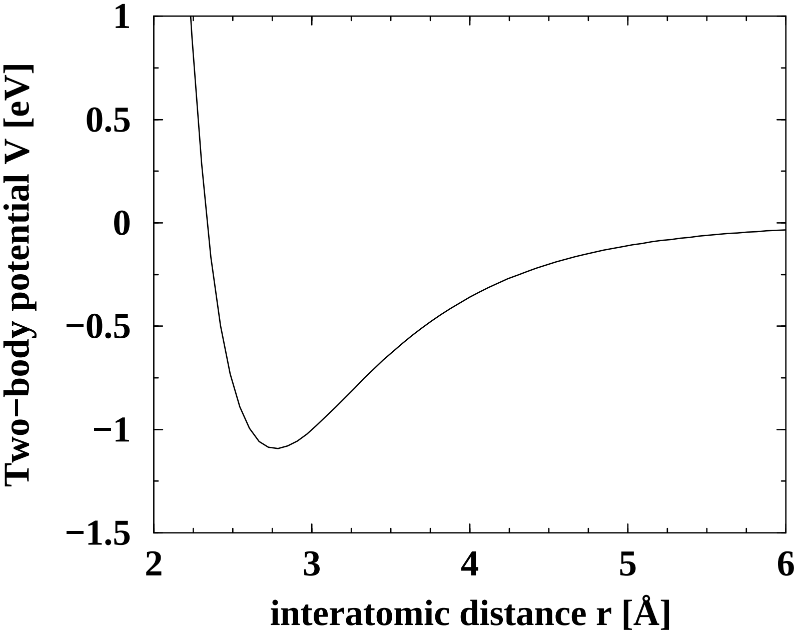

Figure 1.4: Pair part of the Biswas-Hamann interaction potential

1.2.2.4 Perez *et al*

Perez *et al*'s potential [13] is a total interaction potential between two subsystems (tip and sample) fitted to a Morse potential typically used to describe a diatomic molecule

$$V(z) = V_0 \left\{ \left[1 - exp(-2b\frac{z - R_c}{R_c}) \right]^2 - 1 \right\}$$

It was deduced from force versus distance characteristics above specific sites which were obtained in a sophisticated density functional (DFT) calculation of a Si(111)-5×5 surface interacting with model Si tip. V_0, b, R_c are parameters that define the strength, range, and minimum of the net interaction, while z is the distance between the nearest atoms of the sample and tip. Parameters fitted above two specific sites are given in Table 1.1.

1.2.2.5 Long-range interactions

Long-range interactions between tip and sample include van der Waals forces [21, 22], capillary forces due to the presence of fluid films at the surface when imaging

	V_0 [eV]	b	R_c [Å]
Adatom	2.273	1.497	2.357
Rest atom	2.636	1.526	2.357

Table 1.1: Parameters of Morse potential fitted by Perez *et al.*

in liquid or air, and electrostatic forces, including those due to tip and surface polarization, to patch charges and surface charging on freshly cleaved insulators.

The van der Waals(VdW) interaction is the most universal one. In the case of doped silicon tip and sample in UHV with zero applied voltage, it is the strongest long-range interaction. To calculate the van der Waals interaction between the tip and the surface, a knowledge of the tip macroscopic shape is required. We consider the VdW interaction as non-retarded and additive and compute it by using the Hamaker summation method[23]. We approximate the total tip-sample VdW interaction by integrating over the volumes of the tip and sample the asymptotic VdW pair potential between tip and surface atoms

$$V_{VdW} = -\frac{C}{r^6}$$

where the value of C depends on the tip and sample materials. The total VdW interaction depends on the geometry of the tip. For example, the interaction between a sphere and a plane is

$$F_{VdW} = -\frac{AR}{6(z-R)^2}$$

where $A = \pi^2\rho^2 C$ is the Hamaker constant for identical materials of density ρ, z is the distance from plane to center of the sphere and R is the sphere radius. The interaction between a cone and a plane is

$$F_{VdW} = -A\frac{\tan^2\theta}{6}\frac{1}{z}$$

where θ is the half angle of the cone and z is the distance from the plane to the apex of the cone.

The above approximations are only valid if the tip-sample separation z is large compared to the interatomic spacing, but are nevertheless used at short separations because the main contribution to the total interaction comes from more distant atom pairs.

1.3 Tight-Binding Linear Scaling Method

The past years have witnessed impressive advances in electronic structure calculation, especially in the complexity and size of the systems studied, as well as in computation time. Linear scaling methods based on empirical tight-binding Hamiltonians which can describe chemical bonding, and have a computational time proportional to the number of atoms N in the system, are of particular interest for simulations in material science. By contrast conventional diagonalization schemes scale as N^3. In combination with judiciously fitted parameters and an implementation suited for MD, it is possible to apply such *O(N)* methods to structural, electronic and dynamical properties of large systems which include up to 1000 atoms on a workstation.

1.3.1 Introduction: *Ab Initio* vs. Semiempirical, $O(N^3)$ vs. $O(N)$ Methods

In the past two decades, the percentage of theoretical investigations of materials based on atomistic computer simulations has steadily increased. Those using either an *ab-initio* or a tight-binding independent electron description of interactions are able to account for chemical bond formation and breaking, and are particularly worthy of attention, as reflected in the 1998 Nobel prize for chemistry[24]. One shortcoming of the usual implementation of such methods is that the number of operations scales as the third power of the number of atoms N, i.e., their computational cost is $O(N^3)$. Currently this limits the number of atoms in the system that can be treated even using very powerful computers. *Ab-initio* methods [25] certainly give more precise results than semiempirical tight-binding methods, but besides being based on more complicated Hamiltonians, they require much more extensive basis sets to expand the wave functions of electrons. Empirical tight-binding methods provide a useful compromise between classical empirical potential approaches and *ab-initio* methods, because they retain a quantum mechanical description of the electrons, ultimately responsible for chemical bonding, but the Hamiltonian is parametrized and the wavefunctions expanded in a minimal set of atomic orbitals. As a consequence, the number of atoms which can be handled with even the simplest *ab-initio* method, the Local Density Approximation(LDA)[26] commonly used in materials science is one to two orders of magnitude less than with tight-binding methods within the same computational constraints. Whereas chemists are interested in studying large, complex molecules, materials scientists are concerned with the properties of clusters, solids with specific defects or disorder, surfaces, interfaces, artificial structures and their interactions.

In order to increase the number of atoms in the system and to study dynamical process or finite-temperature properties obtained from time averages, efforts are constantly made to reduce computational cost. For this reason, many kinds of linear scaling methods have been introduced, tested and compared . The interested reader is referred to recent reviews[27, 28]. Linear scaling or *O(N)* means that the computation time is proportional to the number N of atoms in the system, just like in classical simulations with finite-range interaction potentials[16]. In the work described in this section we relied on a particular orbital-based linear scaling method which, in conjunction with a tight-binding Hamiltonian, has been successfully applied to C and Si systems[29, 30].

1.3.2 Semiempirical Tight-Binding Approximation

The empirical tight-binding (TB) approximation allows the quantum mechanical nature of covalent bonding to enter the interaction Hamiltonian in a natural way rather than through additional *ad hoc* angular terms in a classical potential.

In TB models the total energy of the system is expressed as

$$E = E_{BS} + \sum_{LL'} \phi\left(|\mathbf{R}_L - \mathbf{R}_{L'}|\right) \tag{1.5}$$

where ϕ is a repulsive two-body potential which includes the ion-ion repulsion and the electron-electron interactions which are double counted in the electronic band-structure term E_{BS}. This term describes chemical bonding; it can be written as

$$E_{BS} = \sum_i f_i \epsilon_i = \sum_i f_i < \psi_i \left| \hat{H}_{TB} \right| \psi_i > \tag{1.6}$$

where $\hat{H}_{TB}$ is the TB Hamiltonian, ϵ_i and $\{\psi_i\}$ are its eigenvalues and eigenstates, and f_i is their occupancy. The total number of valence electrons is from now on denoted as N and the total number of single particle states is then $N/2$ if we assume double occupancy, i.e., spin degeneracy for each state($f_i = 2$). The occupied eigenstates can in principle be determined by diagonalization, but in our work diagonalization is only used at the very end of each computation to check its accuracy and to determine the highest occupied and lowest unoccupied eigenstates if needed, as well as the energy gap which is given by the difference of the corresponding eigenstates. The off-diagonal elements of $\hat{H}_{TB}$ are described by invariant two-center matrix elements, $V_{ss\sigma}$, $V_{sp\sigma}$, $V_{pp\sigma}$ and $V_{pp\pi}$, between the set of sp^3 atomic orbitals(assumed orthonormal) (see Appendix A). By adjusting their values at the interatomic distance $r_0 = 2.35$Å in the equilibrium diamond like structures, as well as the diagonal elements E_s, E_p, a good fit to the position and dispersion of the occupied valence bands of Si can be obtained[31].

In order to study properties of covalently bonded systems with defects or free surfaces, tight-binding model must be transferable to different, physically relevant environments. An important advance was due to Goodwin, Skinner and Pettifor[32] who showed that it is possible to set up a TB model which accurately describes the energy-versus-volume behaviour of Si in crystalline phases with different atomic coordination, and reproduces the structure of small Si clusters.

We therefore adopt the functional form suggested by GSP[32] for the distance dependence of the two-center matrix elements:

$$V_\alpha(r) = V_\alpha(r_0) \left(\frac{r_0}{r}\right)^n exp\left\{ n\left[-\left(\frac{r}{r_c}\right)^{n_c} + \left(\frac{r_0}{r_c}\right)^{n_c} \right] \right\} \tag{1.7}$$

$$(\alpha\ :\ ss\sigma,\ sp\sigma,\ pp\sigma,\ pp\pi)$$

and of the two-body potential

$$\phi(r) = \phi_0 \left(\frac{r_0}{r}\right)^m exp\left\{ m\left[-\left(\frac{r}{d_c}\right)^{m_c} + \left(\frac{r_0}{d_c}\right)^{m_c} \right] \right\} \tag{1.8}$$

where r denotes the interatomic separation, and $n << n_c$, $m << m_c$, $r_c \approx d_c > r_0$ and ϕ_0 are parameters which are determined by fitting judiciously chosen properties. The resulting high values of n_c, m_c ensure a rapid decay of $V_\alpha(r)$, $\phi(r)$ beyond r_c, d_c. In MD simulations where a finite range of r is explored, the quantities in Eqs.(1.7-1.8) are further multiplied by a smoothed step function which switches from 1 to 0 in a narrow interval about a cutoff radius $r_m > r_c, d_c$, as described in section 1.1.2.

As explained below, similar couplings between Si and H atoms are required in some of our computations. Because hydrogen has a single occupied s-state, only $ss\sigma$ and $sp\sigma$ matrix elements must be parametrized; $H - H$ couplings are negligible at the separations considered here.

1.3.3 Tight-Binding Parametrizations

Within the above framework, improved sets of parameters were subsequently developed for Si-Si and Si-H interactions. In our work, we used the two different sets of parameters described in detail by Kwon *et al*[33] and Bowler *et al*[34].

The Si-Si parametrization of Kwon *et al*[33] is rather complicated, thus r_c's n_c's depend on α and the repulsive contribution is represented by a function of the second term in Eq.(1.5). The parameters are fitted to many properties of *Si* in the diamond structure and to computed(LDA) cohesive energies vs. density of four different structures. The resulting properties of liquid Si and of small Si clusters are in remarkable agreement with experiments and with *ab-initio* computations. On the other hand, this parametrization uses a cut-off which is beyond second nearest neighbours; this implies significantly larger computing times. The revised GSP parametrization of Bowler *et al* [34] is less complicated than the previous one; *Si-Si* parameters were fitted to fewer properties in the diamond and β-tin structures and *Si-H* parameters to properties of SiH_4. Furthermore, the cut-off radius r_c can be chosen between nearest and next-nearest-neighbours; thus this parametrization is well suited for linear scaling computations. It has in fact been successfully applied to defects and hydrogen diffusion on Si(001)[34].

1.3.4 One-electron eigenstates vs. localized and atomic orbitals

Traditional electronic structure methods solve the Schrödinger equation by expanding one-electron wavefunctions in a fixed basis set (plane waves, atomic orbitals or combinations thereof) and by diagonalizing the resulting secular equation for the expansion coefficients. In spite of significant progress achieved by applying efficient diagonalization algorithms, the required computing time is proportional to NP^2, P being the number of basis functions. Because $P \propto N$, the computational cost is $O(N^3)$, the scaling factor depending on the method, being small in the case of empirical tight-binding. Nevertheless, the diagonalization of $\hat{H}$ for each atomic geometry or at each step of an MD simulation limits the number of atoms that can be currently studied in conventional TBMD computations to about 100 using a workstation and around 1000 using a supercomputer.

The recently developed linear scaling methods compute the total energy by minimizing a functional expressed in terms of localized orbitals in real space. Although typical eigenstates in a condensed system extend throughout most of it, a unitary transformation yields linear combinations of the former which are localized about particular sites. On the basis of exact model calculations[35], these so-called Wannier orbitals are believed to decay exponentially in systems with a finite energy gap between occupied and empty states [36]. This applies in particular to the finite systems on which computations are carried out, although the effective gap will be small and the resulting decay slow if the corresponding real system is metallic.

The key feature of $O(N)$ methods is that the total energy and the forces acting on individual atoms are evaluated *without computing the eigenvalues and eigenstates of* $\hat{H}$. This is accomplished by dividing the full system into finite subsystems and by defining approximate *localized orbitals* ϕ (LO) which are forced to vanish outside each subsystem[37]. These *localized regions* (LR) are the electronic equivalents of the *linked cells* which ensure *O(N)* scaling in classical simulation as explained in section 1.2.1[16]. Intuition and experience suggest that the minimum size of each localization region depends on physical and chemical properties of the constituents, and not on the size of the whole system. The size of the localized regions (which must exceed the range of $\hat{H}$) is the factor which limits the speed and accuracy of an $O(N)$-TB calculation.

1.3.5 Orbital-Based Linear Scaling Energy Minimization without Orthogonalization Constraints

The key ingredient of $O(N)$ scaling methods is the definition of an appropriate energy functional whose minimization requires neither explicit orthogonalization of the auxiliary localized orbitals, nor the inversion of their overlap matrix $\mathbf{S}$. This functional is different from that defined in Eq.(1.5), but must have the same global minimum in the limit of infinite localization regions. Otherwise it yields an upperbound which in practice must be close to the minimum energy even for relatively small LR's. This can in fact be achieved[27, 28, 30]. Various *O(N)* methods are based on different functionals which, however, share this remarkable property.

One convenient energy functional which satisfies these requirements can be obtained by using the Lödwin transformation[38] $\psi_i = \sum_j S_{ij}^{-1/2} \phi_j$[30]:

$$E_{GBS}\left[\{\phi\}, \mu, M\right] = 2 \sum_{ij=1}^{M} (2\delta_{ij} - S_{ij}) < \phi_j \left| \hat{H} - \mu \right| \phi_i > +\mu N \tag{1.9}$$

The matrix $(2I - S)$ is the first order truncated series expansion of the inverse overlap matrix S^{-1}, where $S_{ij} =< \phi_i | \phi_j >$. The generalized band structure energy functional defined in Eq.(1.9) depends on the number M of localized orbitals, and on a global Lagrange multiplier μ which determines the highest filled state and hence the total electronic charge in the system at the minimum. Taking $M > N/2$ helps avoid unphysical solutions[30], which can otherwise be obtained depending on the initial choice of the orbitals.

In order to find the electronic ground state energy for a given spatial configuration of the atoms, the functional is minimized with respect to the LO's. Normally each LR is centered at an atomic site I and encompasses all neighbours connected by n bonds; it is then denoted by nLR. Each LO ϕ_i centered at atomic site I can be expressed as

$$\phi_i = \sum_{J \in \{LR_I\}}^{n_b} \sum_l C^i_{Jl} \alpha_{Jl} \tag{1.10}$$

where α_{Jl}'s are the atomic basis functions on atom J, the index l runs over orbital components (e.g. s, p_x, p_y, p_z for carbon or silicon and s for H), $\{LR_I\}$ indicates the set of atoms within the localization region centered at site I, and n_b is the corresponding number of basis functions.

The functional is efficiently minimized using a conjugate gradient (CG) algorithm[39], the required derivatives

$$\frac{\partial E_{GBS}}{\partial \phi_i} = 4 \sum_j^M \left[|(H-\mu)\phi_i > (2\delta_{ij} - S_{ij}) - |\phi_j >< \phi_j \,|(H-\mu)|\, \phi_i > \right] \tag{1.11}$$

being evaluated at each iteration step. Using Eq.(1.10) the matrix elements can be expressed in terms of the Slater-Koster energy integrals $< \alpha_{Jl} | \hat{H}_{TB} | \alpha_{J'l'} >$[40] and those energy integrals can be further expressed in terms of direction cosines and of the the invariant two-center matrix elements defined by Eq.(1.7)(see Appendix B). Because each derivative needs to be evaluated only in the localization region $\{LR\}_I$, the required number of operations scales linearly with the number of atoms in the system. The global variable μ is initially chosen well above the estimated Fermi energy of the system, then iteratively adjusted until the total charge of the system becomes equal to the charge consistent with global neutrality when convergence is achieved, i.e. when the ground state energy corresponding to the assumed LRs is attained, and μ is then the chemical potential (Fermi energy) of the electrons[30].

1.3.6 Total Energy Minimization with Respect to Atomic and Electronic Readjustment, electrochemical potential

In this work we consider metastable structures of silicon surfaces and model tips. To determine such structures, atoms in several surface layers are allowed to move under the influence of the forces

$$F_I = -\partial E / \partial R_I \tag{1.12}$$

until all their components become smaller than a preset tolerance (0.01 $eV/\AA$) and the energy E reaches a minimum. Instead of using a standard minimization procedure, this is achieved by using MD and introducing a damping term in the standard Verlet algorithm [16] as described in section 1.4.2.

Eq.(1.12) is physically meaningful only if the electrons are in their ground state (Born-Oppenheimer approximation [41]). Therefore, molecular dynamics can be started only after electronic convergence with respect to the initial atomic configuration has been achieved. This rather tedious procedure is necessary at the start of a calculation. The required computing time depends on the initial choice of the LOs and μ. To be safe, we start with random coefficients in Eq.(1.10) and a high μ. To ensure stable MD integration, the time step must be small compared to a typical optical vibration period. The corresponding atomic displacements are then small and typically do not strongly perturb the LO coefficients, except if same atom(s) move out of or into certain LRs. Therefore, after each atom move, enough electronic iterations must be performed in order to reach the slightly modified ground state (within a tolerance of $10^{-4}\ eV$). Fortunately, only small adjustments of μ are necessary once global charge neutrality has been established; they can be performed automatically. The number of electronic steps depends on the system, the narrower its energy gap at the Fermi level(always existing in a finite system), the more electronic steps are needed. Useful *O(N)* performance is achieved if this number of electronic iterations is independent of N and if the necessary computing time is less than that required for diagonalization.

1.3.7 Local vs. global charge neutrality

If significant rearrangements occur in the course of a molecular dynamics simulation, it is sometimes difficult to avoid unphysical charge transfer between neighboring atoms or layers. To reduce such effects, which slow down convergence and sometimes lead to unphysical solutions, local charge neutrality is approximately imposed by adding an extra term $H_U = \frac{1}{2}U\sum_I(q_I - q_I^0)^2$, where $q_I^0 = 4.0$ for Si and 1.0 for H atoms, and the charge around site I is expressed as

$$q_I = 2\sum_{ij}(2\delta_{ij} - S_{ij}) < \phi_i\,|\mathbf{R}_I >< \mathbf{R}_I|\,\phi_j > \qquad (1.13)$$

where $< \phi_i|\mathbf{R}_I >$ indicates the projection of the localized orbital ϕ_i on the localized region around site I[30]. Such a term is obtained by making a local mean field approximation to the Hubbard Hamiltonian, assuming no spin-polarized solutions[42]. The strength U has been estimated and tabulated by Harrison[43] who also discussed its reduction by dielectric polarization. In our simulations we have used U=8.0eV. In covalent systems contributions to H_U must essentially vanish for atoms which have a bulk-like environment once convergence is achieved.

1.4 Integration Algorithms

1.4.1 Equations of motion

Consider a system which includes N atoms. The microscopic state of the system may be specified in terms of the positions and momenta of the atoms. Within the Born-Oppenheimer approximation, it is possible to express the Hamiltonian of the system as a function of the nuclear variables, the rapid motions of the electrons being included in an empirical potential or in the total energy as described in the preceding section. If we make the further approximation that the atoms considered behave classically, then the Hamiltonian of the system can be expressed as a sum of kinetic energy and potential energy functions of a set of generalized coordinates q_i and momenta p_i. Adopting a condensed notation

$$q = (q_1, q_2, \cdots, q_N),$$

$$p = (p_1, p_2, \cdots p_N),$$

we write

$$H(q,p) = K(p) + V(q).$$

If the coordinates q are simply the set of the Cartesian coordinates $\mathbf{r}_i$, of each atom in the system, p stands for the *linear momenta* $\mathbf{p}_i = m_i \mathbf{v}_i$, and the kinetic energy K takes the form

$$K = \sum_{i=1}^{N} (p_{ix}^2 + p_{iy}^2 + p_{iz}^2)/2m_i \tag{1.14}$$

where m_i is the mass of atom i, and p_{ix}, p_{iy}, p_{iz}'s are the x, y, z components of the momentum of atom i. The potential energy V contains all information concerning interatomic interactions. We already discussed tight-binding and empirical approaches to the calculation of V.

Molecular dynamics (MD) simulations rely on a numerical solution of Newton's equations

$$\frac{d^2\mathbf{r}_i}{dt^2} = \mathbf{F}_i/m_i \equiv \mathbf{a}_i \tag{1.15}$$

where

$$F_i = -\nabla_{r_i} V$$

is the force on atom i.

1.4.2 Finite difference schemes

The solution of such coupled differential equations is based on a judicious finite difference approximation. The general idea is to obtain the trajectories of individual atoms, e.g, coordinates, velocities, accelerations etc., at time step $t + \delta t$ from the coordinates and velocities at earlier time steps with a tolerable error. Different algorithms can be used. The optimal choice represents a compromise between the following requirements.

- The algorithm should be fast, accurate, and require little memory
- It should be stable for a time step δt not too small compared to the shortest characteristic relaxation time or oscillation period of the system under consideration
- It should be simple in form and easy to program
- It should preserve energy conservation

In the following subsections we will describe most popular algorithms used in MD simulations. A detailed discussion can be found in [16].

1.4.2.1 Verlet algorithm

Verlet algorithm [44] is based on a direct solution of the second-order Eq. (1.15). The equation for advancing the positions of each atom is

$$\mathbf{r}(t+\delta t) = 2\mathbf{r}(t) - \mathbf{r}(t-\delta t) + \frac{\mathbf{F}_i(t)}{m_i}(\delta t)^2 \tag{1.16}$$

the error being of order δt^4. Note that the velocity does not enter in the above formula. A minor drawback is that it requires the values of $\mathbf{r}(t-\delta t)$ and is thus not self starting. The velocities required to computing kinetic energy K and Hamiltonian H can then be calculated as

$$\mathbf{v}(t) = \frac{\mathbf{r}(t+\delta t) - \mathbf{r}(t-\delta t)}{2\delta t} \tag{1.17}$$

the error being of order δt^2.

There are several variants of Verlet's algorithm.

i. The *leap-frog* algorithm uses the following steps

$$\mathbf{v}(t+\frac{1}{2}\delta t) = \mathbf{v}(t-\frac{1}{2}\delta t) + \delta t\mathbf{a}(t)$$

$$\mathbf{r}(t+\delta t) = \mathbf{r}(t) + \delta t\mathbf{v}(t+\frac{1}{2}\delta t)$$

Thus the velocities $\mathbf{v}(t+\frac{1}{2}\delta t)$ are first calculated from the velocities at time $t-\frac{1}{2}\delta t$ and accelerations $\mathbf{a}(t)$. The positions $\mathbf{r}(t+\delta t)$ are then calculated from the just calculated velocities and positions at time t. The velocities at time t can be calculated from

$$\mathbf{v}(t) = \frac{1}{2}[\mathbf{v}(t+\frac{1}{2}\delta t) + \mathbf{v}(t-\frac{1}{2}\delta t)]$$

ii. The *velocity Verlet algorithm* gives the positions and velocities at the same time:

$$\mathbf{r}(t+\delta t) = \mathbf{r}(t) + \delta t\mathbf{v}(t) + \frac{1}{2}\delta t^2\mathbf{a}(t)$$

$$\mathbf{v}(t+\delta t) = \mathbf{v}(t) + \frac{1}{2}\delta t[\mathbf{a}(t) + \mathbf{a}(t+\delta t)]$$

1.4.2.2 Gear predictor-corrector algorithm

If the trajectories are continuous, then an estimate of the positions, velocities etc. at time $t+\delta t$ may be obtained from a Taylor expansion about time t:

$$\begin{aligned}
\mathbf{r}^p(t+\delta t) &= \mathbf{r}(t) + \delta t\mathbf{v}(t) + \tfrac{1}{2}\delta t^2\mathbf{a}(t) + \tfrac{1}{6}\delta t^3\mathbf{b}(t) + \cdots \\
\mathbf{v}^p(t+\delta t) &= \mathbf{v}(t) + \delta t\mathbf{a}(t) + \tfrac{1}{2}\delta t^2\mathbf{b}(t) + \cdots \\
\mathbf{a}^p(t+\delta t) &= \mathbf{a}(t) + \delta t\mathbf{b}(t) + \cdots \\
\mathbf{b}^p(t+\delta t) &= \mathbf{b}(t) + \cdots \\
\cdots
\end{aligned}$$

where $\mathbf{r}, \mathbf{v}, \mathbf{a}, \mathbf{b}$ are the position, velocity, acceleration and third time derivative of the position, respectively. The superscript marks these as "predicted" values.

We may calculate the force at time step at $t + \delta t$ and the correct acceleration $\mathbf{a}^c(t + \delta t)$. Then the error in the predicted step calculated as

$$\Delta\mathbf{a}(t + \delta t) = \mathbf{a}^c(t + \delta t) - \mathbf{a}^p(t + \delta t)$$

From these we can further correct the trajectory as

$$\begin{aligned}
\mathbf{r}^c(t + \delta t) &= \mathbf{r}^p(t + \delta t) + c_0\Delta\mathbf{a}^c(t + \delta t) \\
\mathbf{v}^c(t + \delta t) &= \mathbf{v}^p(t + \delta t) + c_1\Delta\mathbf{a}^c(t + \delta t) \\
\mathbf{a}^c(t + \delta t) &= \mathbf{a}^p(t + \delta t) + c_2\Delta\mathbf{a}^c(t + \delta t) \\
\mathbf{b}^c(t + \delta t) &= \mathbf{b}^p(t + \delta t) + c_3\Delta\mathbf{a}^c(t + \delta t) \\
&\cdots
\end{aligned}$$

Gear [45] has discussed the best choice for the coefficients $c_0, c_1, c_2, c_3, c_4, \cdots$. In some of the calculations in chapter 3 we have used the 5^{th} order predictor-corrector algorithm and the values chosen are 19/120, 3/4, 1, 1/2, 1/12, respectively.

The corrector step may be iterated to get more accurate trajectories, but this being a time-consuming procedure, normally just one corrector step is carried out at each time step. Thus δt cannot be chosen too large, but can in principle be chosen larger than for the Verlet algorithm because Gear's method is more accurate.

1.5 Temperature Control

An important point is that we want to study the system at a predefined temperature rather than at a predefined total energy because the temperature is easily measurable and controllable in the experiments. This can be done either by modifying the equations of motion or by including coupling to a heat bath by extending the Hamiltonian. We briefly discuss the principles and procedures employed in the following subsections.

1.5.1 Equipartition theorem

In the microcanonical ensemble, the total energy is constant but the kinetic energy fluctuates. For a system of classical particles in thermal equilibration, the temperature is directly related to the average kinetic energy of the system as follows:

$$K = \sum_{i=1}^{N} \frac{p_i^2}{2m_i} = \frac{g}{2} k_B T \tag{1.18}$$

where k_B is Boltzman's constant and T the is temperature. The number of degrees of freedom $g = 3N - N_c$, where N_c is number of constraints in the system. In the canonical ensemble the system temperature is constant but the instantaneous total kinetic energy still fluctuates. In a MD simulation, K can be computed at each time step and Eq. (1.18) is used to compare T to the preset temperature T_0.

1.5.2 Equilibration

Temperature control in constant temperature molecular dynamics is established in three stages: start, equilibration, and constant-temperature runs. At the start of a run, velocities are assigned randomly according to the set temperature, then simple velocity rescaling is used to enforce equilibration; 200-2000 steps are typically sufficient for the systems containing about 1000 atoms treated here enough. Constant temperature runs are performed using a Berendsen thermostat after these initialization steps.

1.5.3 Simple velocity rescaling

In this method all velocities are rescaled at each time step according to the set temperature T_0 by a factor λ. The equipartition theorem is used to define the kinetic temperature at the current step

$$T = \frac{1}{gk_B}\sum_i \frac{m_i v_i^2}{2}$$

The required temperature change is then calculated as follows

$$T_0 - T = \frac{1}{gk_B}\sum_i \frac{m_i(\lambda v_i)^2}{2} - \frac{1}{gk_B}\sum_i \frac{m_i v_i^2}{2} = (\lambda^2 - 1)T \tag{1.19}$$

The scaling factor is therefore

$$\lambda = \sqrt{T_0/T}$$

1.5.4 Berendsen thermostat (velocity rescaling with time delay)

In this method [46] velocities are still rescaled at each time step but much more gently so as to reach the set temperature T_0 with a time delay τ. The system is effectively weakly coupled to heat bath or thermostat at the desired temperature T_0. The bath acts as a source or sink of kinetic energy, supplying or removing heat from the system as appropriate. The velocities are scaled at each step, such that the rate of change of the temperature is proportional to the difference in temperature between the bath and the system

$$\frac{dT}{dt} = \frac{1}{\tau}(T_0 - T)$$

In the language of control theory this corresponds to first-order feddback; τ is a relaxation time whose magnitude determines how tightly the bath and the system are coupled together. If fluctuations are neglected, and equipartition has been established, this method gives an exponential decay towards the desired temperature. The change in temperature between successive time steps is approximately

$$\Delta T = \frac{\delta t}{\tau}(T_0 - T)$$

Comparing this equation with Eq. (1.19) one obtains the modified scaling factor for the velocities

$$\lambda = \sqrt{1 + \frac{\delta t}{\tau_T}(\frac{T_0}{T} - 1)}$$

If τ is large the coupling is weak. If τ is equal to the time step δt then this algorithm is equivalent to simple velocity rescaling. In our simulations the time τ was chosen between 100-400δt. For MD simulations of a driven subsystem, e.g. a sample interacting with a moving tip the Berendsen thermostat is more convenient than that described next, because no strong T-oscillations arise unless an induced configurational change converts potential energy into kinetic energy of a few atoms.

1.5.5 Nose thermostat

In this method [47, 48] the dynamics of the system coupled to a heatbath or thermostat is described by one extra degree of freedom. Energy is allowed to flow continuously from the thermostat to the system and back, so that accuracy is not undermined, by discontinuous changes in velocity.

The equations of motion of the "extended system" can be written as[49]

$$\frac{d\mathbf{q}_i}{dt} = \frac{\mathbf{p}_i}{m_i}$$

$$\frac{d\mathbf{p}_i}{dt} = \mathbf{F}_i - \xi\mathbf{p}_i$$

$$\frac{d\xi}{dt} = 2(\sum_i \frac{p_i^2}{2m_i} - \frac{g}{2}k_BT)/Q$$

$$\frac{1}{s}\frac{ds}{dt} = \xi$$

and correspond to second order feedback control of T.

The Hamiltonian of the extended system

$$H' = \sum_i \frac{p_i^2}{2m_i} + V(q) + \frac{Q}{2}\xi^2 + (g+1)k_BT\ln s,$$

is conserved. Moreover, if the system is ergodic, so that equipartition is indeed established after a certain time, long enough time averages become equal to their canonical ensemble averages. This is most useful for accurate computations of equilibrium properties, in particular their fluctuations and time-dependent correlations. Q is the inertia associated with the thermostat coordinate ξ, and plays a role similar to τ in the Berendsen thermostat. However, as in any second order feedback system, weak coupling can lead to unphysical T-oscillations.

From the above equation of motions, one obtains modified leap-frog variables at time step $t + \delta t$ as

$$\mathbf{r}_i(t+\delta t) = \mathbf{r}_i(t) + \delta t \mathbf{v}_i(t) + \frac{\delta t^2}{2}(\frac{\mathbf{F}_i(t)}{m_i} - \xi(t)\mathbf{v}_i(t))$$

$$\mathbf{v}_i(t+\delta t/2) = \mathbf{v}_i(t) + \frac{\delta t}{2}(\frac{\mathbf{F}_i(t)}{m_i} - \xi(t)\mathbf{v}_i(t))$$

$$\mathbf{r}_i(t+\delta t) = \mathbf{r}_i(t) + \delta t \mathbf{v}_i(t+\delta t/2)$$

$$\xi(t+\delta t/2) = \xi(t) + \frac{\delta t}{2Q}(\sum_i m_i \mathbf{v}_i^2(t) - g k_B T)$$

$$\xi(t+\delta t) = \xi(t+\delta t/2) + \frac{\delta t}{2Q}(\sum_i m_i \mathbf{v}_i^2(t+\delta t/2) - g k_B T)$$

$$\mathbf{v}_i(t+\delta t) = \frac{2}{2+\delta t \xi(t+\delta t)}(\mathbf{v}_i(t+\delta t/2) + \delta t \frac{\mathbf{F}_i(t+\delta t)}{2m_i})$$

1.5.6 Simulated Annealing

Annealing is a process used in glass making and metallurgy. It is the process of solidifying glass or an alloy from the molten state by cooling it slowly. Slow cooling results in a far more orderly arrangement of atoms and molecules than rapid cooling, with the result that the resulting solid is far stronger.

In minimization problems, a basic obstacle to the determination of the global minimum is the presence of local minima. Iterative methods for seeking a minimum, such as conjugate gradients usually get trapped in a neighborhood of a local minimum, because escaping from such a neighborhood would involve a temporary increase in the value of the function that is to be minimized.

The solution to this problem proposed by simulated annealing [39] is to suspend the minimization process occasionally, in the hope that this will allow the process to escape from a local minimum to an other nearby minimum, and possibly to the global minimum. The process is controlled by a parameter which is varied during the course of the process is such a way as to ensure that escape may occur frequently in the early stages of the process, and less and less frequently as the process continues. This parameter is the analogue of the temperature in physical annealing, where the temperature controls the mobility of atoms and molecules, making them less mobile as the substance cools.

Chapter 2

Tight-Binding Simulations of Silicon Surfaces and Tips

2.1 Introduction

In this chapter we present calculations done with the linear-scaling tight-binding method described in the previous chapter which has hitherto been mainly applied to carbon systems. Our ultimate goal was to simulate atomic force microscopy(AFM) and manipulation with a Si tip. We first tested the method by trying to reproduce known reconstructed structures of Si surfaces and a particular surface defect. Then we applied it to study the (meta)stability of pyramidal Si tips with a [001] axis like those microfabricated by etching (001) wafers [50] and used in AFM experiments. In the end we abandoned our initial goal because the required simulations would have been too time-consuming in spite of the linear-scaling implemented in the TB program at our disposal and our attempts to speed it up.

We first present and discuss our results on *Si(111)* and *Si(001)* surface reconstructions which exhibit characteristic features due to rebonding of surface atoms and have previously been studied by tight-binding and *ab-initio* methods. Such reconstructions reduce the density of energetically unfavorable dangling bonds on surface atoms, but induce distortions from the tetrahedral bonding pattern in the bulk. Optimum surface structures represent a delicate balance between different effects and can not usually be guessed by chemical and physical intuition.

These reconstructed surfaces are therefore well-suited for validating the method and are also interesting candidates for controlled atomic scale manipulation experiments. Surface properties are extracted from computations on slabs with a finite number of layers. This number must be large enough to suppress artificial coupling between the free slab surfaces which can arise owing to the overlap of electronic surface states and/or of strain fields induced by atomic rearrangements in surface layers. In order to approximate the effect of the crystalline substrate, atoms in the two central layers are held in their bulk positions. Alternatively, the bottom two layers are fixed, and all exposed dangling bonds are passivated with hydrogen atoms so as to preserve tetrahedral coordination.

Similar accuracy is then expected with half the number of free layers, compared to the former, symmetric slab. Having this in mind, we have investigated the influence of factors which, if chosen properly, should have little effect on physical meaningful results. This includes the number of free and fixed (bulk-like) layers in the slabs used, the influence of H-passivation at the bottom, the shape and lateral dimensions of the computational supercell, the size of the localization regions, the tight-binding parametrization. Even starting from configurations which had the periodicity and some of the rebonding characteristics of desired reconstructions, this required many computations which were performed on not too large systems in order to economize computing time. Thus the emphasis here is on validation rather than on achieving *O(N)* performance, although linear scaling was verified in the largest systems containing a few hundred atoms.

2.2 Si(111)-5x5 Reconstruction

The metastable 5×5 reconstruction plays an important role in the conversion from the 2×1 reconstruction obtained upon cleavage to the stable 7×7 reconstruction of the Si(111) surface [51]. It exhibits the characteristic features of the DAS model, first proposed for Si(111)-7x7[12, 11], which are indicated in Fig. 2.1.

One important difference is that the 5×5 reconstruction has the same average density of atoms in surface layers as the bulk terminated Si(111) surface, whereas additional Si adatoms must be supplied to form the 7×7 reconstruction. There is only one type of adatom in each half of the 5×5 surface unit cell while there are two types, i.e. central and corner adatom in each half of the 7×7 surface unit cell.

2.2.1 Computational Details

We start with a ten-layers thick inversion-symmetric slab which has two bulk truncated (111) surfaces at the top and bottom, encompassing two adjacent 5×5 surface unit cells. Periodic boundary conditions are maintained in the lateral directions. We have also repeated some of the computations with a six-layers slab passivated by H atoms at the bottom, similar to that used by Adams and Sankey[52]. Following these authors, the initial configuration on the free surface(s) is set up by laterally shifting ten atoms in the surface layer of the left half of each 5×5 cell so that they are placed above fourth layer atoms. Then five atoms at one edge of the other unfaulted triangular half and the second-layer atom above the corner hole are placed at the positions of the adatoms so that their bond lengths to the nearest first-layer atoms are equal to the bulk interatomic distance r_0. During the combined relaxation of electrons and ions dimers spontaneously formed along the boundaries between "faulted" and "unfaulted" halves shortly after we started the damped molecular dynamics calculation. At the end, we obtained the relaxed structure consistent with the DAS model illustrated in Fig.2.1. Of the 25 dangling bonds per 5×5 cell on the truncated (111) surface only 9 are left: one on the corner hole atom (CH), two on the restatom(R) and six on the adatoms(AD). The former three are

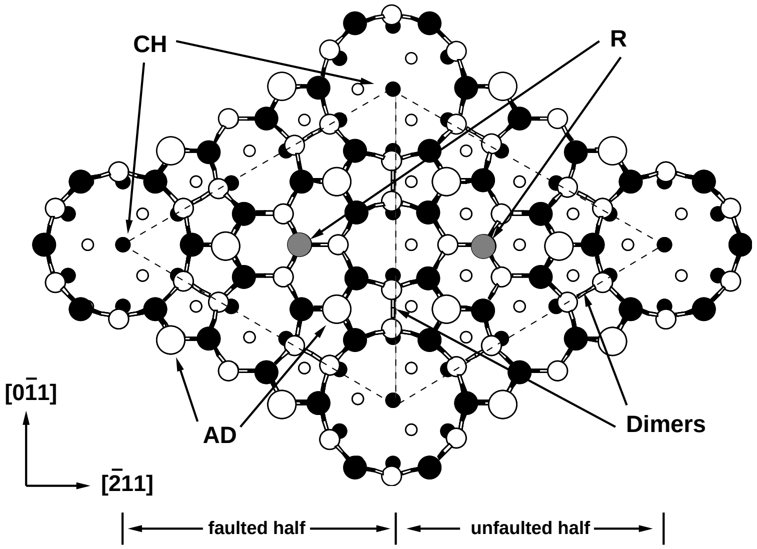

Figure 2.1: Top view of the Dimer-Adatom-Staking fault structure of the Si(111)-5 × 5 reconstruction. Circles of decreasing diameter denote atoms in successive layers starting from the top. Large white ones are adatoms; large black and grey ones belong to the first layer with a stacking fault in the left half; smaller white ones belong to the dimer layer; small black ones appear at the center of corner holes and adjacent to the dimers, whereas remaining third layer atoms are hidden under the adatoms; finally small white ones belong to the fourth layer. Adatoms(AD), rest atoms(R), corner holes(CH) atoms and the boundary of the surface unit cell are indicated. The thin dotted-dashed line along the short diagonal divides the faulted and unfaulted halves.

doubly occupied, whereas surface states derived from those on the adatoms are partially occupied by the remaining three electrons[52]. Thus one expects the $Si(111)-5{\times}5$ surface to have metallic properties just like $Si(111)-7{\times}7$. As a matter of fact, a posteriori diagonalization revealed a tiny energy gap ($< 0.01eV$) in our relaxed structure. One might also expect problems due to the assumed double occupancy. In fact relaxation in a slab encompassing a single $5{\times}5$ surface unit cell produced a distorted DAS structure with twisted dimers. On the other hand, no such distortions have been found in previous $O(N^3)$ computations of $Si(111)-7{\times}7$ with similar slabs which relied on occupied eigenstates at the Γ-point(zero wave-vector) obtained by diagonalization[53] or [54, 55, 56] by total energy minimization *with* orthonormality constraints[57, 25]. Deviations might arise owing to the small size of the localization region(n=3) in our O(N) computations. Fortunately this is not the case, as discussed in the following section, if slabs encompassing an even number number of dangling bonds on each surface are used.

2.2.2 Convergence, Accuracy and Determination of Surface Energies

Our relaxed configuration exhibits common structural features found in previous computations of the 5×5[52, 54] and of the 7×7[53, 55, 56] reconstructions. In what follows we compare results obtained with Bowler's parametrization[34], localization regions encompassing third neighbours and a 5×10 computational cell containing four free layers (not counting the adatoms) and two fixed *Si* layers with the bottom one saturated by H atoms. In order to check the influence of free and fixed(bulk-like) layers in the slab, of passivation by H at the bottom, of the size of the localization regions, and of the tight-binding parametrization, we have performed many calculations of the relaxed geometry of the 5×5 reconstruction. From the results summarized in Appendix C one can conclude that the influence of these factors on the final configuration is negligibly small. This is a very encouraging result. Furthermore the bond lengths listed in Table 2.1 are remarkably close (except for dimers) to those found in recent TB calculations for the 7×7 reconstruction based on a symmetric slab with one free layer less on each side[56]. Small deviations occur, however, compared to bond lengths extracted from a LDA computation for the same system[55]. Similar deviations also occur in an earlier TB computation for a H-passivated slab with two less free layers[53]. In that case, these deviations might be due to that restriction or to the somewhat different parametrization. More significant deviations appear when height differences between adatoms and rest atoms in the two halves of the surface unit cells are compared(see Table 2.2). Our computed differences are larger than those found in previous computations for the 7×7 reconstruction with a smaller number of free layers. On the other hand, our height difference between adatoms is only half of that found in a pioneering computation for $Si(111) - 5{\times}5$ based on a H-passivated slab like ours[52]. Moreover, in contrast to that work, we found that adatoms in each half are almost equivalent, just like corner hole and central adatoms on the $Si(111)\,-\,7{\times}7$ surface. These two discrepancies are probably due to the *non self-consistent* LDA-based approximation used in Ref.[52]. TB computations, including ours, are only rudimentary self-consistent if the Hubbard term is included, but since the parameters are fitted to experimental data[34] and/or self-consistent LDA computations[33], they can yield better results.

The accuracy, efficiency and performance of our O(N) TB computations can be judged on the basis of the results reported in Table 2.3 for the system described in the preceding section. The computations were performed on a single processor of a DEC-Alpha 8400 machine; nLR refers to unconstrained minimizations with localization regions encompassing neighbours connected by n bonds. Diagonalization of the electronic TB Hamiltonian was performed at the end of the 3LR minimization. The first three rows refer to the unbiased but costly minimizations starting with orthonormalized LOs with random coefficients. The subsequent combined optimization of LO coefficients and atomic positions takes about the same time. More importantly, the ratio of conjugate gradient(CG) to MD steps implies that only three CG steps per MD step are on the average required to reconverge the coefficients.

Bonds	present	Kim *et al*[56]	Qian *et al*[53]	Brommer *et al*[55]
1	2.550	2.58	2.486	2.49
2	2.575	2.57	2.471	2.474
3	2.435	2.43	2.410	2.376
4	2.417	2.45	2.463	2.456
5	2.39	2.39	2.405	2.396
6	2.408	N/A	N/A	2.40

Table 2.1: Computed average bond lengths(in Å) between Si atoms in different surface layers of the Si(111)-5×5 (this work) and 7×7 reconstructions; 1 - Adatom-first layer atom; 2 - Adatom-second layer atom; 3 - Rest atom-second layer atom; 4 - Dimer; 5 - Dimer atom-third layer atom; 6 - Corner hole atom-fourth layer atom

Atoms	Present	Adams *et al*[52]	Qian *et al*[53]	Brommer *et al*[55]
adatoms	0.08	0.17	0.055, 0.07	0.047,0.030
rest atoms	-0.05	-	-0.01	0.03

Table 2.2: Computed height differences(in Å) between adatoms(AD) and rest atoms(R) in the faulted and unfaulted halves of the 5×5 and of the 7×7 Si(111) surface unit cells. For the 7×7 reconstruction, the two values given refer to the adatoms near corner holes and near the centers of each half unit cell.

Relaxation	Quantity	2 LR	3 LR	Diag.
Initial (Electrons)	Tot. En.(eV)	-12896.83	-12918.38	-12932.55
	Comp. time(hrs.)	4.5	23	N/A
	CG steps	3400	5500	N/A
Electrons and Atoms	Tot. En.(eV)	-12958.05	-12.977.68	-12987.32
	Comp. time(hrs.)	6.5	22	N/A
	MD steps	1848	1778	N/A

Table 2.3: Comparison of total energies of the relaxed Si(111)-5×5 system at different levels of approximation, required computation times and numbers of iterations for 300 Si and 50 H atoms.

A comparison of the last two columns suggests that 3LR minimization yields total energies with a relative accuracy of about 10^{-4}. The specified tolerance on the relative energy difference between successive CG iterations(our convergence criterion) was, of course, much smaller. Note that diagonalization yields eigenstates corresponding to the Γ-point of the computational supercell. More accurate total energies could be obtained by including occupied eigenstates with nonzero parallel wave-vectors in Eq.(1.6) or by increasing the lateral dimensions of the supercell(the only alternative in the case of O(N) computations). The surface energy differences ΔE_s which determine the relative stability of possible reconstructions are usually approximated by differences between total energies per projected 1×1 surface unit cell computed in the same computational slab with the desired reconstruction on one face and same reference structure on the other. This approximation is reasonable if the system is sufficiently large, in particular to effectively decouple the two faces. On the other hand, an upper bound on the error in ΔE_s is given by the product of the number of layers times the energy per unit cell of the substrate times the relative accuracy. According to Table 2.3 this amounts to $\approx 0.05eV$.

2.3 Si(111)-2×1 Reconstruction

The Si(111)-2×1 reconstruction which appears on silicon crystals cleaved in UHV at room temperature has been a prototype system for experimental and theoretical studies for many years. It is now well accepted that the π-bonded chain model[58, 59, 60, 61, 62] correctly describes the atomic arrangement of the surface, although details are still being investigated. This surface reconstruction is metastable, it converts to the metastable Si(111)-5×5 reconstruction treated in the preceding section at relatively low temperature of 350^oC[63]. In contrast to the transformation into the stable 7x7 Si(111) reconstruction at 800^oC, the 2x1$\longrightarrow$5x5 transformation requires no long-range diffusion of additional Si adatoms because the average number of Si atoms per unit area is the same as on the truncated bulk (111) surface for both of those structures.

We employed the tight-binding linear scaling method discussed above with Bowler et al's parametrization[34]. A 4×4, 8 layers thick slab with 128 atoms was used in the simulation, with periodic boundary conditions applied along the [111] and [11$\bar{2}$] axes. Two layers of Si atoms and the 16 hydrogen atoms attached to the bottom of the slab were kept fixed. In order to induce the reconstruction some surface atoms were shifted from their bulk positions as shown in Fig. 2.2(a), thus yielding the initial configuration shown in Fig. 2.2(b). Damped molecular dynamics started after electronic relaxation for this initial configuration led to the π-bonded chain structure within the first 200 MD steps; relaxation was continued until the all force components became smaller than the preset threshold value 0.01nN. The corresponding relaxed configuration is shown in Fig. 2.2(c). The present calculation results were analyzed and compared with previous results shown in Table 2.4. Although we obtained the correct geometry, diagonalization in the last configuration gave an energy gap E_g=1eV somewhat larger than the most recent experimental[64] (E_g=0.6eV)

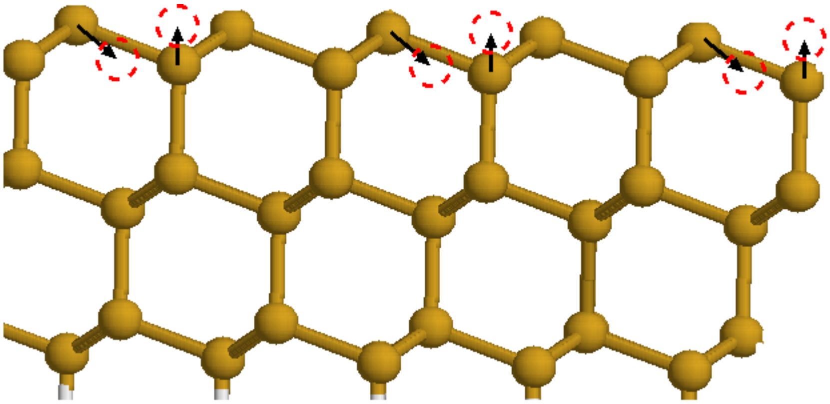

(a) before shifting

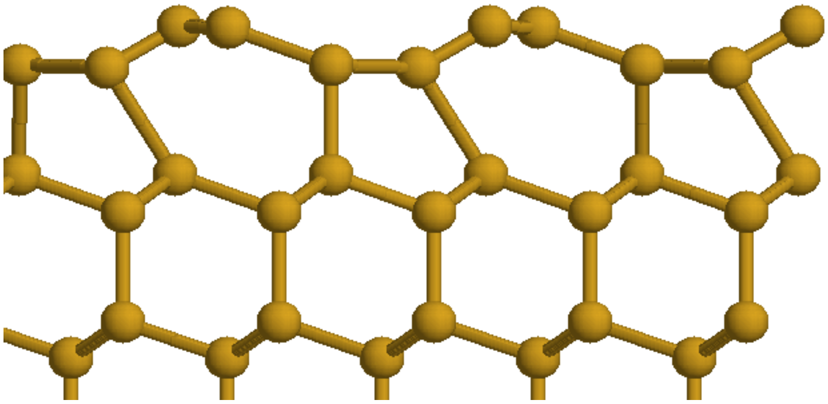

(b) after shifting

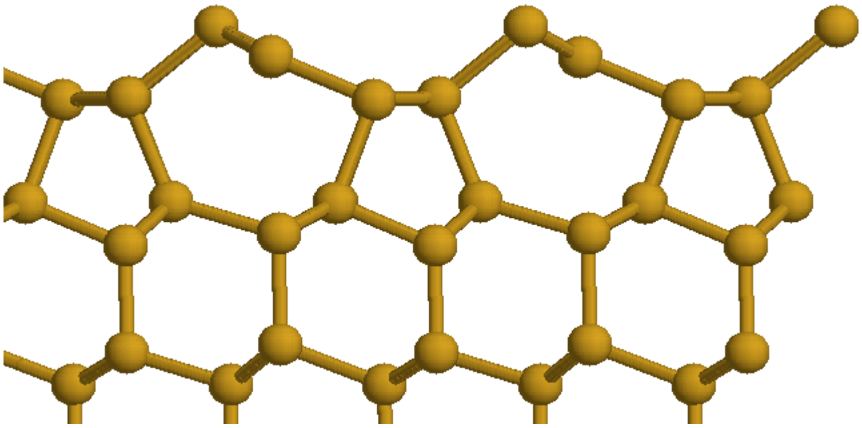

(c) last relaxed configuration

Figure 2.2: Side views of (a) the truncated Si(111)-(1×1) silicon surface, (b) initial configuration, (c) final configuration of 2×1 reconstructed surface.

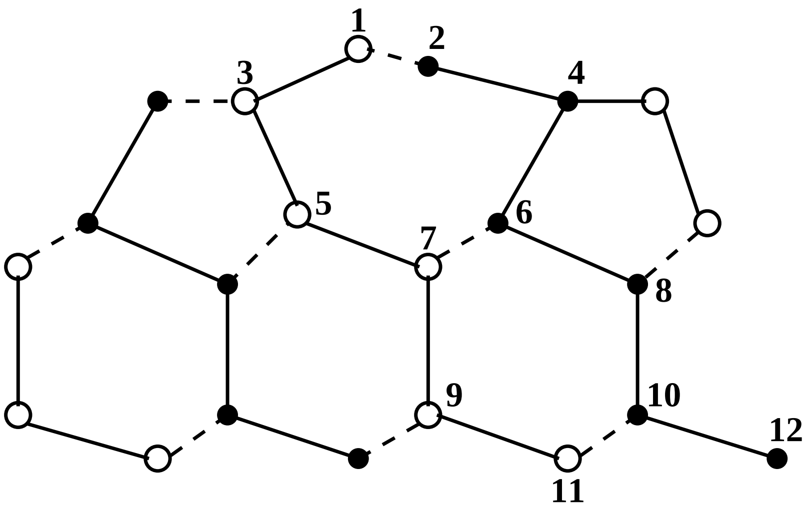

Figure 2.3: Side view of the free layers of the minimized Si(111)-2×1 structure. The atoms 1 and 2 form a π-bonded chain; open and closed circles denote atoms in different $(1\ \bar{1}\ 0)$ planes.

and theoretical[65](E_g=0.69eV) results. We also found that the charge transfer from the upper atoms to the lower atoms is in disagreement with more accurate calculations. Both discrepancies are likely due to the assumed value U_{Si} of Hubbard term(see section 1.3.7).

height	pre sent	Ref. [66]	Refs. [62, 61, 67]	Ref. [68]	Ref. [60, 69]	Ref. [70]
$z_1 - z_2$	0.64	0.47	0.10	0.38±0.8	0.49	0.39
$z_3 - z_4$	-0.05	-0.05	-0.05	-0.07	-0.04	-0.07
$z_5 - z_6$	-0.03	-0.07	-0.08	-0.07	-0.02	-0.07
$z_7 - z_8$	0.26	0.28	0.30	0.20	0.27	0.27
$z_9 - z_{10}$	0.18	0.15	0.20	0.13	0.16	0.15

Table 2.4: Comparison of calculated height differences of the relaxed Si(111)-2×1 structure with previous computations. z_i is the coordinate of i^{th} atom along the surface normal direction (Fig. 2.3)

2.4 Si(001)-c(4x2) Surface

2.4.1 Perfect surface

A truncated 1×1 Si(001) surface as shown in Fig. 2.4(a) contains many unsaturated bonds and the system tends to minimize its energy by reconstructing its surface. Theoretical[71, 72, 73] and experimental[74] evidence shows that this reconstruction causes dimers to appear on the surface; i.e. surface atoms move toward each other to form pairs. Furthermore, these dimers are tilted and asymmetric with respect to terminated bulk. The dimers can arrange themselves in various patterns on the surface and thus several reconstructions of the surface like $p(2\times1)$, $p(2\times2)$ and $c(4\times2)$ are possible and have been extensively studied [75]. Following a period of controversy, several LDA studies, in particular the exhaustive one of Ramstad *et al*[76] have confirmed that the $Si(001)-c(4\times 2)$ reconstructions schematically illustrated in Fig. 2.4(b), and first predicted in a pioneering TB computation[71] has in fact the lowest energy. The $p(2\times 2)$ structure, characterized by identical [110] rows with alternatively tilted Si-dimers, is only marginally metastable, while the 2×1 structure with untilted, symmetric dimers is unstable at low temperatures and 0.1 eV higher in energy per surface atom [76].

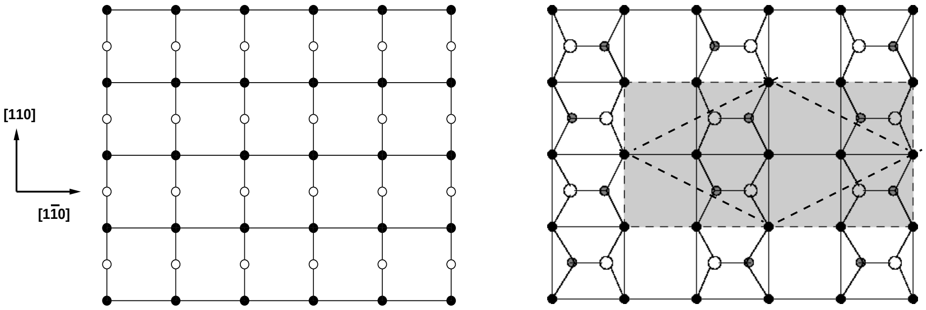

(a) ideal surface (b) reconstructed surface

Figure 2.4: Top views of a) the unreconstructed (bulk truncated) *Si(001)* surface and b) its c(4×2) reconstruction. The shadowed area delimits the surface unit cell used in our simulation. Black circles denote second layer atoms, grey and white circles denote dimerized surface atoms. The white atoms lie higher than their grey counterparts. The primitive c(4×2) surface unit cell is outlined by the dot-dash line in (b).

We performed O(N) computations with Bowler *et al*[34]'s parametrization, n=3 LRs in the 4×2 surface unit cell indicated by shading in Fig.2.4(b). Our computational slab consisted of 6 free Si layers and two fixed layers, with pairs of dangling bonds at the bottom passivated by H atoms in order to approximate a connection to the bulk crystalline silicon substrate. Starting from a configurations with slightly preformed untilted dimers, our computations converged towards a $c(4\times2)$ reconstruction, although the $p(2\times2)$ was obtained in some cases.

As can be seen from Table 2.5, the resulting pattern of atomic displacements is reproduced correctly, the relaxed coordinates being within the spread of values from previous computations. Deviations are more evident in Table 2.6. The dimer tilt, being energetically easy, is quite sensitive to the level of approximation. The deviation of the dimer bond length from the bulk Si-Si distance(2.35Å), in the opposite direction to LDA predictions is more serious and disappointing. Indeed, Bowler *et al*[34] claimed that their parametrization would cure this discrepancy. More extensive computations are needed to check the extent to which the above-mentioned deviations are affected by computa-

Layer	Tight-binding calculations					
	present			Chadi[71]		
	Δx	Δy	Δz	Δx	Δy	Δz
1	0	0.629	0.045	0.	0.46	0.04
1	0	-0.821	-0.383	0.	-1.08	-0.435
2	0.09	0.115	-0.011	0.	0.115	-0.014
2	-0.09	-0.115	-0.01	0.	-0.115	-0.014
3	0.	0.	-0.2	0.	0	-0.12
3	0.008	0.	0.117	0.	0	0.11
4	0	0.023	-0.132	0.	0	-0.07
4	0	0.	0.08	0.	0	0.07
5	0	0.049	-0.01	0.	0.034	0.
5	0	-0.067	-0.31	0.	-0.034	0.

Layer	LDA calculations					
	Ramstad *et al*[76]			Northrup[77]		
	Δx	Δy	Δz	Δx	Δy	Δz
1	0	0.68	-0.05	0	0.61	-0.04
1	0	-0.95	-0.788	0	-1.04	-0.74
2	0.117	0.12	-0.086	0.008	0.1	-0.07
2	-0.12	-0.108	-0.079	-0.008	-0.1	-0.07
3	0	0.009	-0.223	0	0	-0.19
3	0.02	0.003	0.066	0.001	0	0.05
4	0	0.006	-0.154	0	0	-0.12
4	0	0.005	0.069	0	0	0.04
5	0	0.043	-0.03			
5	0	-0.038	-0.03			

Table 2.5: Computed atom displacements from ideal truncated bulk positions (in Å) on the relaxed Si(001)-c(4×2) reconstructed surface

tional approximations and to extract reliable surface energy differences.

A *posteriori* diagonalization gives a 0.9 eV band gap, a value which is reasonable[77], but should not be taken too seriously because the TB parameters are fitted to occupied valence bands and to ground-state properties. The existence of a band gap is consistent with the known semiconducting nature of the c(4×2).

2.4.2 "Type-C" Defect

The Si(001) surface has a rich variety of metastable reconstructions and the properties of lowest surface energy c(4×2) structure has been studied extensively as described in the previous section. This surface also has rich variety of native defects; the typical ones labelled type-A, B and C identified using STM and STS by Hamers and Köhler[78], have been studied both experimentally, as well as theoretically, but controversy remained regarding the structure of the type-

Bonds	present	Ramstad *et al*[76]	Chadi[71]
I	2.425	2.29	2.35
II	2.345	2.31	2.332
III	2.367	2.35	2.390
IV	2.379	2.37	2.398
V	2.377	2.35	2.34
α	10.2^o	18.8^o	11.68^o

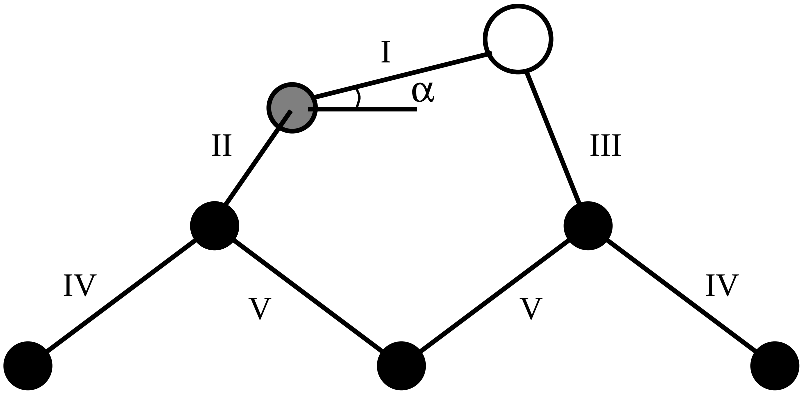

Side view of the tilted dimer and of second and third layer atoms in the relaxed Si(001)-c(4×2) reconstructed surface

Table 2.6: Computed bond lengths and tilt angle of a surface dimer on the Si(001)-c(4×2) reconstructed surface.

C defect. While Hamers *et al* proposed that two adjacent Si atoms along the dimer row are missing, Uda *et al*[79, 80, 81] proposed models with only one atom missing in the second layer. Their LDA, LDA calculations showed that two of the proposed models agree with experimental results.

In our TB calculations we started with structures close to those proposed by Uda and compared the relaxed structures and energy gap with those found on a type-C defect with and without a hydrogen impurity in the above-mentioned LDA calculations and in the STS experiments.

The calculation was carried out using the linear scaling tight-binding method with Bowler *et al*'s parametrization[34] and localized regions encompassing third neighbours. A 8 layers thick 7 × 4 slab was constructed from our previously relaxed c(4×2) slab, the type-C defect was created by removing a silicon atom in the second layer and the dimers on opposite sides of the defect were given same the tilt to ensure periodic boundary conditions. The bottom layer dangling bonds were saturated with hydrogen atoms, the two bottom Si layers and the hydrogen atoms were kept fixed to simulate bulk terminated crystalline silicon.

Removing one Si atom from the second layer creates 4 unsaturated dangling bonds at sites 1, 2, 6 and 7 shown in Fig. 2.5(a), but the dangling bonds on site 1 and 2 are eliminated by relaxation of atoms 1 and 2 toward each other. The dangling bonds at sites 6 and 7 are also eliminated by atom 6 moving

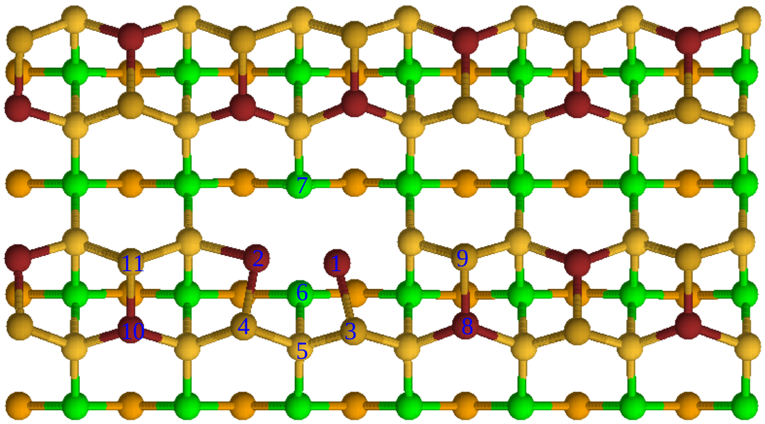

(a) initial configuration

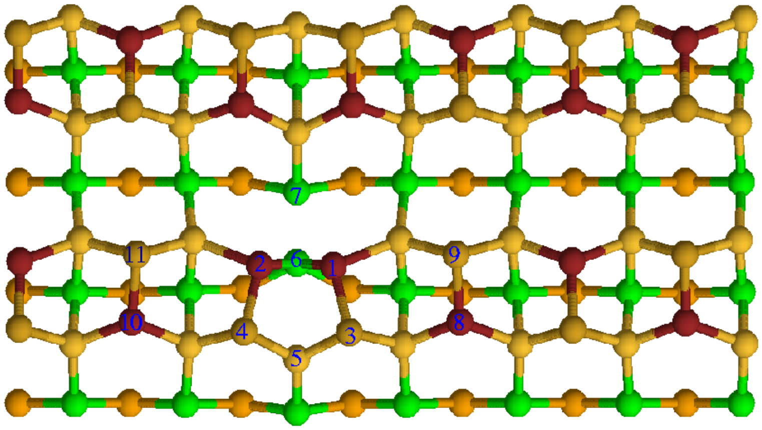

(b) relaxed structure without hydrogen atom

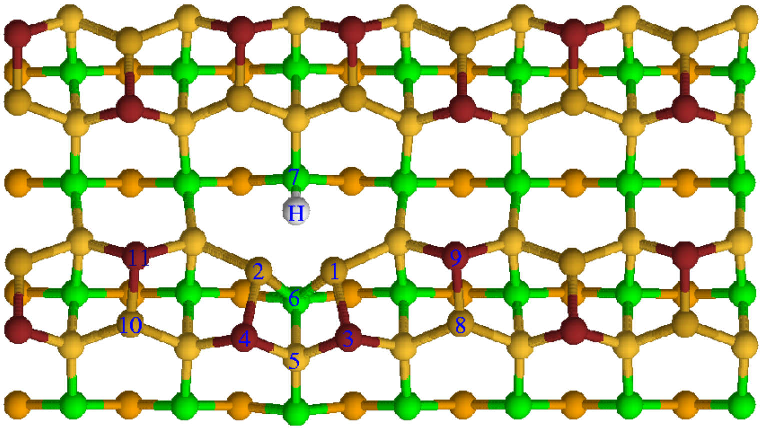

(c) final relaxed structure with hydrogen atom

Figure 2.5: Top views of the relaxed structures of a type-C defect on the Si(001)-c(4×2) surface

towards 7, but the bond between 5 and 6 breaks and creates 2 new dangling bonds. This rebonding scenario around the defect creates a phase break in the buckling pattern along the dimer row as seen in Fig. 2.5(b). The geometry of the converged relaxed structure is compared with the results of Ref. [80] in Table 2.7. The buckling of the surface dimers adjacent to the defect is about 0.53Å and it is not very different from the buckling of the surface dimers which are far away (0.5Å). Our results are encouragingly similar to those of Uda *et al*[80].

The above calculation has been repeated in a 14×4 surface unit cell to check the error created by the finite size of the unit cell; the results showed that the difference is negligible. The energy gap E_g=0.24 eV obtained by diagonalization of the relaxed configuration is in contradiction to the apparent lack of a gap in the STS spectrum at room temperature [78], but it is not very different from 0.3eV gap obtained by Uda *et al*[80] and 0.5eV observed by Hata *et al*[82] in STS at 80K.

	This work				Ref[80]			
(i-j)	Δx	Δy	Δz	d	Δx	Δy	Δz	d
(1-2)	0.027	2.553	-0.0386	2.554	0.002	2.495	0.012	2.495
(3-4)	0.0167	3.627	0.032	3.627	0.007	3.661	-0.009	3.661
(1-3)	-2.280	-0.5417	-0.562	2.410	-2.236	-0.578	-0.558	2.376
(2-4)	-2.290	0.532	-0.492	2.402	-2.231	0.587	-0.579	2.378
(3-5)	-0.932	1.810	1.105	2.317	-0.888	1.835	1.015	2.277
(4-5)	-0.948	-1.817	1.073	2.313	-0.895	-1.826	1.024	2.277
(1-6)	0.0971	1.268	2.261	2.594	0.164	1.245	2.188	2.523
(2-6)	0.070	-1.286	2.30	2.636	0.162	-1.251	2.176	2.515
(6-7)	2.502	0.006	0.021	2.502	2.524	-0.001	0.077	2.525
(6-5)	-3.309	0.001	-1.718	3.728	-3.288	0.012	-1.731	3.716

Table 2.7: Comparison of the relaxed structure of the type-C defect on the Si(001) surface.

In a separate calculation, we have inserted a hydrogen atom at site 7, obtaining the converged structure shown in Fig. 2.5(c). The geometry of this relaxed structure is compared with Ref.[79] in Table 2.8. An energy gap E_g=0.59eV is obtained from a diagonalization of the converged relaxed structure. Hydrogen saturation of the dangling bond above site 7 reduces the reactivity of the defect and induces an energy gap as expected.

2.5 Surface Energies

Based on the total relaxed energies of different slabs and bulk-like slabs of the same size, the surface energies of different reconstructed surface referred to a (1×1) unit area have been estimated. The results are summarized in Table 2.9. From the results we can see that the (111)-5×5 reconstructed surface energy is higher than estimated in Ref. [54]. It is only 0.16 eV lower than the sur-

	This work				Ref[79]			
(i-j)	Δx	Δy	Δz	d	Δx	Δy	Δz	d
(1-2)	0.000	2.587	-0.005	2.587	0.013	2.520	0.004	2.520
(3-4)	0.001	3.608	0.005	3.608	0.007	3.662	0.029	3.662
(1-3)	-2.294	-0.509	-0.495	2.401	-2.257	-0.572	-0.437	2.369
(2-4)	-2.294	0.512	-0.486	2.400	-2.262	0.570	-0.412	2.369
(3-5)	-0.696	1.802	1.372	2.370	-0.960	1.827	1.042	2.312
(4-5)	-0.695	-1.805	1.367	2.369	-0.967	-1.836	1.014	2.310
(1-6)	-1.018	1.292	2.170	2.723	-1.169	1.270	1.933	2.592
(2-6)	1.018	-1.295	2.175	2.728	-1.181	-1.250	1.928	2.583
(6-7)	4.228	0.000	-0.072	4.229	4.097	-0.004	0.124	4.099
(6-5)	-1.972	0.002	-1.294	2.3581	-2.048	-0.016	-1.327	2.440
(H-7)	1.093	0.001	1.082	1.539	1.233	0.000	0.962	1.564

Table 2.8: Comparison of relaxed structures of the type-C defect in the presence of a hydrogen atom at site 7.

face energy of the truncated bulk (111) configuration; this difference is smaller than previous estimates, namely 0.56eV [83, 52] and 0.395eV [53]. Furthermore, our estimated surface energy of the 2x1 reconstructed surface is lower than that of the 5x5. This differences suggest that TB parametrization and non-selfconsistency are delicate issues which should be addressed more carefully. Our estimated surface energy of the Si(001)-c(4×2) surface energy is the same as in Ref. [77], however.

Surfaces		Surface Energies [eV]	
		Our Result	Previous results
(111) surface	ideal	1.48	-
	5×5	1.32	1.17[54]
	2×1	1.19	-
(001) surface	ideal	2.10	-
	c(4×2)	1.39	1.39[77]

Table 2.9: Surface energies of different silicon surfaces.

2.6 [001] Oriented Pyramidal Cluster Tips

Over the past five years, there have been many reports of true atomic resolution on a growing number of materials, in particular on the Si(111)-7×7 surface, obtained with NC-AFM technique. Theoretical and experimental investigations[84, 85, 13] have proven that the short-range chemical interaction plays the main role in achieving true atomic resolution. The quality of the images strongly depend on the sharpness of the probing tip. Although most of the commercially available silicon tips are etched from [001] silicon wafers, one important concern is the apex structure of such tips and their stability.

To clarify these issues we have performed tight-binding molecular dynamics simulations with Bowler et al's parametrization.

2.6.1 Model

An atomically sharp pyramidal tip with {111} facets is constructed with a cluster of up to 95 silicon atoms in up to 9 layers, in accordance with the silicon bulk lattice structure. The silicon atoms in the bottom layer and the passivating hydrogen atoms attached to them were kept fixed. The dangling bonds on the facets of the tip in the next n_H layers, where n_H=0,1,2,3, were also saturated with hydrogen atoms, but these hydrogen atoms were allowed to move. This model tip was placed in the center of a rectangular supercell with a vacuum space larger than the potential cut-off. The calculated forces are used to update the atomic positions as described in section 1.3.6. Two different kinds of runs have been performed: First relaxation with damped molecular dynamics at T=0K and then stepwise heating with a Nose thermostat applied in between up to 800K. The results are presented in the following sections.

2.6.2 Relaxed structures

Starting with the given atomic configuration, electronic minimization with the conjugate gradients method were performed for about 2000 electronic steps until the successive energy differences become smaller than a preset threshold of $10^{-4}eV$. Then damped molecular dynamics was performed with electronic minimization performed at least 5 times for each MD step. The procedure continued until all force components on each atom become smaller than a threshold of 0.01nN. Fig. 2.6 shows the relaxed configuration for n_H=2 at T=0. The dangling bonds on the second layer have formed a weak dimer with an interatomic distance of 2.8Å. The formation of the dimer pushes the apex atom upwards. As we can see from Fig. 2.6 the initial C_{2V} symmetry is broken, but the bonding topology of the apex is preserved although one facet of the tip is flattened while the opposite facet is more corrugated. The C_{2V}-symmetry breaking displacement of the apex atom lowers the energy of the initial configuration by lifting the degeneracy of the two unsaturated dangling bonds at the apex. On the more corrugated facet the protruding atoms have almost the same bond angles and bond lengths to their neighbours as adatoms on the Si(111)-5x5 reconstructed surface. The atoms on the flattened facet stay almost in a plane and have a structure similar to graphite, except for one protruding atom in the middle of the facet.

To see the effect of the hydrogen saturation of dangling bonds on the facets and of system size, we have increased the number of hydrogen saturated layers and the number of silicon layers. The results showed that the change in the relaxed configuration of the tip apex is not significant.

2.6.3 Thermal stability

To check the stability of the relaxed tip, we performed several MD calculations at successively larger values of the temperatures. The temperature was

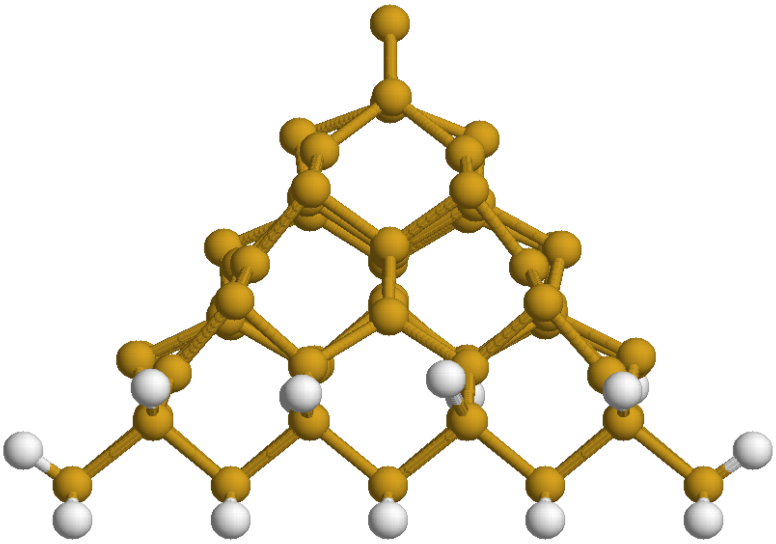

(a) (110) direction view

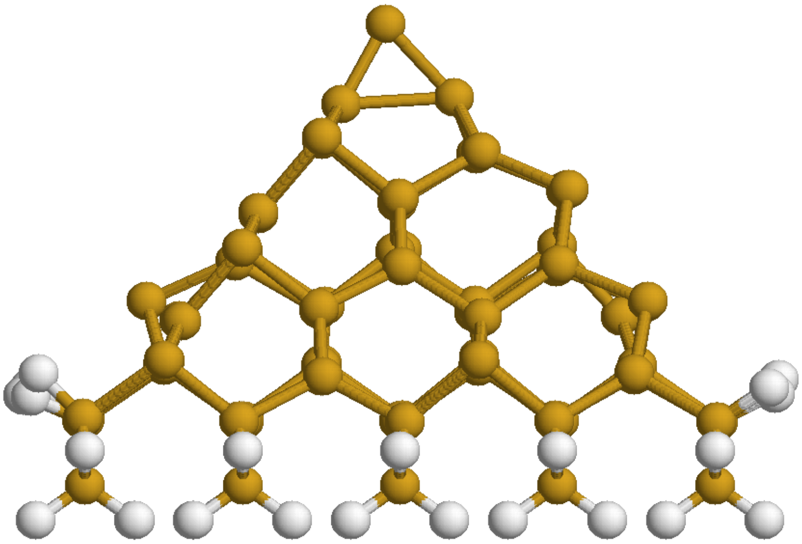

(b) $(1\bar{1}0)$ direction view

Figure 2.6: Relaxed structure of a [001] directed model tip with 9 silicon layers. The silicon atoms in the two bottom layres are saturated with hydrogen atoms. The bottom layer and the attached hydrogen atoms are kept fixed. The initial C_{2V} symmetry is broken, but the bonding topology of the apex is preserved.

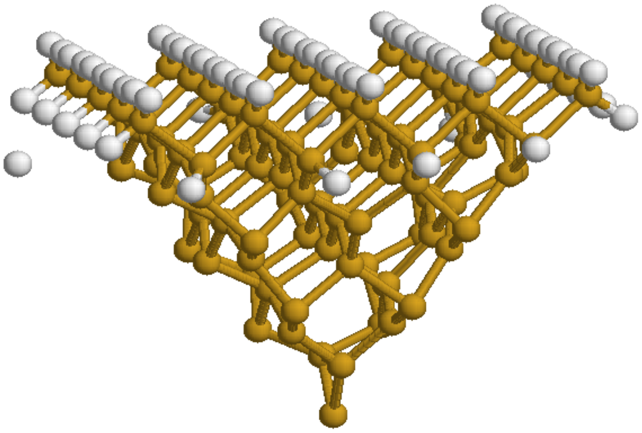

Figure 2.7: Snapshot of the annealed structure of the tip shown in Fig. 2.6 at 800K. The structure is essentially preserved despite appreciable thermal motion of the passivating hydrogen atoms; a few even desorbed.

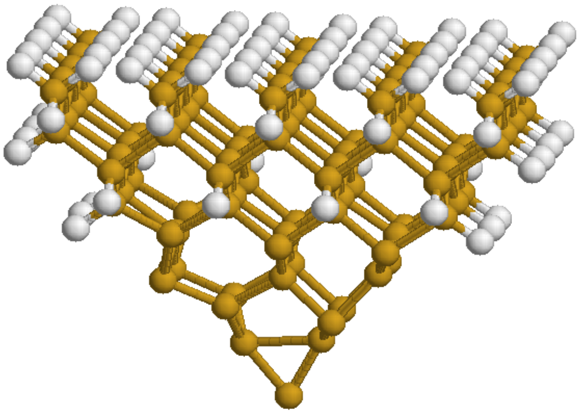

Figure 2.8: Snapshot of the annealed structure of a different [001] oriented tip at 600K. Note that dangling bonds are saturated with hydrogen atoms except on Si atoms in four layers at the top. Except for small thermal motions of Si atoms and significant ones of the free H atoms, the relaxed structure is essentially preserved.

increased stepwise to 800K in steps of 50K with 1000 MD steps performed at each temperature using a Nose thermostat. Because the corresponding time interval (0.4ps) corresponds to just a few typical vibrational periods, it is by no means certain that the system had a chance to make any transition to any lower neighbouring minima, but several bonds were seen to break and form again, especially at the higher temperatures. Nevertheless, the geometry of the original tip did not change significantly. At the highest temperature of 800K we also observed that some H atoms allowed to move desorbed from the facets, as shown in Fig. 2.7. A longer run (∼2ps) at 600K revealed no essential changes compared to the $T = 0$ structure, as illustrated in Fig. 2.8 for $n_H = 4$.

Chapter 3

Molecular Dynamics Simulations of Atomic Force Microscopy — Applications to the Si(111)-7×7 Surface

3.1 Introduction

Following its invention [86] scanning tunneling microscopy (STM)[87, 88, 89, 90] has proven to be very successful when imaging conducting sample. However, it is not able to image non-conducting samples unless they are made conducting by heating or irradiation. Later atomic force microscope(AFM)[91, 1] developed into a useful tool which allows routine investigations of surface structure, albeit on nanometer or larger scales, by probing the spatial variations of the forces between the tip and sample via the deflection of a cantilever. If the interaction force between the tip and sample is kept constant, the sample surface profile can be determined by monitoring the variation of the tip height. Such profiles were originally hoped to be more directly related to surface atomic structures, unlike STM where images reflect the electronic band structure around the Fermi level, e.g. the local density of states at the center of the tip [92, 93]. In principle, AFM can be applied to non-conducting samples as well as conducting samples; for this reason it is an important tool in surface science and many applied fields. But it took quite a while to obtain true atomic resolution, because images taken in the common *contact mode* were not able to clearly resolve individual surface point and line defects since the tip-sample contact area typically encompasses at least several surface and tip atoms. Only the periodicity of the ordered surface lattice of a crystal could be seen. It was impossible to image reactive surfaces like clean semiconductor surfaces in ultra high vacuum(UHV) without wear. Atomic resolution can only be obtained if the tip can approach the surface in the attractive regime without making contact. In such non-contact experiments it is difficult to measure this interaction force accurately while avoiding cantilever jump to contact. In dynamic AFM measurements, the resonance frequency of the cantilever changes locally if the tip starts to be attracted to specific surface sites. It thus became possible to image surface atoms by using a tip oscillation amplitude exceeding the distance of closest approach and maintaining a constant frequency shift Δf via feedback control of the sample perpendicular displacement[2, 3]. This shift can be measured very accurately using frequency demodulation[4]. Jump to contact is avoided by using a large cantilever force constant k and a large tip oscillation amplitude A, such that the restoring force kA considerably exceeds the maximum attractive force F_z at the distance of closest approach, whereas in quasistatic measurements this requires the tip-sample interaction force gradient $\frac{\partial F_z}{\partial z}$ to be smaller than the cantilever spring constant k.

Under the former condition, the tip-sample interaction weakly perturbs the harmonic motion of the tip, so that Δf can be calculated from the force-distance dependence at any particular site, as first pointed out by Giessibl[15].

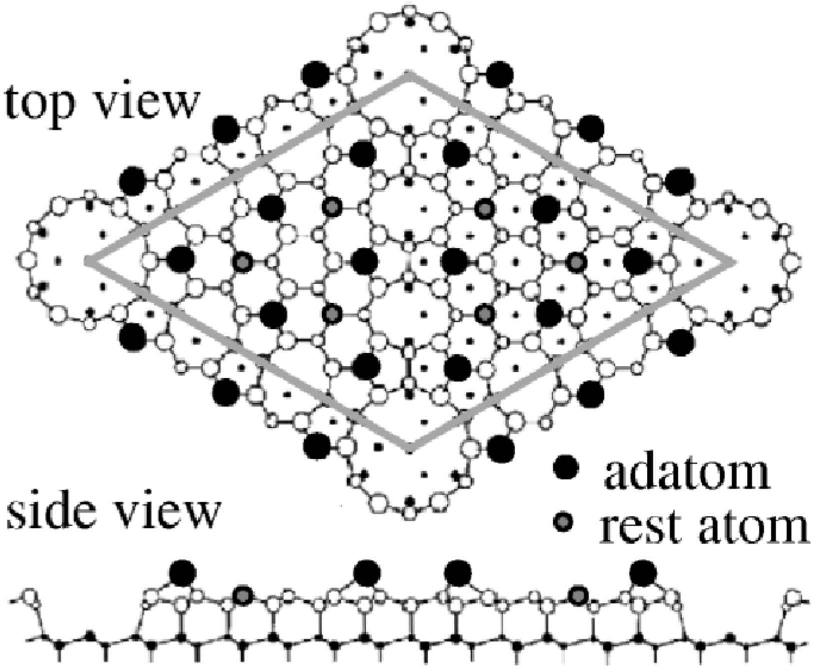

Figure 3.1: Top and side views of Si(111)-7x7 reconstructed surface

Following the pioneering experiments[2, 3], many investigators have obtained atomically-resolved images of the Si(111)-7×7 surface in ultra high vacuum (UHV) using large-amplitude dynamic force microscopy (DFM) under various feedback conditions and different tip materials [5, 6, 7, 8, 9, 10]. These experiments revealed the most characteristic surface features of the DAS model [11, 12], namely the diamond-shaped unit cell with its 12 adatoms and a corner hole, as shown in Fig. 3.1. The images show marked atomic-scale contrast sometimes comparable to the best previous STM images. Quite recently, after the work reported in this chapter, Lantz et al[14] using low-temperature(LT) atomic force microscope (AFM) imaged not only the 12 adatoms but also the 6 rest atoms in between. While there are slight variations in the height differences between the different cell halves and the adatoms, most data at constant frequency shift $\Delta f < 0$ show corner holes imaged lower than the adatoms consistent with a more negative Δf above adatoms in constant height images[14].

Atomic-scale AFM contrast on the Si(111)-7×7 surface has been attributed to a partially filled dangling bond on the tip apex of the atomically sharp tip, which interacts with nearby dangling bonds on the surface adatoms. No irreversible deformations or material transfer presumably occur at separations between tip apex and closest atoms of the surface which exceed the sum of their radii by a few Å , so that their their electrons only weakly overlap[94]. This interpretation was strongly reinforced by the work of Perez et al[13] in density functional calculations which simulated a [111] oriented pyramidal Si tip interacting with a Si(111)-5×5 surface which exhibits same characteristic DAS features as the Si(111)-7×7 surface. The validity of the interpretation has been further confirmed by the above-mentioned LTAFM experiments [14]. Constant height scans at a series of tip-sample distances were used to extract the first measurements of the interaction potential above specific sites. The range and magnitude of the short-range interaction potential above the adatoms was in remarkable agreement with the chemical bonding force calculated by Perez et al[13] except for small systematic deviations attributed to the larger deformation expected for a real AFM tip. This work also indicated that stable imaging at constant Δf could only be obtained when the tip-sample interaction is purely attractive, well below the maximum attractive tip-adatom interaction force. Despite this progress in understanding, there are still many open questions such as the effect of the chemical nature of the tip on the image contrast. Other issues are whether Δf jumps if covalent bond(s) form between dangling bonds at the tip apex and on adatoms of the sample [10], and whether maximum atomic-scale contrast can be obtained at closer separations[10], in a soft intermittent contact mode[7] or even in the range where Δf increases with decreasing tip sample separation[6].

Recently Arai and Tomitori [95] have reported significant variations in AFM contrast on the Si(111) 7x7–surface depending on the frequency set point and the tip–sample voltage. Images taken at large frequency shifts ($\Delta f < -200\,\mathrm{Hz}$) exhibited an inverted contrast, i.e. the adatoms appeared lower than the corner holes. Very recently inverted contrast was also observed by LTAFM at zero voltage [96].

In this chapter we show how relevant information about issues and quantities measured or involved in large-amplitude dynamic force microscopy (DFM) can be effectively extracted from classical molecular dynamics simulations despite the enormous discrepancy in time scales between the tip oscillation and atomic motions. Stable atomic-scale contrast is reproduced in simulations of different scan modes above a critical tip-sample separation. Missing or additional adatoms can be recognized in such scans, although they are less well resolved than native adatoms. Furthermore, we find that inverted contrast in good agreement with the latest experimental results is obtained,when the tip is treated as sharp but non-reactive. By means of dynamic simulations we also show how energy losses induced by interaction with an oscillating tip can be monitored and that they occur even in the non-contact range. Finally we explain why controlled lateral translation of an individual Si adatom by means of an AFM tip should be difficult in view of the very special structure of the Si(111)-7x7 surface.

3.1.1 Relation between frequency shift and interaction force

The tip motion in dynamic atomic force microscopy can be described by the differential equation following which represents the driven oscillation of the cantilever not too far away from its fundamental bending resonance

$$m\ddot{z} + \alpha\dot{z} + k(z - \bar{z}) + F_z[z(t)] = F_0 \cos \omega t \tag{3.1}$$

Here α denotes the damping constant of the free lever and is related to its effective mass m, quality factor Q and resonance frequency ω_0 as $\alpha = \frac{m\omega_0}{Q}$; F_0 and ω are the amplitude and the frequency of the driving force, respectively and k is the force constant of free cantilever. $F_z[z(t)]$ is the tip-sample interaction force which contains the short-range chemical interaction and long-range van der Waals interactions, including contributions due to induced deformations of the sample and/or the tip. Atomic displacements induced by interactions cause the actual separation between the tip apex and the nearest sample atom(s) to be different nominal separations [13, 14]. Furthermore, these displacements will not exactly follow the cantilever. Finally, $\bar{z}$ is the equilibrium tip position which is also shifted by the time averaged tip-sample interaction $\bar{F_z}$. Eq. 3.1 takes into account the interaction-induced dissipation discuss in section 3.6 through the time-dependence of F_z. Alternatively, in a stationary state an implicit average of the energy lost over each cycle can be accounted by an effectively increased $\alpha(z)$ compared to the intrinsic damping α_0 of the noninteracting lever [97].

In the same spirit, if we assume that right on resonance the external driving force cancels the damping term on average and neglect retardation effects, Eq. 3.1 reduces to

$$m\ddot{z} + k(z - \bar{z}) + F_z(z) = 0 \tag{3.2}$$

where $F_z(z)$ is the tip-sample interaction force (including tip and sample deformations) which would be acting if the tip were held at position z. Typical tip oscillation frequencies (<1MHz) being more than 10^7 times smaller than maximum acoustic phonon frequencies of hard materials like silicon (12 THz), it is reasonable to neglect retardation effects. The interaction force is highly nonlinear on the scale of typical oscillation amplitudes, but it is weak, and therefore changes the cantilever resonance frequency from its non-perturbed value f_0 (when $F_z = 0$) only by a small shift $\Delta f < 0$ which depends on the tip sample interaction force-distance dependence and strength. An AFM image is usually obtained by maintaining a fixed value of the frequency shift Δf by means of distance-controlling feedback. This operating mode can avoid the problem of damaging the tip or surface because the tip enters the interaction region only for a short time during each oscillation cycle. The relation between the tip-sample interaction and the frequency shift Δf can in general be obtained by the solving above nonlinear equation numerically. An approximate analytic relation can, however, be obtained in the limit $kA >> F_z$.

In this large amplitude limit which the oscillation waveform practically remains harmonic, and

$$\frac{\Delta f}{f_0} = -\frac{1}{kA} f_0 \int_0^{1/f_0} F_z[z(t)] \cos\phi dt << 1 \tag{3.3}$$

where $\phi = 2\pi f_0 t$, $z(t) = d + A(1 + cos\phi)$, and d is the minimum nominal tip-surface distance. Eq. 3.3 can be obtained by considering F_z as a perturbation and Fourier transforming Eq. 3.2 or by applying the Hamilton-Jacobi formalism[15, 98, 99]. Using $\cos\phi$ as the integration variable one obtains the relation which will be used in section 3.4.4,

$$\frac{\Delta f}{f_0} = -\frac{1}{\pi k A^2} \int_{-A}^{A} \frac{F_z(d + A + \tilde{z})\tilde{z}}{\sqrt{A^2 - \tilde{z}^2}} d\tilde{z} \tag{3.4}$$

Expanding the integrand in Eq. 3.4 about the distance of closest approach and extending the large upper limit to infinity one obtains the further approximation valid if $A >> d$

$$\frac{\Delta f}{f_0} = -\frac{1}{\pi k A} \int_0^{\infty} \frac{F_z(d + z')}{\sqrt{2Az'}} dz' \tag{3.5}$$

In view of the explicit $A^{3/2}$ dependence, Giessibl [15] suggested to compare data obtained in this limit in terms of the quantity

$$\gamma = kA^{3/2} \frac{\Delta f}{f_0} \tag{3.6}$$

For a given distance dependence of the interaction, for instance a power law,

$$U = -\frac{1}{n-1} \frac{C}{z^{n-1}}, \quad F_z = -\frac{dU}{dz} = -\frac{C}{z^n} \tag{3.7}$$

Eq. 3.5 reduces to [100]

$$\gamma = \frac{\Gamma(n - 1/2)}{\sqrt{2\pi}\Gamma(n)} \frac{C}{z^{n-1/2}} = \frac{\Gamma(n - 1/2)}{\sqrt{2\pi}(n-1)\Gamma(n)} \sqrt{UF_z}|_{z=d} \tag{3.8}$$

In the case of an exponentially decaying interaction with range $\lambda = \frac{1}{k}$

$$U = F_0 \frac{e^{-kz}}{k}, \quad F_z = F_0 e^{-kz} \tag{3.9}$$

Eq. 3.6 reduces to

$$\gamma = F_0 \frac{e^{-kz}}{\sqrt{2\pi k}} = \frac{1}{\sqrt{2\pi}} \sqrt{UF_z}|_{z=d} \tag{3.10}$$

The relation between γ and $\sqrt{UF_z}$ at the distance of closest approach was derived heuristically [101, 102] and then as a consequence of Eq. 3.5 in the large amplitude limit [100].

In the small amplitude limit ($A << d$), Eq. 3.2 reduces to

$$\frac{\Delta f}{f_0} = -\frac{1}{2} \frac{\partial F_z / \partial z}{k} \tag{3.11}$$

$\frac{\partial F_z}{\partial z}$ is the force gradient at $z \simeq \bar{z}$. This can be derived by approximating F_z by the first two terms in its Taylor expansion and substituting the equilibrium condition.

3.2 Relevant Experimental Facts and Issues

Owing to its characteristic features, the Si(111) 7x7–surface has been extensively studied using a variety of dynamic AFM modes and tip materials. Here we discuss some experimental results which are directly relevant to our MD simulations.

Recently Arai and Tomitori [95] reported a study of the dependence on the preset frequency and tip–sample voltage of the AFM image contrast on the Si(111) 7x7–surface. The experiments were performed using a silicon cantilever with a spring constant k=20 N/m, a resonance frequency f_0=240 kHz and an oscillation amplitude A=5 nm. When a voltage on the order of –2 V was applied to the sample, the additional attractive electrostatic force allowed stable imaging at large frequency shifts, down to –500 Hz. For $\Delta f = -77$ to -200 Hz, they obtained images similar to those described previously. However, images obtained at $\Delta f < -200$ Hz, exhibited an *inverted contrast.* They also observed inverted contrast even under zero applied bias at $\Delta f \approx -180$ Hz.

In recent low-temperature experiments performed in Basel which we helped to interpret[103], imaging was performed in the dynamic mode using a very sensitive digital phase–locked loop frequency detection scheme in which the cantilever is driven on its resonant frequency at a constant tip oscillation amplitude of 5 nm. A similar cantilever with $k = 30$ N/m, f_0=158178.3 Hz, $Q = 930000$ was used. At first, only weak contrast was observed (lower part of Fig. 3.2a). An abrupt improvement in contrast occurred while the tip was scanned over a bright protrusion (see arrow in Fig. 3.2a). Following this event imaging was noisy; however, with continued scanning at a somewhat reduced frequency set point, stability improved significantly and high quality images were obtained (see Fig. 3.2b). The contrast is similar to that commonly reported, i.e. the tip–sample spacing is increased above the adatoms so that they appear higher than the corner holes. The height difference between these features was dependent on the preset frequency shift, with larger corrugations observed at more negative frequency shift. Moreover, these features are expected to depend on the structure of the tip apex. In Fig. 3.2b, an overall difference of 1.2 Å was observed. This normal *contrast* is thought to result from the onset of chemical bonding between a reactive dangling bond on the tip apex interacting with the reactive adatoms [14, 103].

After obtaining several images, the tip unintentionally crashed into the surface. The tip was then retracted and re–approached. Images were taken at increasingly lower frequency setpoints, until atomic–scale contrast was obtained. Initially the corner holes and half unit cells could barely be distinguished, as in the lower part of Fig. 3.2a. At $\Delta f = -54$ Hz, the contrast was weak and appeared inverted relative to Fig. 3.2b, i.e. the adatoms appeared as local minima. At $\Delta f = -80$ Hz, we observed a stronger *inverted contrast* (Fig. 3.3a), but stable imaging was difficult to maintain. In general, inverted contrast images appear noisier and more prone to tip changes than when normal contrast was obtained. The total height difference is lower in the inverted contrast image, 0.75 Å compared to 1.2 Å, and the adatoms appear narrower. Furthermore, weak minima are observed above the rest atom sites. With continued imaging,

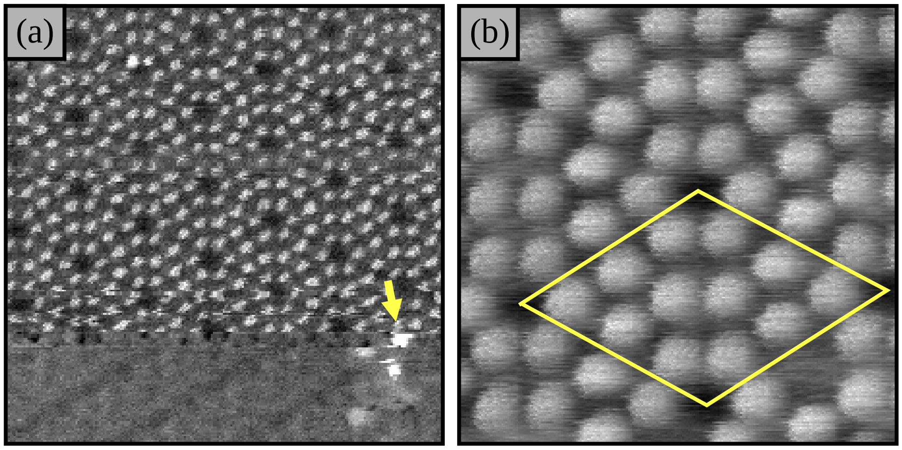

Figure 3.2: (a) $17 \times 17\,\mathrm{nm}^2$ constant frequency shift image ($\Delta f = -48\,\mathrm{Hz}$). (b) $6 \times 6\,\mathrm{nm}^2$ constant frequency shift image ($\Delta f = -42\,\mathrm{Hz}$). The outline of the unit cell is indicated by the white diamond

normal contrast was again obtained (see Fig. 3.4a) following another abrupt tip change. The corrugation observed in Fig. 3.4a (0.8 Å) is significantly smaller than that observed in Fig. 3.2b, despite the fact that it was acquired at a more negative frequency shift. It is likely that the reduced corrugation results from an increase in the contribution of the van der Waals force to the frequency shift, due to an increased tip radius after the tip crash [104]. Following the acquisition of Fig. 3.4a, the tip crashed during attempted frequency distance measurement, after which inverted contrast was again obtained(Fig. 3.4b).

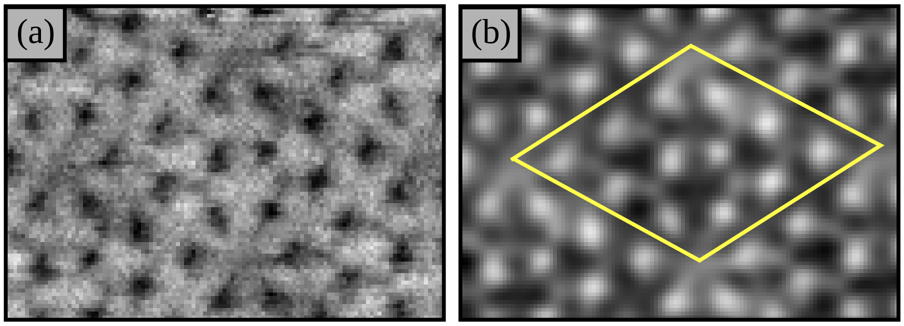

Figure 3.3: (a) Inverted contrast image obtained after a tip crash ($\Delta f = -80\,\mathrm{Hz}$). To facilitate comparison with Fig. 3.2, the data of (a) has been low–pass filtered and the gray scale has been inverted in (b). The outline of the unit cell is shown with a white diamond.

In the experiments reported here, it is believed that the initially untreated, oxidized tip could not form a covalent bond with the reactive adatoms on the surface. The contrast in Fig. 3.2b and Fig. 3.4a probably results after one or more silicon atoms are picked up by the tip, making its apex chemically reactive, i.e. the normal contrast is due to a strong short–range attractive force near each adatom. We hypothesize that the inverted contrast in Fig. 3.3a and Fig. 3.4b

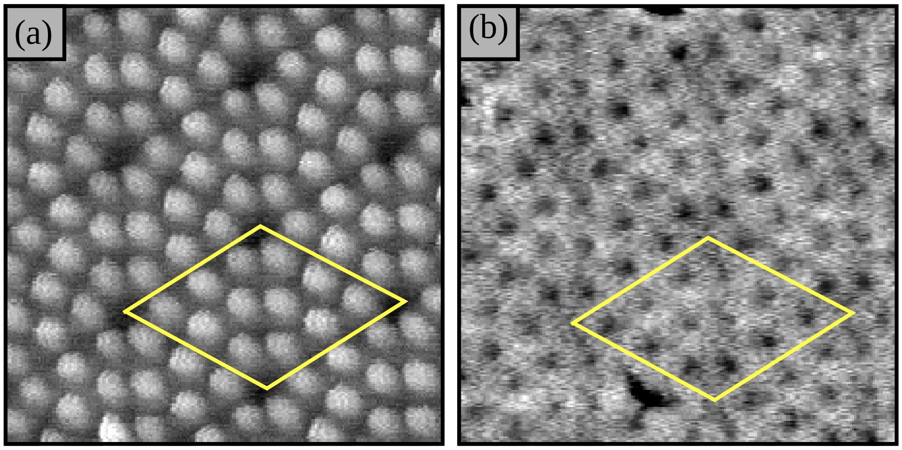

Figure 3.4: (a) Normal contrast obtained after a tip change similar to that shown Fig. 3.2a ($\Delta f = -74\,\mathrm{Hz}$) (b) Inverted contrast image obtained after a second tip crash. ($\Delta f = -120\,\mathrm{Hz}$) The outline of the unit cell is indicated by a white diamond [96].

results when the apex atom of the tip is not reactive, i.e. cannot form a chemical bond with any adatom. In this situation, the net force can still be attractive due to the van der Waals interaction, however, above each adatom an additional short–range repulsive force arise at small tip–sample separations. When these short range forces are probed, the net frequency shift at a given height above an adatom is reduced and the feedback must decrease the tip–sample spacing in order to increase the van der Waals contribution and keep the total frequency shift constant. Therefore the adatoms appear lower than their surroundings. For stable feedback operation in this situation, the net frequency shift must vary monotonically, i.e. must still become more negative as the tip–sample spacing decreases. Arai and Tomitori [95] argued that inverted contrast would arise even in the presence of chemical bonding at tip–sample separations below the crossing of the Δf versus distance curves above an adatom and a corner hole. In contrast to their assumption, this crossing (which is independent of the essentially site independent long–range interaction) actually occurs at even smaller tip–sample separations (see Fig. 3 of [14]). Non–destructive imaging at such close separations is extremely unlikely.

All the images discussed previously refer to perfect areas of the surface. The Si(111)-7×7 surface also exhibits surface point defects, steps and kinks. We focus our attention on the typical point defects, i.e. missing and extra adatoms which have also been observed in other areas otherwise exhibiting normal contrast (Fig. 3.5).

As already mentioned, in dynamic AFM experiments, an additional damping, induced by a delayed deformation response, can arise. This damping is site-dependent and it is possible to obtain an other surface image if the strength of the cantilever excitation required to keep A constant plotted against the lateral position on the surface. As an example, in Fig. 3.6 we will show simultaneously recorded images by Lüthi et al [8]: Fig. 3.6a shows the topography, Fig. 3.6b

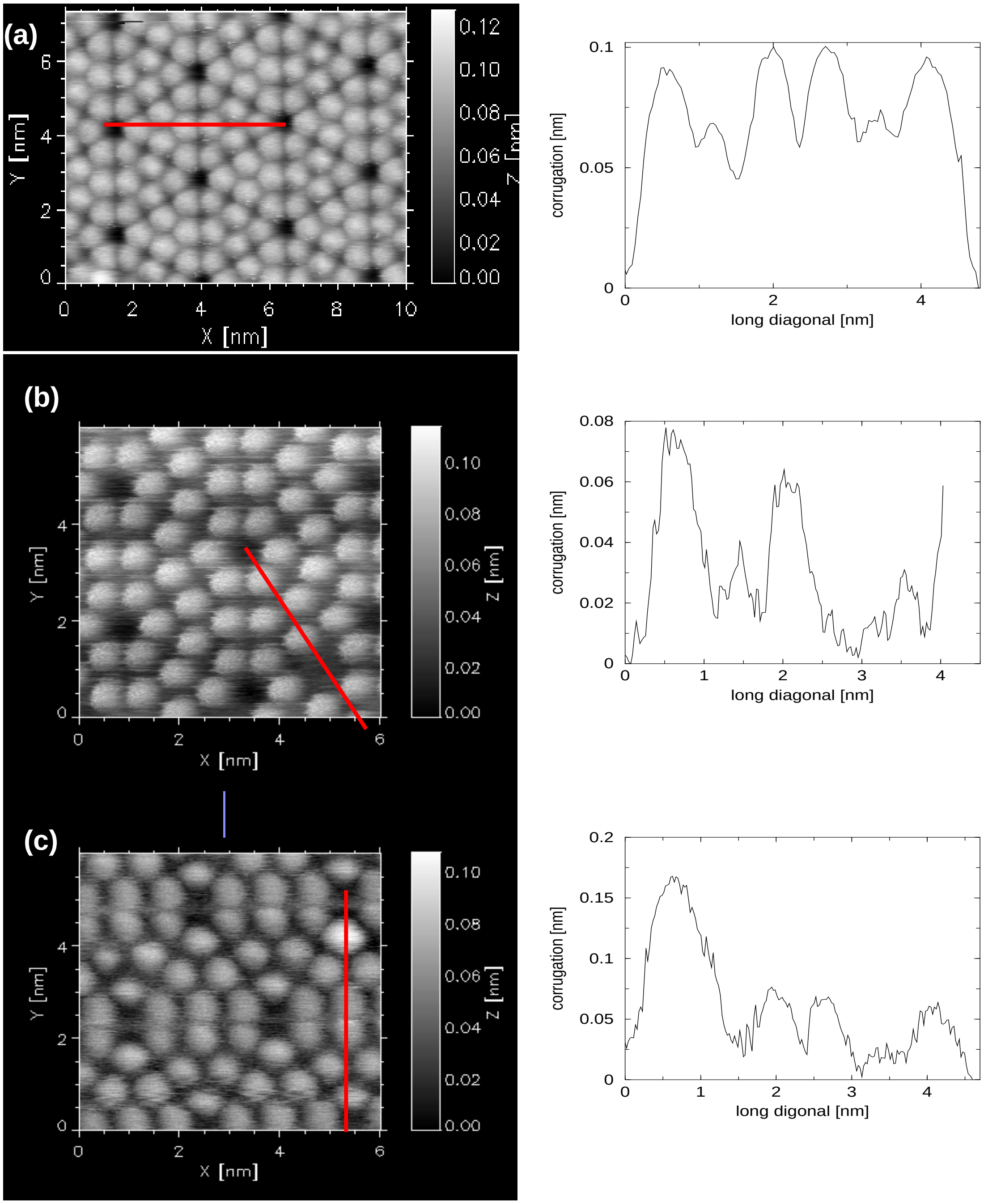

Figure 3.5: Constant frequency shift images of the Si(111)-7×7 surface taken in ultra high vacuum at 7.2K, (a) perfect sample, (b) with a missing adatom, (c) with an extra adatom(unknown species). Sections along the indicated lines are also included (courtesy of M. Lantz).

the average tunneling current and Fig. 3.6c the damping. Comparing Fig. 3.6a and Fig. 3.6c we notice that the damping image is inverted with respect to the topography, namely the highest damping is observed above the corner holes and

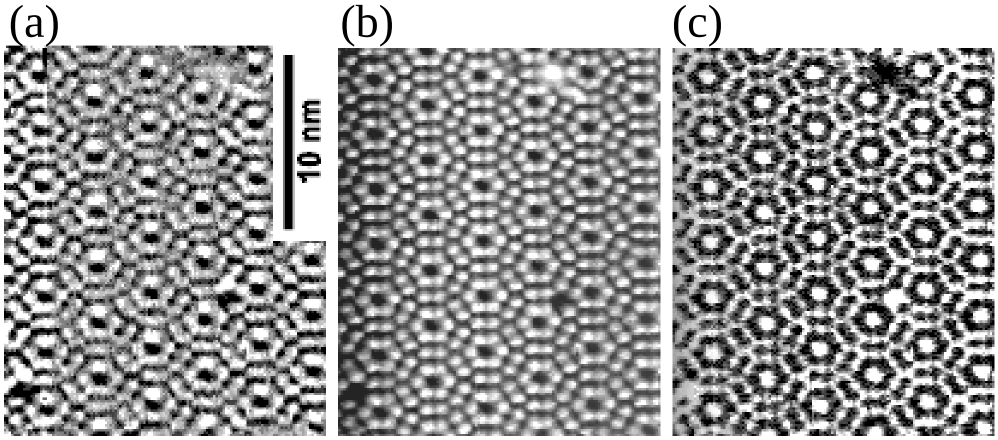

Figure 3.6: The first simultaneously recorded images of the Si(111)-7×7 reconstructed surface taken at room temperature; (a) topography (b) time averaged tunneling current(c) damping(cantilever excitation amplitude required to keep the tip oscillation amplitude constant).

the lowest is above adatoms. However, recent experiments obtained the highest damping above adatom site [103].

In the following chapters we will describe our MD simulations and compare our results with experimental ones.

3.3 The Model

The Si(111) sample is represented by a slab of eight layers with atoms coupled via the well-known short-range Stillinger-Weber (SW) potential (section 1.2.2). Periodic boundary conditions are applied laterally to a nearly square supercell encompassing four 7×7 unit cells. Atoms in the two bottom layers are fixed in bulk-like positions. Atoms in the following layers are allowed to move. The Si(111)-7×7 reconstruction is initiated by removing and shifting atoms in the top three layers, in particular by placing adatoms in the top layer so as to approximately reproduce the geometry of the dimer-adatom-stacking fault(DAS) model[11]. Dimers were not forced to occur but spontaneously formed during equilibration (section 1.5.2) between faulted and unfaulted half-cells in the third, layer and adatoms equilibrated 2.7Å away from their second layer neighbors shortly after molecular dynamics was started. Top and side views of the relaxed sample are shown in Figs. 3.7 and 3.8. Subsequent simulations were initiated with this equilibrated structure.

The coordinates of all moving atoms are updated according Newton's law, using the 5^{th}-order Gear predictor-corrector algorithm[16] (see section 1.3.2) with a time step Δt=0.4fs, as advocated by Stillinger and Weber[19]. The average kinetic energy, i.e., the temperature, is controlled by a Berendsen thermostat (section 1.5.4). The thermalization time τ_T is chosen such that the coupling to the thermostat is weak, as described at the end of this section. In the limit

$T_0 = 0$, the procedure in question reduces to damped molecular dynamics, which can be conveniently used to find relaxed metastable configurations, e.g. upon introducing defects like missing or additional adatoms. Because the SW potential led to some surface diffusion at room temperature (which is not realistic), the setpoint temperature T_0 was kept at 100K in most runs to ensure only small oscillations about the 7×7 equilibrium structure.

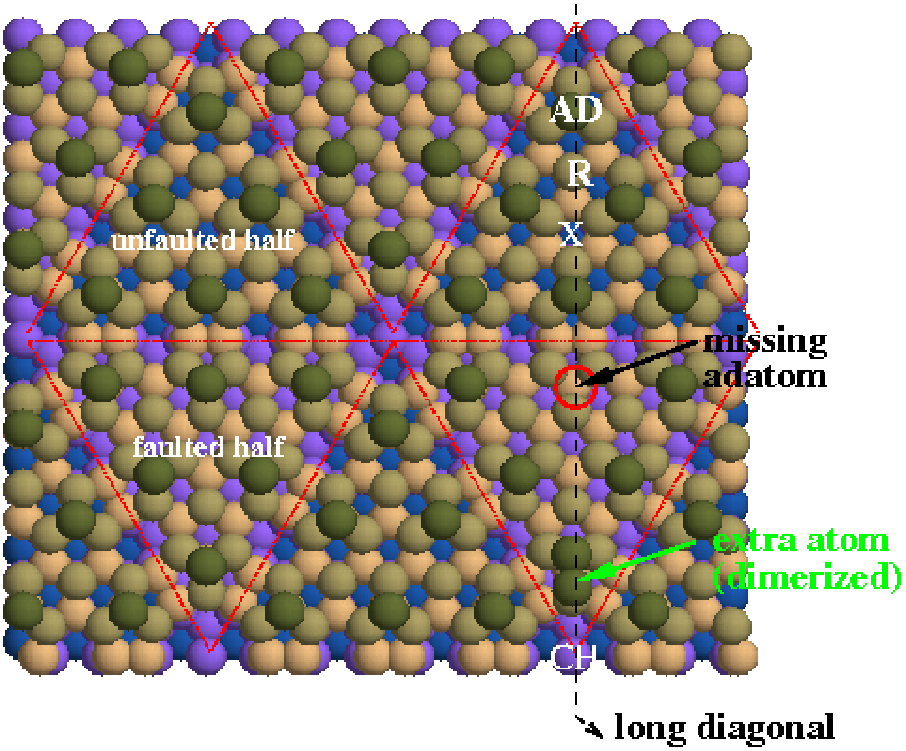

Figure 3.7: Top view of the simulated sample(color). Atoms in different layers are represented with different colors. The relaxed extra adatom and missing adatom positions are highlighted by arrows.

To include short-range chemical tip-sample interactions, which presumably give rise to atomic-scale contrast in the non-contact regime, we first model the tip by a single silicon atom, then by sharp pyramidal silicon cluster with 4 or 6 layers (13 or 34 atoms). Like AFM tips etched out of Si [50], it has a [001] axis as shown in Fig. 3.8. As discussed in the preceding chapter, in a separate tight-binding molecular dynamics investigation, we have shown that such tips are distorted but preserve their bonding topology and overall shape if the base layers are fixed and passivated. In present the study all tip atoms are kept at bulk-like positions in order to isolate effects due to sample deformation and dynamics. Because the SW potential vanishes beyond 3.8Å, as seen in Fig. 3.9, the pair part of a potential[20] fit to a first-principles computation of the interaction between Si(111) layers was added when considering the interaction between the tip and sample atoms in the case of normal contrast. The resulting tip-sample interaction has a decay length λ=0.8Å close to that found in a recent first-principles calculations of the interaction between a silicon cluster

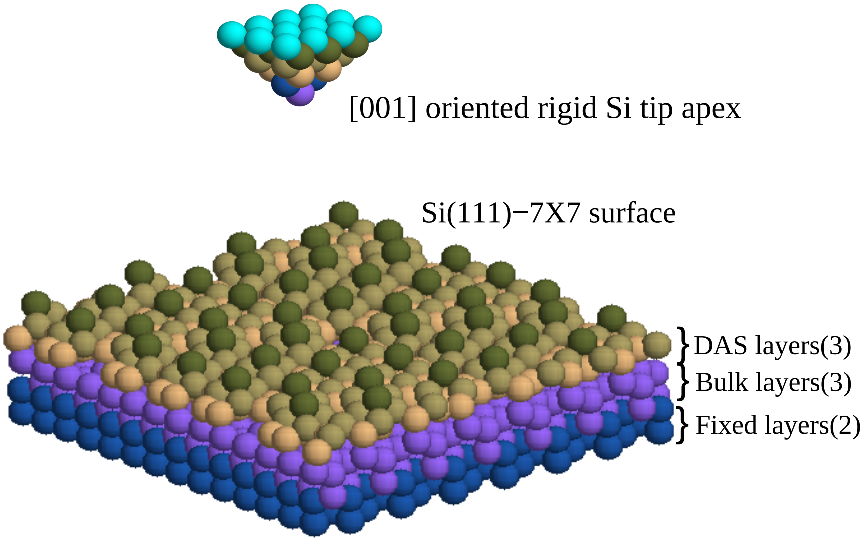

Figure 3.8: Side view of the simulated sample together with the model tip. The color representation is the same as in Fig. 3.7.

tip and a Si(111) surface[13]. We also made a few computations with the above pair potential adjusted to reproduce the Morse fit to the interaction above a central adatom obtained by Perez et al [13]. Compared to Ref.[13], the force F_z computed for the same [111]-directed Si_{10} tip above a rest atom using our potential exhibits a similar decay but a somewhat stronger attraction. Similar values are obtained with the [001]-directed model tip shown in Fig. 3.8 which was used in most of our simulations. Because the net short-range interaction is dominated by the closest tip and sample atoms, force-distance curves computed above an adatom lie close together, independent of the shape and height of the model tip.

To model interactions with passivated atoms or a chemically unreactive tip, we included only the repulsive part of the two-body potential whith readjusted parameters as discussed further in section 3.5.

One important concern is the huge discrepancy between practical times for simulations and those relevant ones in DFM experiments, e.g. the scan velocity (100 m/s vs. 100 Å/s) or the tip oscillation period $1/f$ (few ps vs. few ms). To obtain meaningful results these parameters must be chosen significantly smaller than the sound velocity and the lowest natural frequency (see below) of the finite simulated sample, respectively.

To control the temperature, a Berendsen thermostat[46] is used. It has the advantage of not leading to strong oscillations as the Nose-Hoover method[47, 48]. To maintain the internal energy of the sample constant on the average, the thermostat must react fast enough to compensate any energy transfer induced by the imposed motion of the tip. On the other hand the time constant τ_T (see section 1.5.4) should be so long that the vibrational spectrum of the sample is not appreciably distorted. A reasonable compromise is to choose $2/\tau_T$ comparable

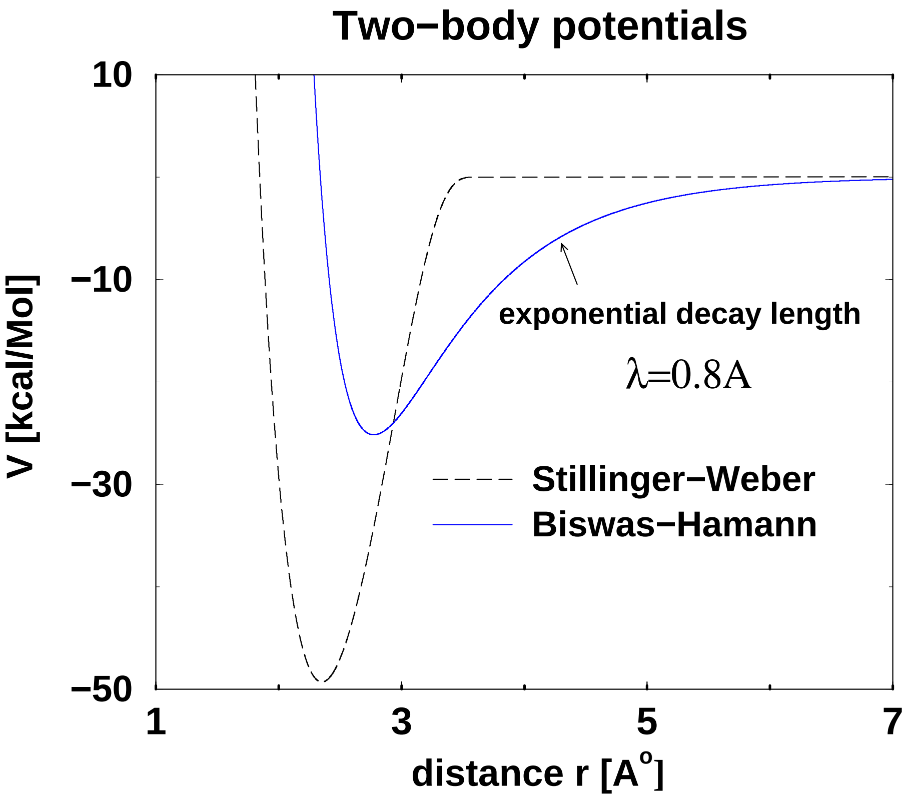

Figure 3.9: Components of the short-range, two-body interaction potential between Si atoms.

to the average difference between the frequencies of the discretized acoustic modes of out finite slab, i.e.

$$c_z \tau_T \simeq 4 N_z a_z \tag{3.12}$$

for mechanical thickness oscillations. Here c_z, N_z and a_z are the longitudinal sound velocity, the number of free layers and their spacing along the [111] direction. Substituting $c_z = 9360$ m/s, $a_z = 3.11$Å, $N_z = 6$, Eq. 3.12 leads to $\tau_T = 0.8 \times 10^{-12}$s. In our simulations we used values of $\tau_T / Deltat$ between 100 and 1000. Typical temperature variations obtained for $\tau_T = 400\Delta t$ are shown in Fig. 3.10; They exhibit small irregular oscillations about the setpoint value with a frequency corresponding to the lowest thickness vibration of the finite slab.

3.4 Different Types of Molecular Dynamics Runs

Simulated, non-contact atomic force microscopy images or scanlines at a constant value of any quantity depending on the tip-sample interaction, e.g. at constant height, constant force or constant frequency shift, can be reconstructed from a close series of quasistatic approach curves. Constant height scans can be simulated directly, but a feedback algorithm is more convenient for constant

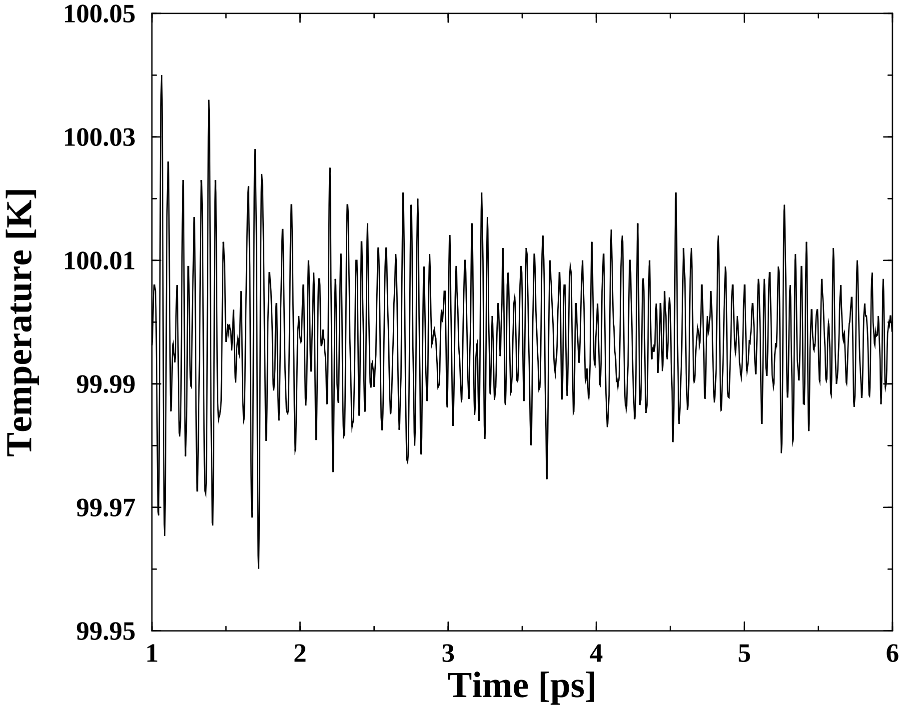

Figure 3.10: Temperature fluctuations of the free sample following equilibration at 100K.

force scans. The third mode also be simulated with a feedback using the approximate relations Eq. (3.8) or (3.10) between $\gamma = kA^{3/2}\frac{\Delta f}{f_0}$ and the geometric mean of the interaction potential and force $\sqrt{UF_z}$. It is otherwise tedious to perform constant Δf simulations directly. As in experiments, in our simulations the tip-sample distance is controlled by a feedback algorithm which attempts to null the difference between the instantaneous force or $\sqrt{UF_z}$ and a setpoint value. The feedback time constant τ and scan velocity v can be chosen so that no significant difference occurs between forward and backward scans, at least in the non-contact regime.

We were able to identify typical surface features and point defects in different operation modes. Since the long diagonal of the Si(111)-7×7 reconstructed surface crosses characteristic features of this surface, i.e. adatoms, rest atoms, corner holes, all horizontal scans were performed along the long diagonal.

In the following subsections we discuss particular aspects in detail.

3.4.1 Monitored and plotted quantities

In order to track possible temperature and/or tip-induced atomic jumpings, in each simulation we recorded 20 to 50 snapshots of atomic positions, and plotted the time evolution of the following quantities: the temperature, the center-of-mass of all moving atoms, the coordinates of the tip apex and of selected adatoms, components of forces on the tip and on those adatoms, the work done on the tip and the heat transfer to the thermostat. The last two quantities are important for the determination of tip-induced energy losses [8], as well as for quantifying friction and wear in the contact or tapping mode, but the latter are not considered here. In order to reduce noise due to fast vibrations excited thermally or by tip-induced atomic jumps, plotted quantities were first averaged over several increments using a normalized binominal distribution of weights.

3.4.2 Missing and additional adatoms

One of the main advantage of NC-AFM is it can resolve point defects, e.g. missing and extra atoms on the Si(111)-7x7 surface [5], presumably thanks to an atomically sharp tip. To compare our results with experiments, we performed some simulations with point defects. Before making any scans we first set up samples with surface point defects.

We created representative point defects by appropriately changing the initial sample configuration and then letting it equilibrate. A missing adatom was created by removing a central adatom, and an extra adatom was created by placing an additional one at one of lowest energy surface sites, e.g. H_3[105] which is next to a corner adatom on the relaxed perfect sample, as shown in Fig. 3.7. These two point defects are shown together in the same figure, although they were created created in two different runs. Removing a central adatom creates dangling bonds on the three atoms in the next layer which are attached to the removed adatom. They relax 0.05Å towards vacuum; the interatomic distances expand about 0.1Å , but the overall geometry and symmetry are preserved around the defect. After an extra atom was inserted into the H_3 position, we observed that the extra atom and one neighboring intrinsic adatom formed a dimer at almost equal height. The dimerized adatoms are also shifted laterally (mostly along the y direction), but the next layer atoms almost preserved their original coordinates.

3.4.3 Quasistatic approaches and retractions

Theoretical modeling allows one to obtain a good estimate of the distance range where stable imaging can occur for a given surface and tip. Before performing or reconstructing any scans, we first determined the minimum distance for non-contact operation at characteristic surface sites of the 7×7 surface. The definition of the minimum distance for non-contact AFM is a delicate issue which merits further investigations because it is strongly depends on the assumed tip-sample interaction. Unless stated otherwise, the results reported here pertain to the short-range interaction described by the sum of the pair potentials shown in Fig.(3.9) plus the SW three-body term(section 1.2.2). It is natural to define z_c as the distance below which irreversible atom jumps, either vertical or lateral (or both) happen. Such jumps lead to hysteresis in force-distance characteristics.

To identify the highest z_c we performed a slow approach above an adatom because it protrudes the most and then retracted the tip from different minimum approach distances. Only the short-range chemical interaction need be included since the macroscopic van der Waals interaction is site-independent in the Hamaker approximation. A particular example of approach and retraction curves recorded at 200 m/s is shown in Fig. 3.11. The retraction curve exhibits a stronger attraction, i.e. we observe a hysteresis, but no global irreversibility, i.e. the tip and sample return to their initial configurations. It is important to keep in mind that the distance z on the horizontal axis is between the apex atom of the tip and the adatom in the absence of the tip. Looking at tip-induced displacements, we notice that the adatom jumps by about 0.5Å towards the apex once $z < z_c \simeq 3.6$Å, upon retraction, the adatom returns to the surface only once $z \simeq 4$Å, however. This behavior is clarified in section 3.7. The rather smooth curves shown in Fig.(3.11) were obtained upon averaging over a significant number of points(section 3.4.1). If only a few points are used, the approach and retract curve exhibit much steeper slopes at the above-mentioned values of z, followed by more pronounced oscillations which are excited by the adatom jumps. The hysteresis gets stronger as we retract the tip from a smaller tip-sample distance. Eventually the adatom is deflected sideways and irreversibly attached to the tip. Pickup of the outermost tip atom, although possible in principle, is perevented by our assumption of a rigid tip. For the weaker interaction reproducing the fit by Perez *et al.* [13], z_c lies closer to the sample than the point of maximum attraction. Owing to time limitations, only a few simulations could be performed with this probably more realistic interaction.

At other positions, even if the tip is above nominal high-symmetry sites surrounded by several adatoms, e.g. rest atoms, z_c is smaller than above an adatom and the first instability occurring upon approach involves a jump of one or a few of the nearest adatoms and results in appreciable lateral force components (1 to 3 nN) on the tip. Furthermore, these atoms typically remain attached to the tip upon retraction. Such tip-induced rearrangements also depends on the tip orientation. As we described in section 3.7, the maximum tip-induced relaxation above an adatom is about 0.7Å . Note once more that we did not consider tip deformations which might also be important [14, 103] and even change the behavior qualitatively.

Tip-induced relaxation also leads to energy dissipation in the case of an oscillating tip. We discuss this issue in detail in section 3.6.

3.4.4 Construction of different scans from quasistatic force distance characteristics

According to the perturbation theory [15, 106] sketched in section 3.3, a normalized frequency shift independent of k can be computed in the non-contact range from the z-dependence of F_z (including possible reversible deformations). In the large amplitude limit $A >> d$, constant Δf approximately corresponds to constant $F_z(d)$ at the turning point $z = d$. Quasistatic force-distance characteristics similar to those discussed in the previous subsection were obtained by approaching the tip at a constant velocity $v_z << v_c = \lambda f_{max} \simeq 1000 m/s$, λ being the decay length of the interaction, $f_{max} = 16THz$ being the highest natural frequency of our system (adatom vibration against neighboring atoms). Such approach curves are then essentially v_z-independent and reversible down to a site-dependent separation z_c, apart from residual thermal fluctuations such

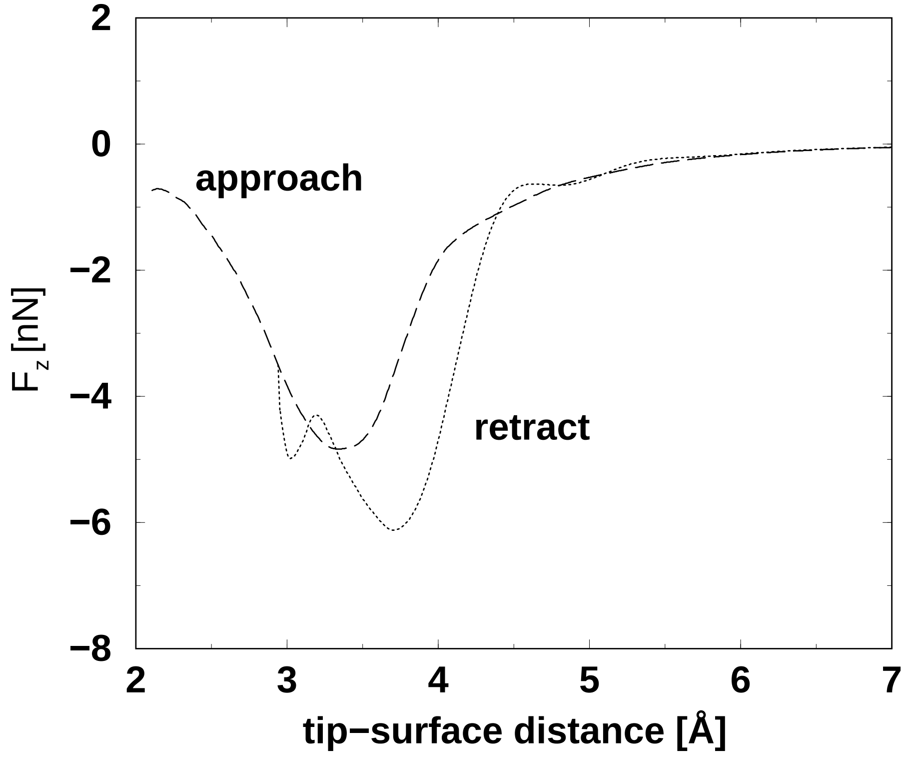

Figure 3.11: Approach and retraction force-distance curves above an adatom site(see text).

as those apparent in the retraction curve in Fig. (3.11).

Force-distance characteristics recorded with $v_z = 200$ m/s at closely spaced points (0.5Å between neighboring points) along the long diagonal are shown in Fig. 3.12. Above z_c, these force-distance characteristics can be used to reconstruct non-contact scans measurable under all possible operation modes. For instance points on a plane parallel to the xy plane lie on a constant force scanline whereas points on a plane parallel to the xz plane lie on a constant height scanline. The same procedure can be used to reconstruct scans at constant normalized frequency shift in order to take advantage of the dense set of equidistant data points recorded in simulated approaches. As an example we show a scanline for $kA\Delta f/f_0$=-0.15nN and A=20 Å plotted together with the constant force scanline obtained for F_z=-2.0nN in Fig. 3.13 with parameters chosen so that both curves match for $z \simeq 3.4$ Å . We can see that the constant frequency shift scan remains close to the constant force curve. The contrast of the former is slightly reduced due to the non-uniform weight multiplying F_z in the rhs of Eq.(3.5). The apparent height difference between the corner hole and the adatom sites is approximately 1.7Å , i.e. larger than in most measurements at constant Δf except one[10]. This is likely due to our neglect of interactions other than covalent bonding. The contrast we obtain is the maximum possible one for a given normalized frequency shift or force. The inclusion of Van der Waals and long range electrostatic interactions reduces the contrast as discussed

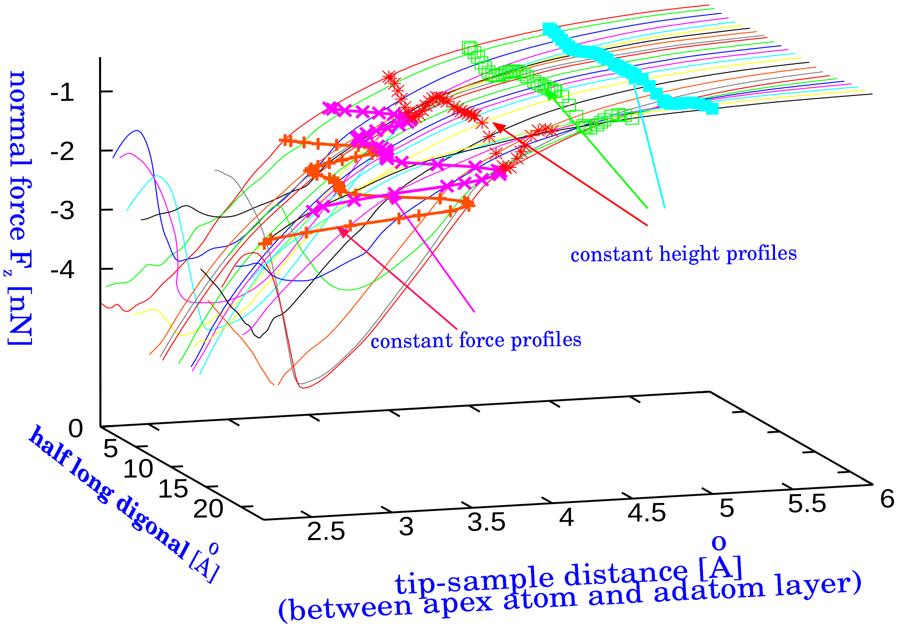

Figure 3.12: Series of quasistatic approach curves with interpolated lateral scans.

later in this chapter.

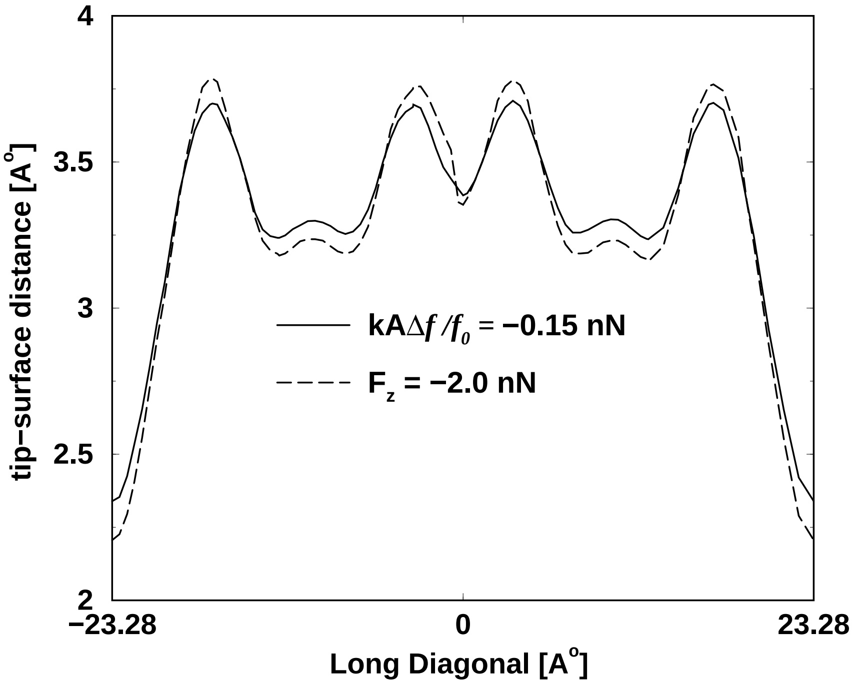

Figure 3.13: Comparison of topographical scans at constant force (dashed curve) and constant normalized frequency shift (full curve). Both curves were computed by interpolation from quasistatic force-distance characteristics.

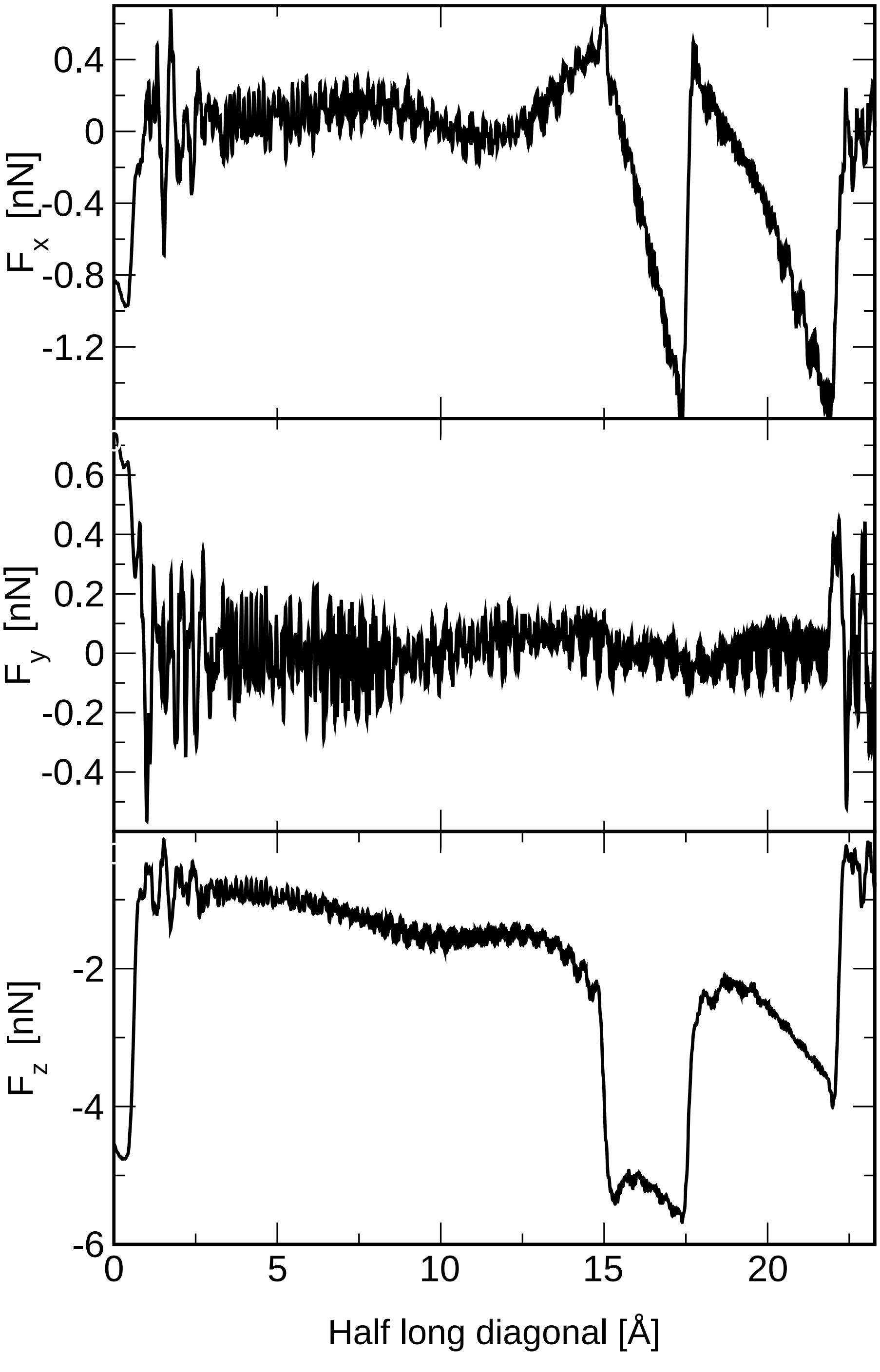

Figure 3.14: Variation of the force components on the tip recorded at a lateral velocity 2 Å /ps at a height z = 3.5Å along the long diagonal of the Si(111)-7×7 unit cell

3.4.5 Constant height scans over the perfect sample and over point defects

Below the highest $z_c \simeq 3.6$Å, constant height scans recorded at constant velocity exhibit friction and wear, adatoms being successively picked up and sometimes

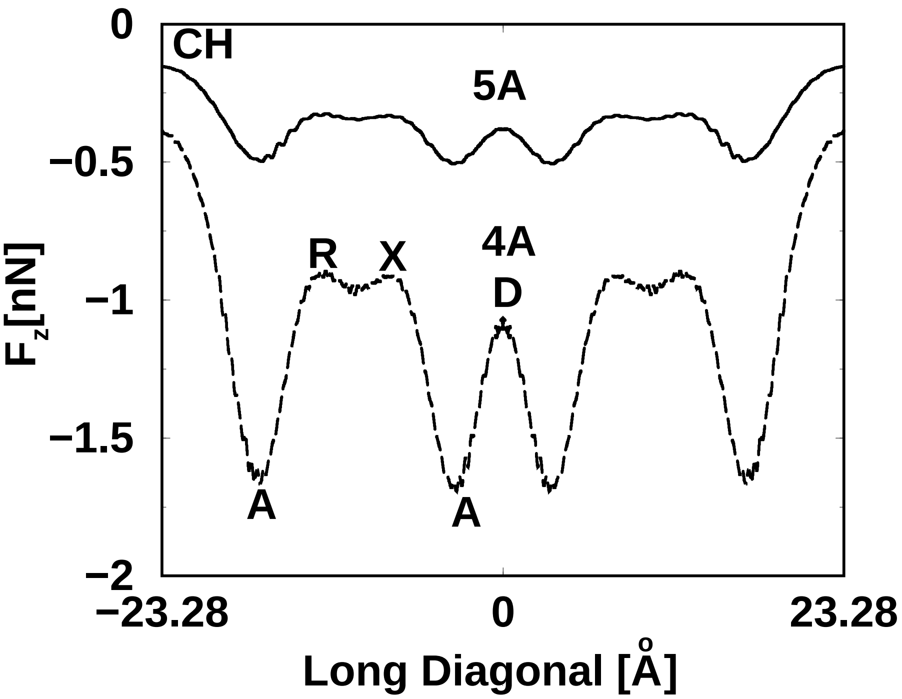

Figure 3.15: Variation of the normal force on the tip along the long diagonal of the Si(111)-7 ×7 unit cell recorded at 2 Å /ps at constant heights z = 5 and 4 Å. CH, A, R, X and D denote corner hole, adatom, rest atom, hollow and dimer-center sites, respectively.

redeposited by the moving tip. The force components recorded at constant z=3.5Å are shown in Fig. 3.14 as an example. The scan starts above the center of a dimer site and extends towards the nearest corner hole along the long diagonal. We first see a strong normal force on the tip, then the tip-sample interaction suddenly gets weaker after the central adatom jumps towards a facet of the tip. This leads to a large lateral force along the scan direction. The corner adatom jumps to the tip afterwards. Above the maximum critical z_c constant height scans are reversible and, as shown in Fig. 3.15, exhibit a contrast with site-specific features in F_z which becomes more pronounced at smaller z. Maximum attraction above adatoms being expected[13, 5], such scanlines appear inverted with respect to the constant force or frequency shift scanlines shown in Fig. 3.13. Note that F_z is the same above the rest atom (R) and above the hollow site (X) in the adjacent triangle between adatoms, although a recessed dangling bond exists only at the R-site. This implies that attraction to the adatoms dominates the picture. Furthermore, both cell halves and all adatoms appear equivalent. Both discrepancies are consequences of because our model takes no account of charge transfer effects[13].

We also recorded constant height scans (i) above a sample including an extra atom near a corner adatom and (ii) above a sample with missing central adatom. Two such scans are plotted in Fig. 3.16 together with the scan above the perfect

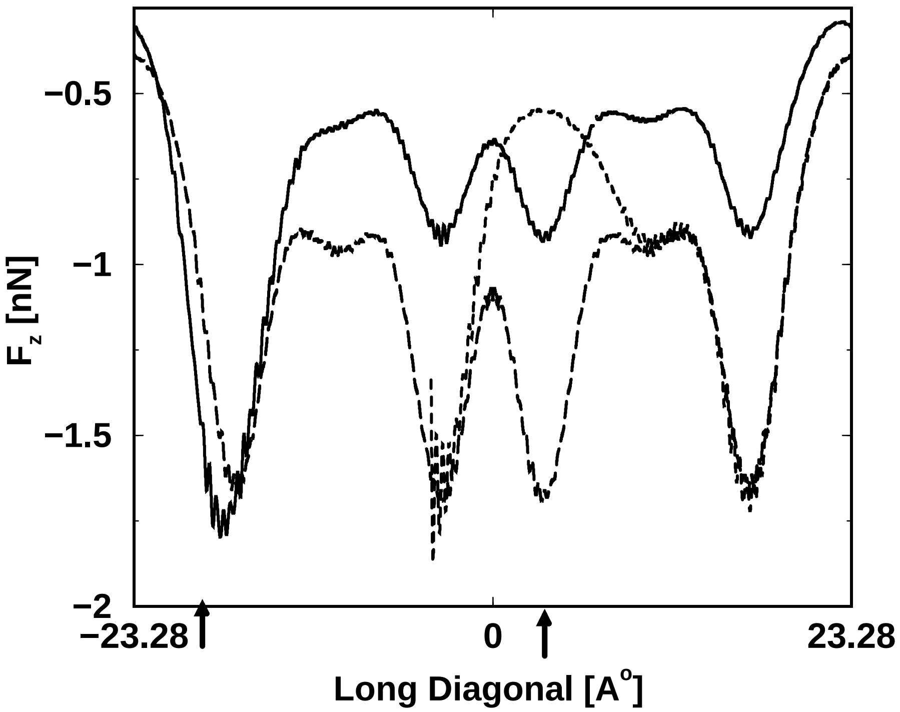

Figure 3.16: Constant height scans in the presence of a missing center adatom (dot-dashed curve, z=4Å), an additional adatoms bound to a corner adatom (full curve, z=4.5Å) compared a similar scan above the perfect surface (dashed curve, z=4 Å). The position of the missing (additional) adatom is indicated by the right (left) arrow on the horizontal axis. The oscillations appearing at the minima above adatom are induced by the scan onset or by thermal fluctuations of the sample.

surface already shown in Fig. 3.15. Compared to the native adatom sites, we observe an almost twice as strong attraction above the dimer formed between the additional adatom and the nearby corner adatom, although it is not possible to resolve the two partners. On the other hand, the missing adatom produces a maximum almost as high and slightly broader than the corner hole. This appearance is consistent with that of deep minima associated with a missing adatom in constant Δf images[8]. These results show that, although characteristic point defects can be recognized on the surface, their identification is not trivial.

3.4.6 Relevance of the macroscopic tip shape

The shape of the tip is of preeminent importance in any scanning probe microscopy. If the tip averages the detected interaction over a certain area due to a blunt end or a large opening angle, the maximum resolution which can be achieved is strongly affected by the tip geometry. Furthermore, the shape of the tip might change owing to a too close approach to the sample due to reversible elastic or to irreversible plastic deformation.

To represent a more realistic tip, we consider the cluster tip used so far as a nano-tip of height h at the end of a macroscopic tip, and model the latter as a truncated cone with a spherical end cap as shown in Fig.3.17. The interaction between the nanotip and the surface is treated atomistically because the chemical interaction between the atoms of the nanotip and surface is largely responsible for the image contrast, while the further parts of the tip and the surface can be treated as continuous media. The macroscopic Van der Waals(VdW) tip-sample interaction treated in the Hamaker approximation [23] for this tip model first calculated in Ref. [107] can be further simplified as follows [108],

$$V_{VdW} = -\frac{H}{6}\left(\frac{R}{(z+h)^2} - \frac{1}{z+h} + \frac{1+tan^2\theta}{z+h+Rsin\theta}\right), \qquad (3.13)$$

H being the Hamaker constant, R the radius of the spherical cap and θ the half opening angle of the cone. In the range relevant for atomic resolution the distance z+h is about several angstroms whereas the typical tip radius is 5 to 100nm, which implies that the first term in Eq. 3.13 is dominant. We have chosen $H = 0.4$aJ [109], but the exact value is not important because only the product HR matters in the range in question.

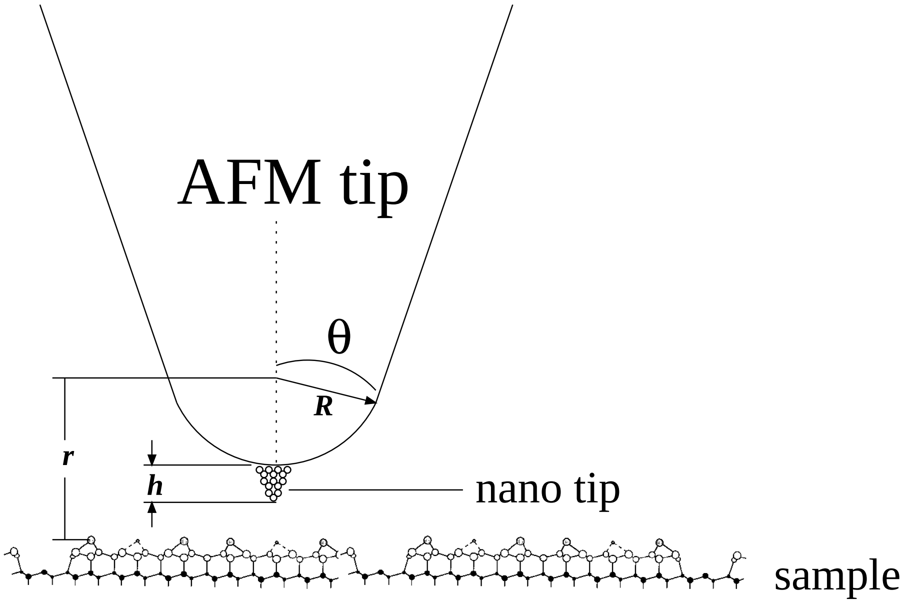

Figure 3.17: Model of a tip consisting of a macroscopically treated truncated cone with a spherical cap and of an atomistically treated cluster

As a whole, the relative contribution of the long-range macroscopic interaction depends on two parameters, the tip radius R and offset h. The tip radius can be obtained by fitting experimental approach data to the first term in Eq. 3.13 in the distance regime where only long-range macroscopic interaction significantly contributes[108]. The offset h is chosen to be 2-4Å.

In the Hamaker approximation, the VdW interaction has no influence on the contrast in the constant height scan mode, but it reduces the contrast in constant

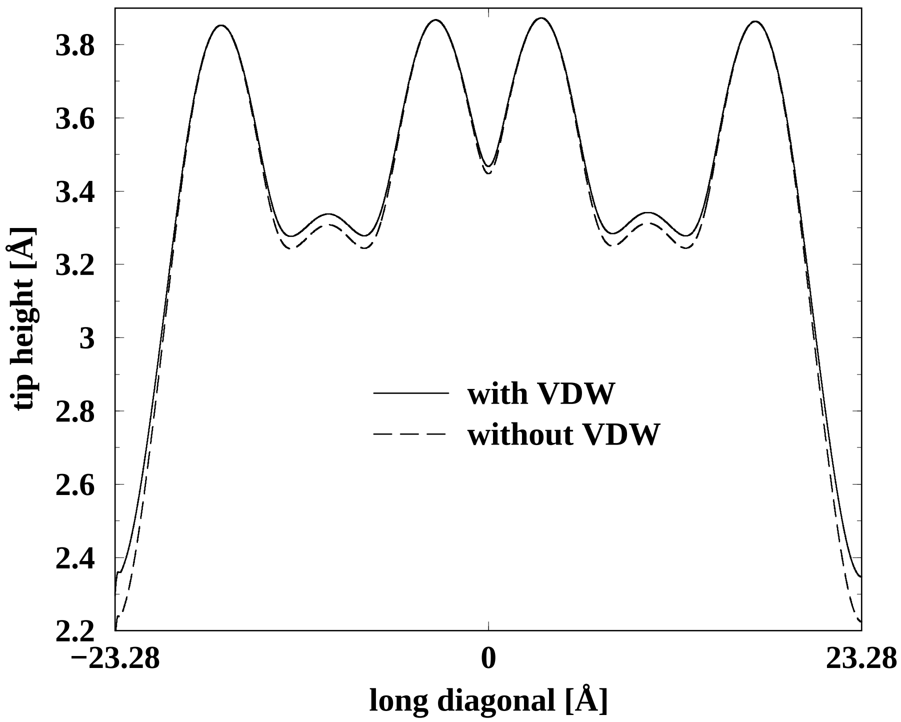

Figure 3.18: Constant force scanlines matched above adatoms showing contrast reduction by the Van der Waals interaction with a macroscopic tip($R = 100$Å, $h = 4$Å).

force or frequency shift modes, because the relative contribution of the VdW interaction varies as the tip height changes and so does the relative strength of the more rapidly varying short-range interaction. In order to demonstrate this effect we have performed calculations with and without the van der Waals interaction for different total force setpoints as described below, in section 3.4.8. If scanlines are matched so that they have the same height above adatoms, they remain close to each other. As an example in Fig. 3.18 we show two such scanlines obtained at $T = 0$ for F_z=-2nN (without VdW interaction) and F_z=-2.59nN(with VdW interaction). The tip position above the corner hole is nevertheless higher when the VdW interaction is included. This example shows that in order to obtain the same scanline corrugation with a blunt macroscopic tip one should select a larger negative setpoint and operate closer to the surface than with a sharp tip. In other words, *sharp tips are better both in terms of sensitivity and stability for noncontact operation.* One effect not taken into account in our treatment is that for small offset h, the unreactive part of the tip can come so close to the surrounding adatoms if the tip is above a corner hole that the Hamaker approximation breaks down, and/or the presumably inert macroscopic tip is repelled.

3.4.7 Feedback algorithm

Although scanlines can be reconstructed for a constant value of any property which depends on the tip-sample interaction from many densely spaced approach curves, this is computationally demanding. To facilitate comparison with nc-AFM experiments, constant force or constant frequency shift scans should be simulated directly. As in experiments the idea behind is to incorporate a feedback in our simulations. The perpendicular coordinate z of the tip is updated at each time step according to the desired force or frequency shift value by means of a feedback algorithm in response to the force computed from the instantenous atomic positions. For example at a given position the simplest algorithm adjusts z on the attractive branch with slope $F^{'} > 0$ according to

$$\Delta z_i = \sigma\alpha(F_i - F_0)/F_0 \tag{3.14}$$

and $z_{i+1} = z_i + \Delta z_i$ where F_i is the total force exerted on the tip atoms at iteration step i, F_0 is the desired force value for a given scan, z_i and z_{i-1} are the current and preceding tip heights, α is a relaxation parameter and $\sigma = 2.1$ Å the distance scale of the SW potential(section 1.2.2).

In a particular simulation, the system is first brought to equilibrium with the tip initially placed above a given site at a height approximate corresponding to the desired value of F_z or Δf guessed from previous simulations, then the scan proceeds at constant velocity while the tip height is automatically adjusted according to the above feedback algorithm at each time step Δt. In the relevant non-contact range, $F_i - F_0 \sim F^{'}(z_i - z_0)$, whereby $F^{'}/F_0 \sim -1/\lambda$ above an adatom, λ being the decay length of the short ranbge interaction. Eq.(3.14) can then be approximately considered as the discretized version of the differential equation

$$\frac{dz}{dt} = \frac{z_0 - z}{\tau} \tag{3.15}$$

which describes exponential relaxation towards z_0 with a time constant $\tau = (|F_0|/\gamma F^{'})\Delta t/\alpha \sim 0.38\Delta t/\alpha$ above an adatoms. With $\Delta t = 4fs$ and $\alpha = 0.1$ τ is still shorter than the period of the heighest frequency vibration in our sample even at the corner hole site above which the interaction exhibits the slowest decay. Such a feedback responds so fast that it picks up sample vibrations and defects atop jumps if they occur, as discussed at the end of the following section. Thermal noise is, of course, suppressed in $0K$ simulations.

3.4.8 Constant force and frequency shift scans over the perfect sample

Constant force scans are easier to compute, but difficult to realize in experiments while avoiding "jump-to-contact" [110] of the cantilever. Almost all experimental images exhibiting atomic resolution are taken at constant frequency shift Δf using frequency demodulation detection [4], but it is tedious to simulate them. Fortunately, as described in section 3.1, there is an approximate relation between the geometrical mean of interaction energy and force $\sqrt{UF_z}$ and the reduced frequency shift γ[101, 102, 100]. We can directly simulate approximate frequency shift scans by taking advantage of this relation.

3.4.8.1 Constant force scans

In order to study the influence of the force setpoint on atomic-scale contrast we performed constant force scans at -1.5, -1, -0.65 nN along the long diagonal of the 7×7 unit cell with a lateral scan velocity of 100 m/s which is much smaller than the velocity of sound but it much faster than typical experimental scan speeds. However, what matters is that a tip displacement by 1Å takes 1ps which allows the tip motion to proceed slowly with respect to most of the vibrations within the sample . As a result, the recorded scanlines does not depend on the scan direction as long as no atoms jump. If tip moves faster, the results become direction and velocity dependent, and hence unreliable. The z-position of the tip was adjusted with the first-order feedback described in section 3.4.7. As in experiments, the position of the tip then provides an approximate map of the surface. From Fig. 3.19 we see that the adatoms appear higher than the corner holes, i.e. the scanlines reflect the surface topography and appear inverted respect to constant height scans in Fig. 3.15. Furthermore the contrast increases as the strength of the setpoint force is increased. However, once this strength exceeds a critical value, which is still below that corresponding to maximum attraction in the force vs. distance approach curve above an adatom (see Fig. 311) irreversible adatom jumps occur. This critical strength is close

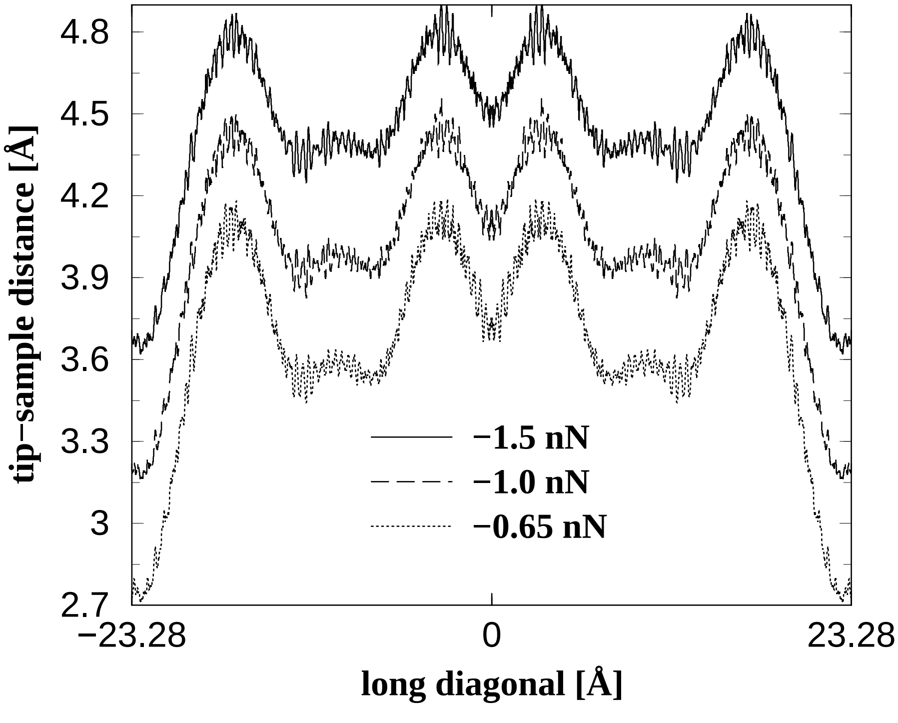

Figure 3.19: Constant force scans with short-range force alone. The noise is due to thermal fluctuations at 100K

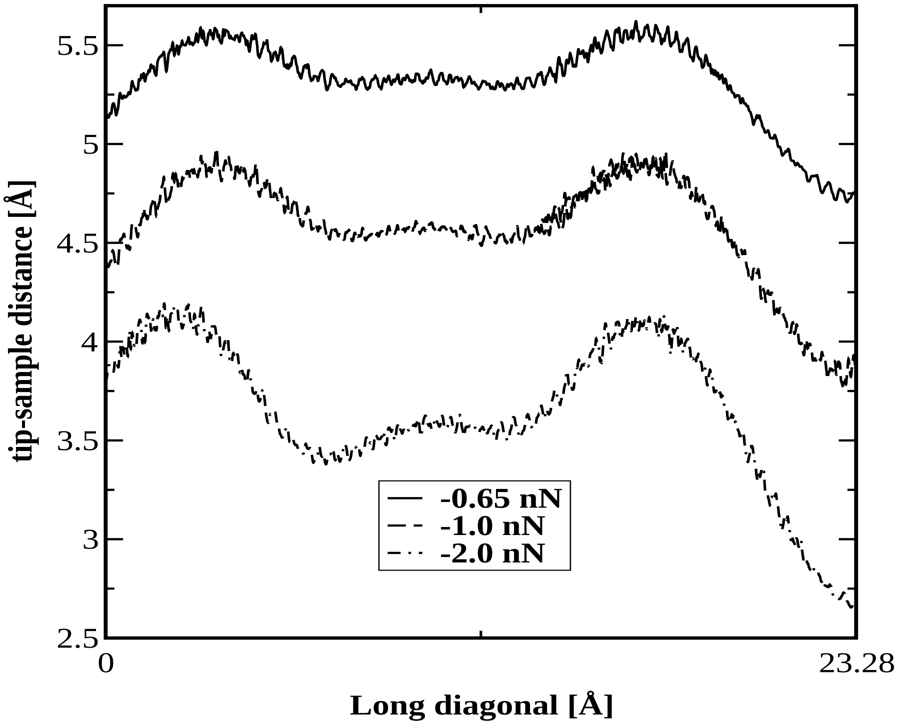

Figure 3.20: Constant force scans with short-range chemical force and long-range macroscopic van der Waals force included(R = 100Å, h = 4Å). Only half of the diagonal is shown.

to -2nN without VdW interaction.

As a next step, we included the long-range van der Waals interaction with parameters of $R = 100$Å and $h = 4$Å , and repeated constant total force scans for -2.0, -1.0 and -0.65 nN. Results are shown in Fig.3.20; comparing Fig 3.19 and Fig. 3.20 we see that the inclusion of the van der Waals interaction significantly reduces the overall contrast for a given total force, i.e. 1.1Å vs. 0.8Å at -0.65 nN, mainly because the average tip height is higher. Furthermore, there are no adatom jumps at -2nN. The contrast reduction comes about because relative contribution of the the short range interaction which gives rise to the corrugation is larger above adatom sites and smaller above corner hole sites. The contrast strongly depends on the macroscopic shape of the tip, namely the the offset h and radius R, as observed in the constant force scans at -2nN plotted in Figs. 3.21 for R=10 nm and 3.22 for h=4.07Å. We see that the contrast is reduced if we reduce the offset or increase the tip radius. This is probably why the contrast can be quite different between different nc-AFM experiments showing atomic resolution.

Close to the previously mentioned critical force value the stability of scans depends on the temperature because of the thermal vibrations of surface atoms and of activated jumps over energy barriers which are lowered by attraction to the tip. For example no adatom jump is observed at a constant force F_z=–2nN at 0K, while one central adatom jumped towards the tip to a nearby bridge site

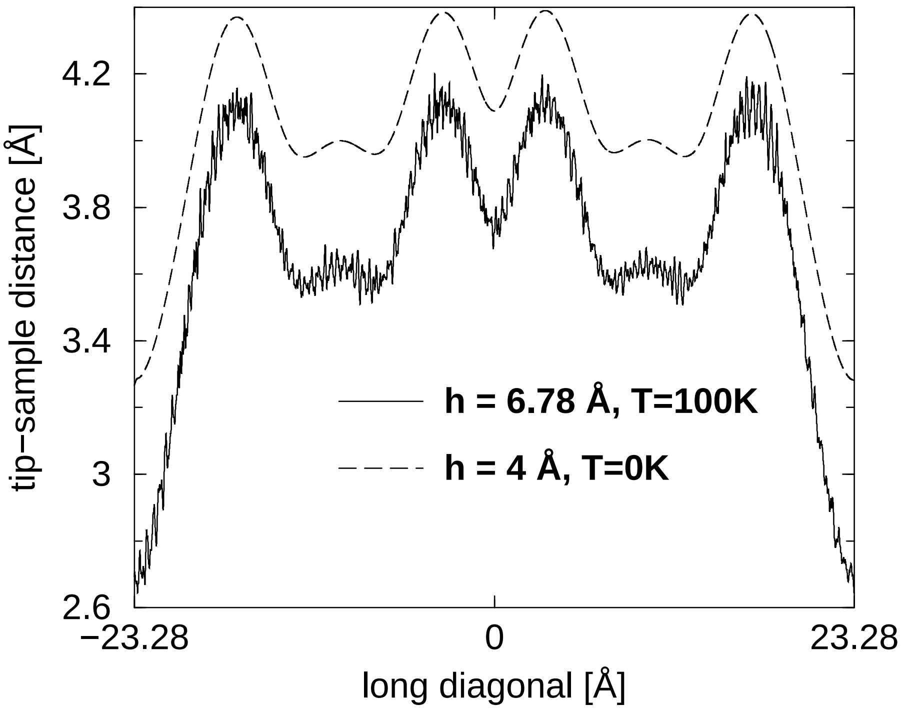

Figure 3.21: Influence of the macroscopic tip offset on the contrast at a constant force of -2nN.

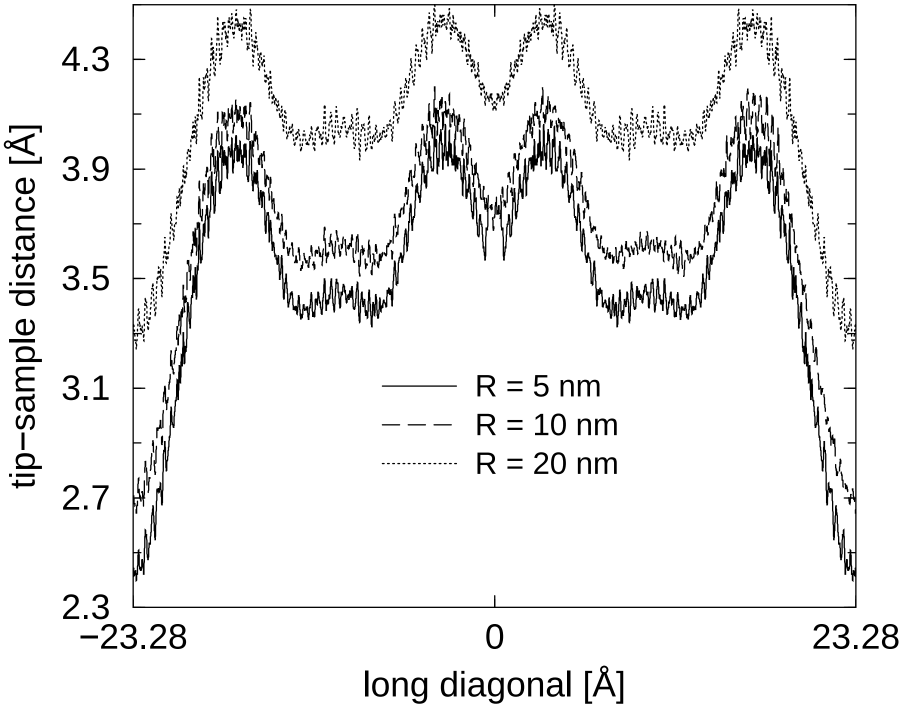

Figure 3.22: Influence of the macroscopic tip radius on the contrast at a constant force of -2nN.

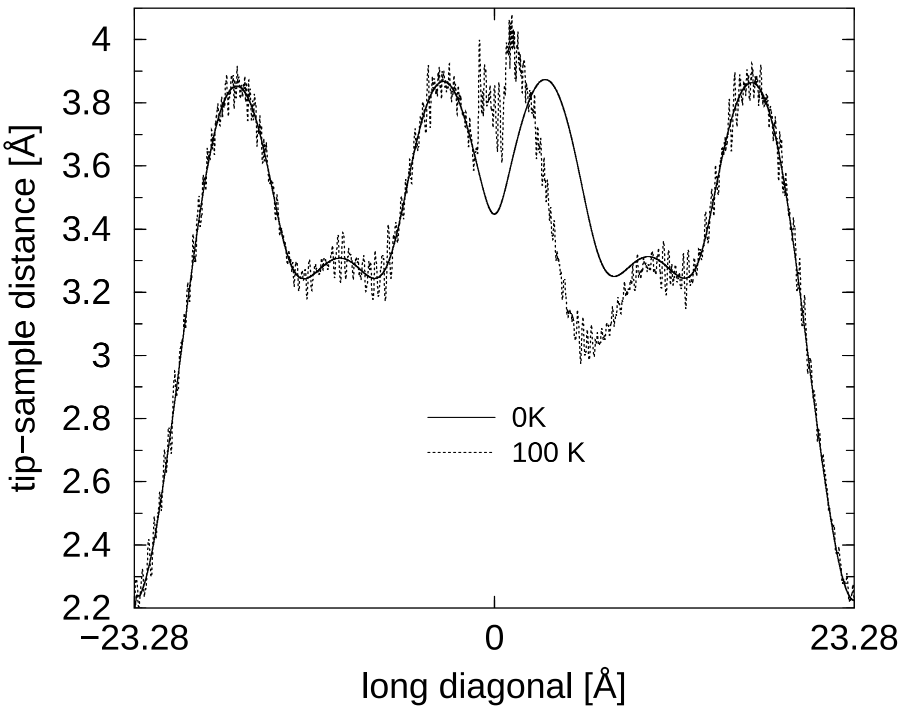

Figure 3.23: Thermal fluctuations and activated lateral adatom jump towards the tip at 100K revealed by comparison with a scan at 0K at a constant force close to the limiting value for stable non-contact operation(without Van der Waals interaction).

at 100K as seen in Fig. 3.23. Then the adjacent center adatom jumps towards the former and forms a dimer parallel to the scan direction. The feedback responds by raising the tip in order to reduce the resulting enhanced attraction to the setpoint value. Such jumps of the tip height are similar to those observed in experiments and simulations of lateral adatom manipulation on different systems by on STM tip[111]. They suggest that lateral manipulation of Si adatoms by on AFM tip may be possible. This is discussed further in section 3.8. Away from the displaced adatoms both scans in Fig. 3.23 coincide apart from thermal fluctuation, thus proving that thermal expansion is negligible at 100K. The tip-induced relaxation of the sample can be quantified by comparing constant force scana above a free and a frozen prerelaxed sample. At F_z=-2nN the surface adatoms are observed to relax 0.15 Å towards the vacuum (Fig. 3.24).

3.4.8.2 Constant frequency shift scans

Although there is a well-defined relation between force and Δf in the small perturbation limit [15], it is tedious to compute constant Δf scans directly. Fortunately, as pointed out in section 3.1.1, the reduced frequency shift $\gamma = \frac{\Delta f}{f_0} k A^{3/2}$ proportional to $\sqrt{U F_z}$ in a wide range of tip-sample distance d if the distance dependence of the interaction is specified by a single parameter where U is the tip-sample interaction energy and $F_z = \partial U / \partial z$ is the corresponding

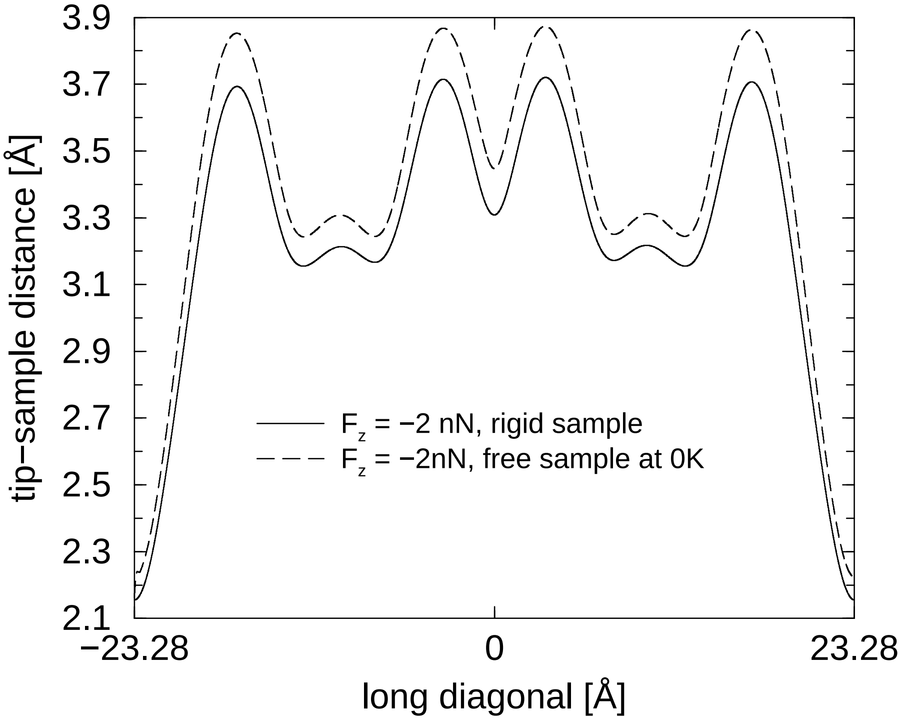

Figure 3.24: Tip-induced deformation revealed by comparison between constant force scans above a deformable vs. a rigid (prerelaxed) sample(without Van der Waals interaction).

force. In particular[100]

$$\sqrt{UF_z}/\gamma = \sqrt{2\pi} = 2.51 \tag{3.16}$$

if both U and F_z have the same z-dependence, e.g. exponential. In our case this is approximately valid for the short-range attraction, but according to Eq.(3.8) the same ratio for the van der Waals interaction between a sphere and a plane is $2\sqrt{2} = 2.83$. To check the usefulness of the relation Eq. (3.16), we first have reconstructed scanlines at constant F_z, Δf, U and $\sqrt{UF_z}$ taking only the short-range interaction into account. From Fig. 3.25(a) we see that the difference between the constant $\sqrt{UF_z}$ and constant Δf scanlines is tiny and that the corrugation of the constant Δf profile is smaller that the corrugation of the constant F_z profile and larger than the corrugation of the constant U profile, as expected. However, we found that the fitted scaling factor $\sqrt{UF_z}/\gamma$ $\approx$2.67, i.e. slightly higher than the exact value 2.51 for a number of reasons, e.g. underestimate of γ via numerical integration of Eq. 3.4, finite A/d, deviation from a pure exponential dependence of $U(d)$ arising from the superposition of contributions with different z-decay rates (repulsive and attractive, or from inequivalent atom pairs). We then have reconstructed scanlines at constant F_z, Δf, U and $\sqrt{UF_z}$ in order to determine the optimum value of $\sqrt{UF_z}/\gamma$ when the tip-sample interaction includes both short- and long-range contributions. This ratio is significantly higher, i.e 3.27, if we match all profiles at rest atom

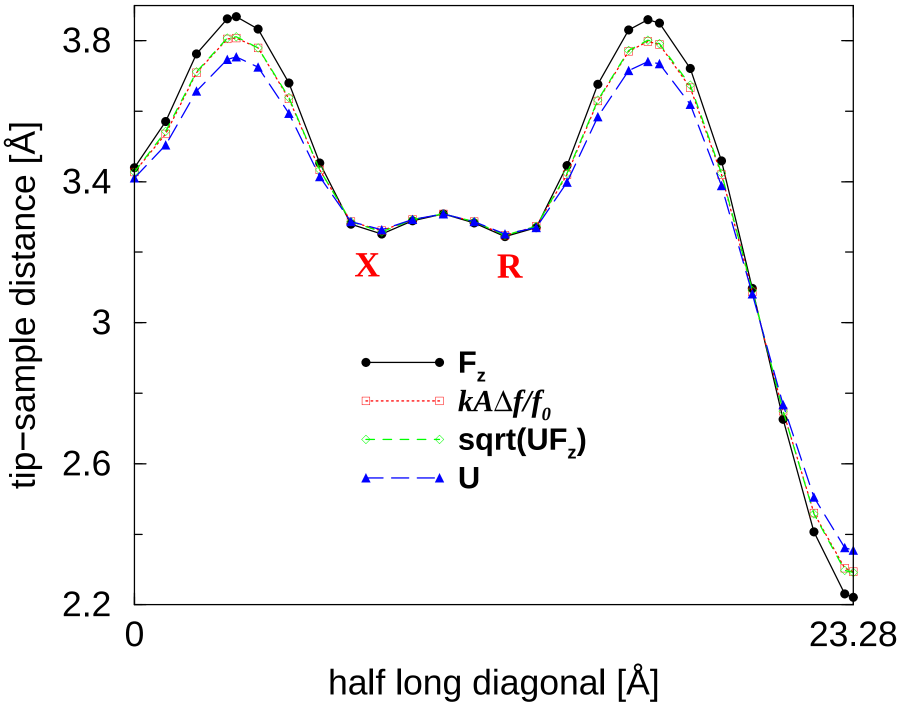

(a) Scanlines with short-range interaction alone.

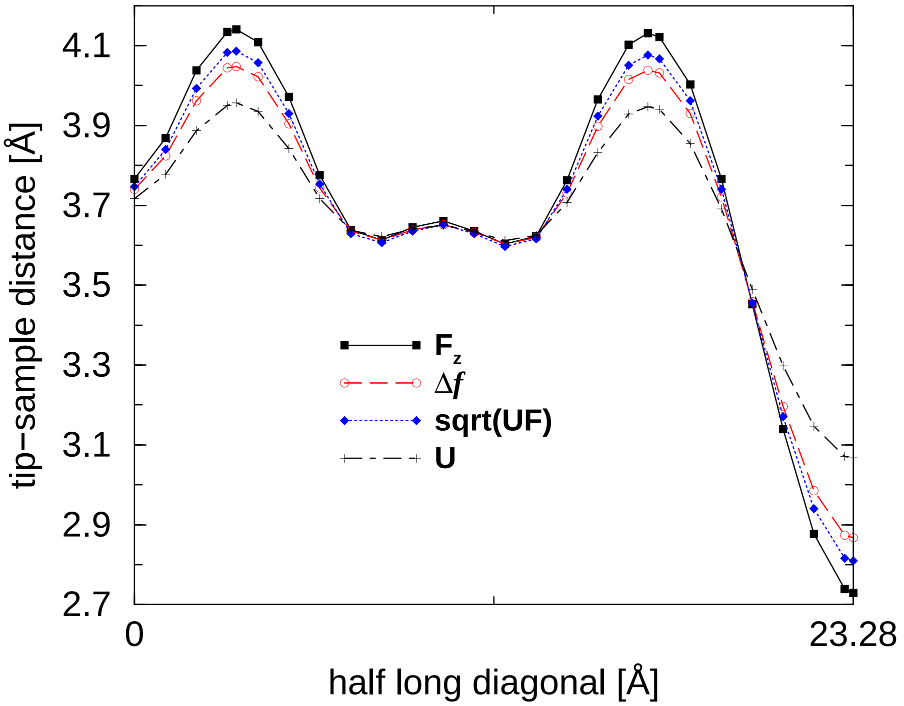

(b) Scanlines with VdW interaction (h=4.07Å, R=10nm).

Figure 3.25: Interpolated scanlines at constant values of several related quantities constructed from quasistatic approach curves. The values are chosen so that all profiles match at the rest atom (R) site.

(R) sites; the corrected value is 3.1 if we take the above 6% error into account. As discussed below, this value of γ compares well with values estimated from experiments [2]. Furthermore, the corrugation of the constant $\sqrt{UF_z}$ scanline is now slightly larger than the corrugation of the Δf scanline, as seen in Fig. 3.25(b).

We now explain why the appropriate value of $\sqrt{UF_z}/\gamma$ can exceed the limiting values derived for pure exponential or inverse power laws. Define, $c_{tot} = \frac{\sqrt{U_{tot}F_{tot}}}{\gamma_{tot}}$, $c_{chem} = \frac{\sqrt{U_{chem}F_{chem}}}{\gamma_{chem}}$ and $c_{VdW} = \frac{\sqrt{U_{VdW}F_{VdW}}}{\gamma_{VdW}}$. According to the first-order perturbation expression Eq. 3.4, γ is a linear functional of F_z, i.e. $\gamma_{tot} = \gamma_{chem} + \gamma_{VdW}$ if $F_{tot} = F_{chem} + F_{VdW}$ to a good approximation. However, $\sqrt{UF_z}$ is not proportional to F unless U/F is constant. More precisely, because each U and the corresponding F_z are both negative in the attractive range relevant for non-contact AFM,

$$\begin{aligned} 1 &< \frac{\sqrt{U_{tot}F_{tot}}}{\sqrt{U_{chem}F_{chem}} + \sqrt{U_{VdW}F_{VdW}}} \qquad (3.17) \\ &= \frac{c_{tot}\gamma_{tot}}{c_{chem}\gamma_{chem} + c_{VdW}\gamma_{VdW}} = \frac{c_{tot}}{c_{chem} + (c_{VdW} - c_{chem})\gamma_{VdW}/\gamma_{tot}}, \end{aligned}$$

so that $c_{tot} > c_{chem}$ because $c_{VdW} > c_{chem}$; c_{tot} can also exceed c_{VdW}. For

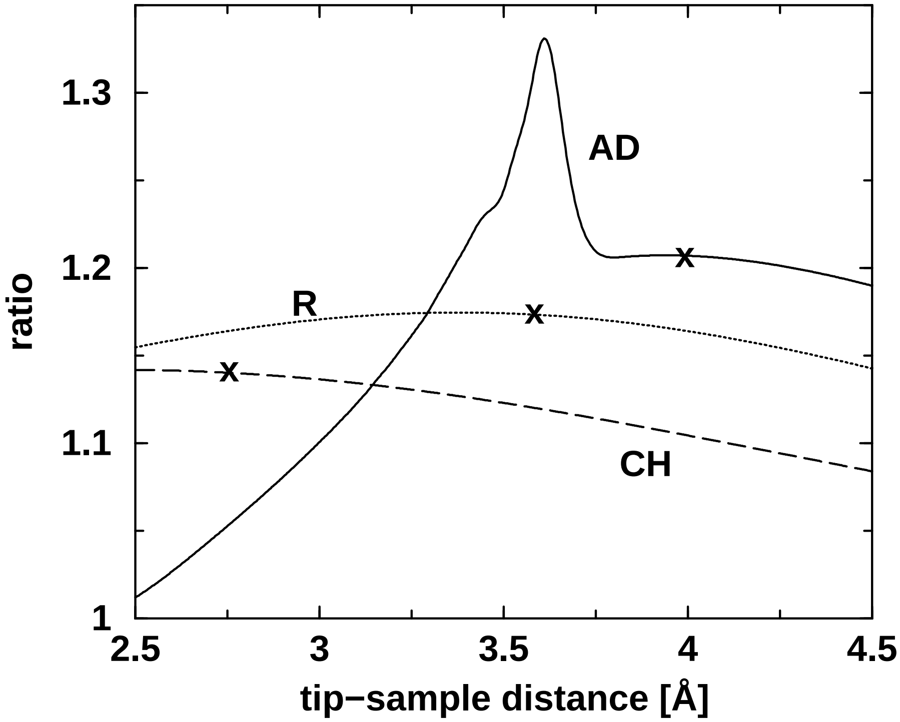

Figure 3.26: Variation of the left hand side of Eq. 3.18 with respect to the minimum tip-sample separation d at different sites (AD: adatom, D: dimer center, CH: corner hole). Minimum tip-sample distances at each site are highlighted with crosses corresponding to the constant $\sqrt{UF}$ scan in Fig. 3.25(b).

typical parameters this is in fact true, as demonstrated in detail by computations for a frozem sample, $R = 10\text{nm}$, $h = 4.07\text{Å}$ and values of d for which to the short-range force is attractive. As seen in Fig. 3.26, the left hand side of Eq. 3.18 varies slowly above the onset of the SW contribution and is somewhat larger above the adatom than above the corner hole.

In Fig. 3.25(b) the ratio $\frac{\sqrt{U_{tot}F_{tot}}}{\gamma_{tot}}$ is 3.2 above the adatom and 2.8 above corner hole sites. This value for the corner hole indicates that the dominant contribution to the frequency shift comes from the long-range VdW interaction. This is obviously different from the situation in Fig. 3.25(a).

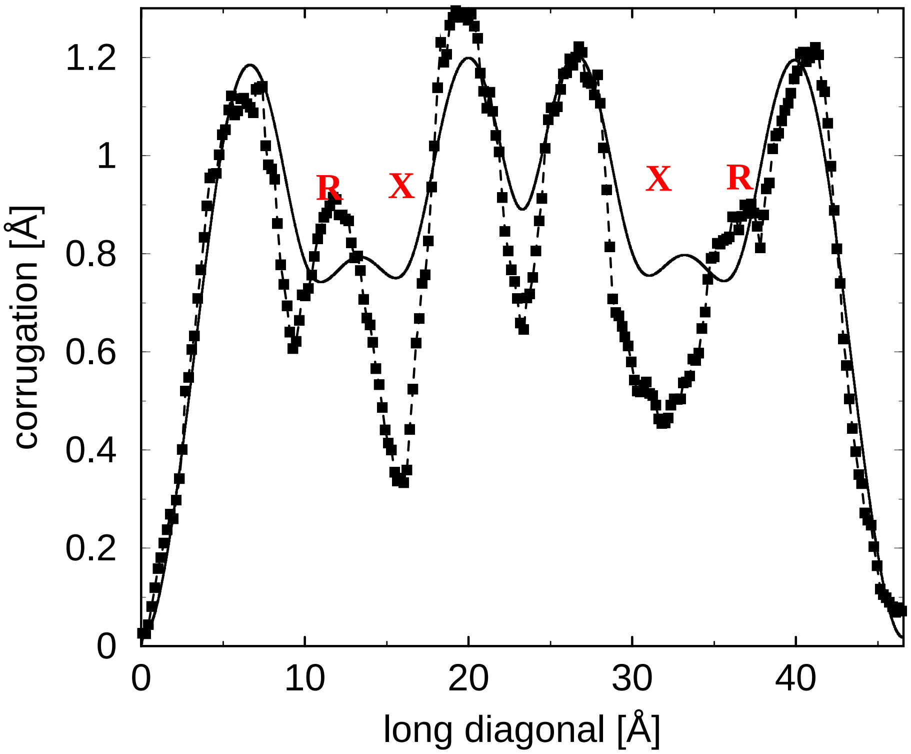

Figure 3.27: Comparison between computed scanline(solid curve, see text) and a line section along the long diagonal of the unit cell in Fig. 3.2b

Because the difference between corresponding constant $\sqrt{UF_z}$ and constant Δf scanlines is small, we take advantage of the approximate relation between γ and $\sqrt{UF_z}$ to directly compute constant $\sqrt{UF_z}$ scanlines and compare them to experimental constant Δf profiles. To model the atomic scale contrast presented in Fig. 3.2b, we calculated a series of scanlines varying the parameters R and h and using a feedback setpoint determined by the experimental value of $\gamma = -2.82 \times 10^{-15} Nm^{1/2}$ and the corrected relation $\sqrt{UF_z}/\gamma = 3.1$. The calculated scanlines compared to a line section taken along the long diagonal of the unit cell of Fig. 3.2b. We obtained the best agreement assuming a tip radius $R = 9\,\text{nm}$ and a tip–apex offset h=4.1Å (corresponding to four Si(001) layers). As seen in Fig. 3.27, the apparent width of the adatoms as well as the overall corrugation height are in good agreement. The experimental tip-sample distance is only known up to a few Å, but the computed tip height at the corner hole is 3Å, while the total force varies between -2.1 nN and -2.3 nN. On the basis of the simulations described previously, we conclude that the normal contrast data in Fig. 3.26 were indeed obtained in the non-contact range and that our interaction model provides a reasonable description of such data. However, variations in the measured heights of inequivalent adatoms [14] and, especially, in the minima between the adadtoms are not adequately reproduced in the simulations. These differences likely result from variations in the distribution of electronic charge among surface atoms [13]. Such effects are not properly taken into account in our interaction potential. We have also modeled the data presented in Fig. 3.4a and found best agreement assuming R=20nm, and h=4.1 Å(not shown), the larger tip radius being expected following a tip crash.

3.4.8.3 Identification of surface defects in constant force and frequency shift scans

As discussed section 3.4.5, we were able to recognize typical surface defects on the Si(111)–7×7 reconstructed surface in constant height scans (Fig. 3.16). In order to interpret the experimental images in Fig. 3.5 we also performed constant force and constant frequency shift scans above a sample with an extra adatom next to the corner adatom and another sample with a missing central adatom. Results are shown in Fig. 3.28 only for scanlines at constant force since the corresponding scanlines at constant frequency shift are not significantly different. As we can see from Fig. 3.28(a) the tip retracts considerable above the dimer formed by the extra atom to keep the tip-sample interaction force constant. There is only one maximum corresponding to the extra adatom and its partner; this is consistent with the constant height scanlines in Fig. 3.16. This maximum might correspond to the brighter "adatom" in the experimental image in Fig. 3.5(c). In Fig. 3.28(b), the tip dives into the surface above the missing adatom site and the resulting minimum is deeper than any site on the surface except the corner hole. The width of the minimum around the missing adatom is even broader than the corner hole. This likely corresponds to the dark spot close to an expected adatom position in the experimental images of Fig. 3.5(b) and Fig. 3.6(a)(buttom left corner).

3.5 Contrast Inversion

To test our hypothesis regarding the inverted contrast observed in Fig. 3.3 and Fig. 3.4(b), we have performed simulations using our non–reactive tip model. In constant $\sqrt{UF_z}$ scans the feedback was stable at the value of the setpoint determined from the experimental value $\gamma = -5.36 \times 10^{-5} Nm^{1/2}$ (assuming $\sqrt{UF_z}/\gamma$) only for large enough values of R. The best agreement was found for $R = 20\,\mathrm{nm}$, $h = 2.7\,\text{Å}$ and a repulsive decay length $\lambda_1 = 0.6\text{Å}$ The computed minimum separation between the tip apex and the unperturbed adatom layer is then 3.5Å compared to 4.1Å for the fit in Fig. 3.27, i.e. significantly larger than the Si–Si bond length (2.35Å) in either case. Assuming a larger R or a smaller λ resulted in a reduction of the inverted contrast for the given γ. The smaller

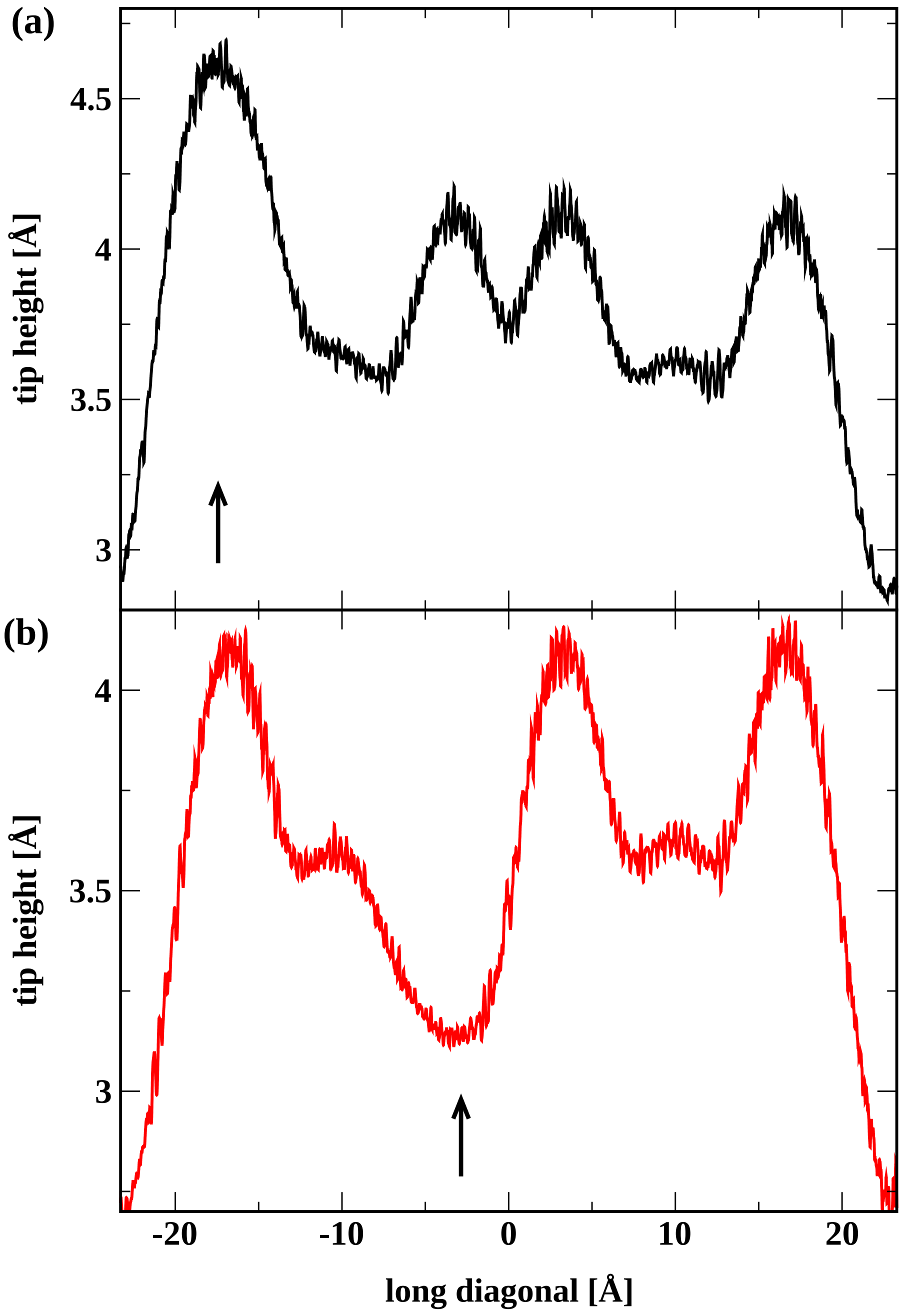

Figure 3.28: Scanlines across surface defects in constant force mode at $F_z = -2nN$(with Van der Waals interaction, R=100Å, h=4.0Å): (a) extra atom next to corner adatom (b) missing central adatom. The lateral positions of the pre-relaxed defects in the absence of the tip are indicated by arrows.

value of h is consistent with the absence of adsorbed silicon atoms on the inert tip. As seen in Fig. 3.29, the overall corrugation and especially the apparent width of the adatoms are in good agreement. This reduced width arise because each adatom is repelled by the tip apex as manifested in the computed force component on the tip which switches from negative to positive with respect to the scan direction as the tip passes over each adatom. The total perpendicular force, which is dominated by the Van der Waals interaction nevertheless becomes more attractive with decreasing distance in the range where stable feedback operation is possible. There are discrepancies between the adatoms, especially above the hollow X sites. As in Fig. 3.27, these discrepancies are probably due to differences in the charge distribution which can still influence the interaction with chemically inert tip.

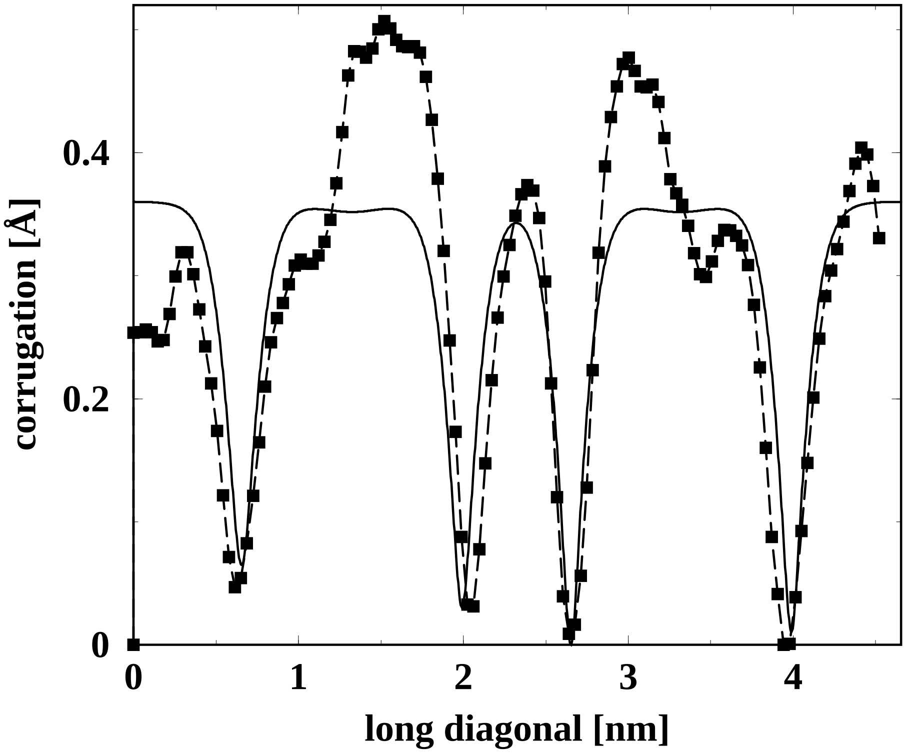

Figure 3.29: Comparison between computed scanline and a line section taken along the long diagonal of the unit cell of the low pass filtered (but not inverted) data shown in Fig. 3.3b

In order to investigate the range of setpoints where inverted contrast could be obtained, we also performed several calculations for different values of $\sqrt{UF_z}$. As the latter was reduced (relative to the experimental setpoint), the corrugation rapidly dropped. In simulations with a slightly larger setpoint, the feedback became unstable, however in other words, inverted contrast can only be obtained in a narrow range of γ. By looking at the error signal we also observed that the feedback is fluctuating more than in our normal contrast simulations. These findings are in agreement with experiments namely that inverted contrast was only observed in a narrow range of frequency shift and that imaging was noisier and more prone to instabilities compared to when normal contrast was obtained [96]. The fitted decay length $\lambda_1 = 0.6$Å is relatively large compared to typical values for Born–Mayer and similar potentials describing repulsion between closed shells, e.g. 0.2 to 0.35Å for light elements. Note, however, that the fitted repulsive interaction implicitly includes the deformation of the tip which is neglected in our simulations. Compression of the tip, especially at the apex, should be reflected in a larger effective value of λ_1.

3.6 Periodic Tip Oscillation and Energy transfer

Dissipation i.e. energy loss is an important issue in friction force microscopy (FFM) where the microscopic origins of dissipation are being studied. Possible origins of dissipation in friction are related to phonon excitation, electronic excitations and irreversible changes at surfaces in contact [112].

In dynamic force microscopy two types of interactions can be involved, namely conservative and dissipative. We have so far considered the first type of interaction, namely without damping. As a matter of fact external power must be supplied to the cantilever to compensate intrinsic as well as interaction-induced losses in order to sustain a stationary oscillation of the tip. When the tip is oscillated in the vicinity of a surface, there are different forms of energy losses in addition to the intrinsic damping of the cantilever. There have been several experimental observations of additional damping, but still considerable controversy about the mechanisms. Lüthi *et al* were the first to present data on atomic-scale variations of damping in a noncontact AFM experiment at constant Δf on a Si(111)-7×7 surface, whereby the strongest dissipation was found above the corner holes [8]. The corrected version of their images reproduced in Fig.3.6 was recently published together with corrected parameters [113]. However, recent experiments showed the highest damping above adatoms [103]. Details about how the additional damping can be measured simultaneously with the frequency shift are given in Refs.[113, 114, 115]. Damping attributed to long- and short-range interactions has been observed [114, 115]. The explanation of long-range electric damping by Joule dissipation is well-established and experimentally confirmed [116, 117]. Short-range damping is less understood and has been found to be more sensitive to tip changes and/or loosely bound atoms than the frequency shift. Recent theoretical calculations provide several explanations for this kind of damping, e.g. changes produced by nonlinear properties of the tip-cantilever system [118, 119], adhesion hysteresis or an effective viscosity [120, 121, 122], which can in principle arise even in the non-contact range and be related to fluctuating forces acting on the tip in close proximity to the sample [123].

In this section we attempt to shed more light on this kind of short-range damping. One important issue is whether dissipation can occur even if the minimum tip-sample separation d exceeds z_c. According to recent estimates [98, 123] this dissipation due to coupling to acoustic phonons is finite but small.

As already mentioned in section 3.4.3 we have observed hysteresis in quasistatic approach and retraction curves below a critical distance z_c. This hysteresis can also give rise to energy transfer from the tip to the sample and then to the heat bath, if the atomic arrangements which lead to the quasistatic hysteresis can still occur if the tip oscillates.

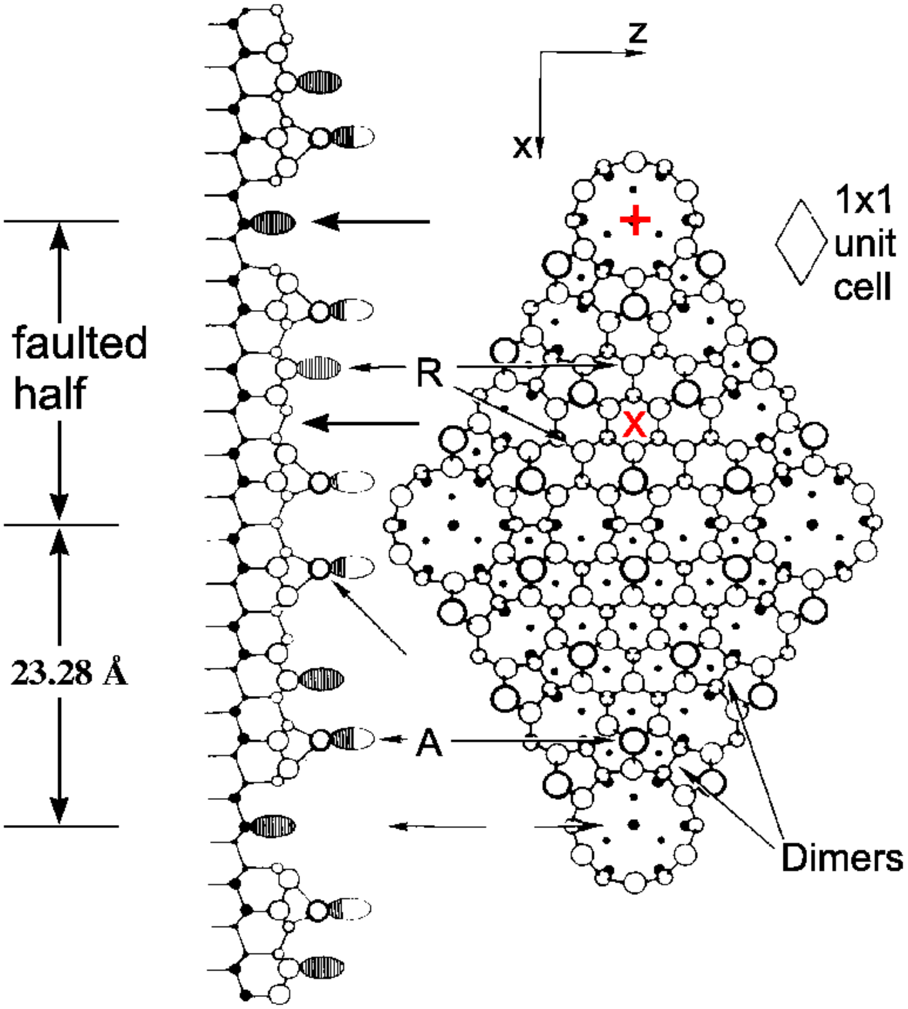

Figure 3.30: DAS model of the Si(111)–7×7 surface and specific sites. CH(+): corner hole, A: adatom with reactive dangling bond, R: rest atom, X: hollow site. The tip was driven sinusoidally above those sites.

In order to understand the mechanism of dissipation we pursued dynamic simulations which were initiated by T. Bonner using a single atom tip [124]. We vibrated our Si cluster tip above the specific surface sites indicated on Fig. 3.30 and compared the work done and the heat transfer above these sites. These dynamic simulations were done with the first interaction potential described in section 3.3 without Van der Waals interaction. As discussed in section 3.4.3, this potential becomes strongly attractive and induces jumps of adatoms towards the tip once the distance between its apex and the nearest adatom becomes slightly smaller than the range of the SW potential.

In real experiments the interaction-induced damping is detectable but small due to the very different time scales of fast surface atom relaxation versus slow tip motion. In our dynamic simulations we use a rather high tip oscillation frequency to amplify this type of damping and to keep computation time within reasonable limits.

As a result, several time scales or frequencies are important in our simulation, namely:

(i) the tip oscillation period T_z or frequency $f_0 = 1/T_z$;

(ii) the interaction time $\tau_{int} = T_z\sqrt{\lambda/A}$, here λ is tip-sample interaction range and A is the oscillation amplitude;

(iii) the maximum longitudinal acoustic phonon frequency f_{max} of silicon, about 12 THz;

(iv) the minimum oscillation frequency f_{min} in the simulated system due to the finite thickness of the slab, previously discussed in section 3.3;

(v) the relaxation time τ_T of the thermostat.

The inverse interaction time has to be larger than f_{min} and smaller than f_{max} in order to allow phonon excitation, namely

$$f_{min} < f_0\sqrt{\frac{A}{\lambda}} < f_{max}.$$

In most of our calculations we choose A=20 Å , whereas $\lambda \sim 1$Å . Thus we require $0.2 f_{min} < f_0 < 0.2 f_{max}$. For a slab with 6 free layers we estimate $f_{min} \sim 1.2 THz$, so the allowed oscillation period must lie between 0.4 to 4ps. We performed most simulations with the oscillation period T_z=2.5ps. We could increase the tip oscillation period if we increased the thickness of the slab, but this would increase computing time by a proportional amount. The relation between the relevant frequencies is shown in Fig. 3.31.

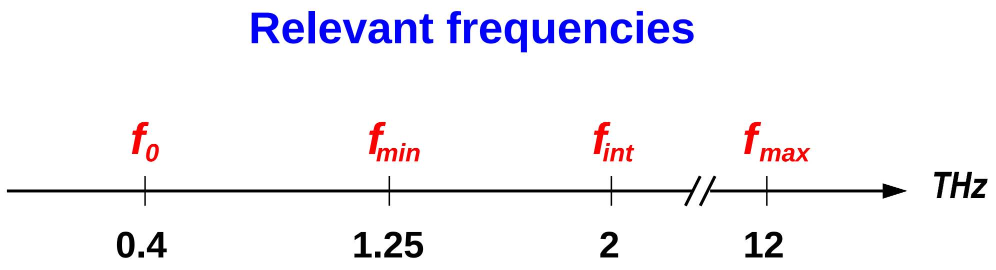

Figure 3.31: Relevant frequencies for dynamic simulations, tip oscillation frequency f_0, inverse interaction time f_{int}, minimum phonon frequency f_{min}, maximum LA phonon frequency f_{max}.

To control the temperature, we used Berendsen thermostat[46] for reasons given in section 1.5.4. If τ_T is short compared to T_z a step in the energy transfer to the heat bath is observed for each close approach of the tip to the sample. Thus a compromise can be found between reasonable simulation time and a weak couplingto the thermostat. Results were approximately independent of τ_T as long as $\tau_T < T_z$ (otherwise the sample heats up) and $\tau_T > \tau_{int}$ (otherwise the temperature pulses leading to steps in the heat transfer merge into irregular fluctuations).

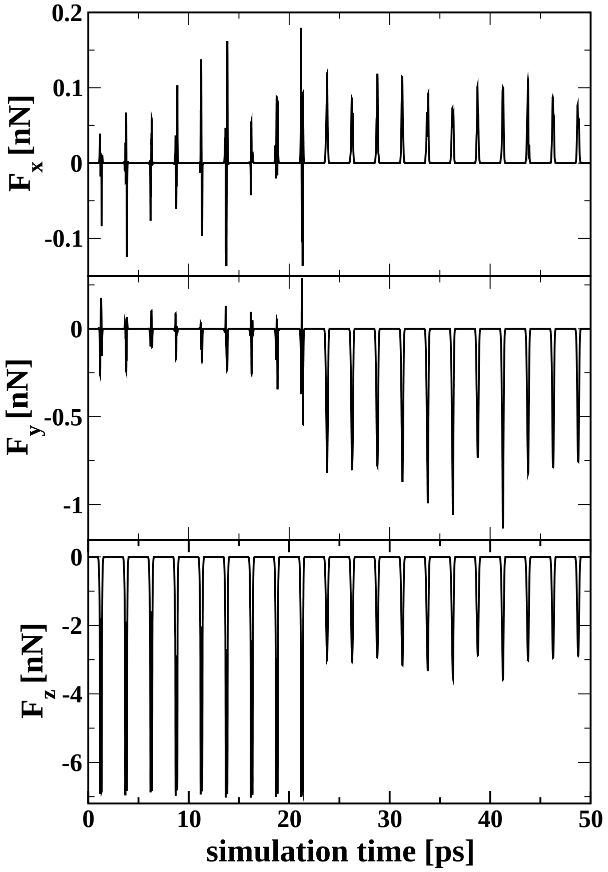

(a) Time-dependent force components.

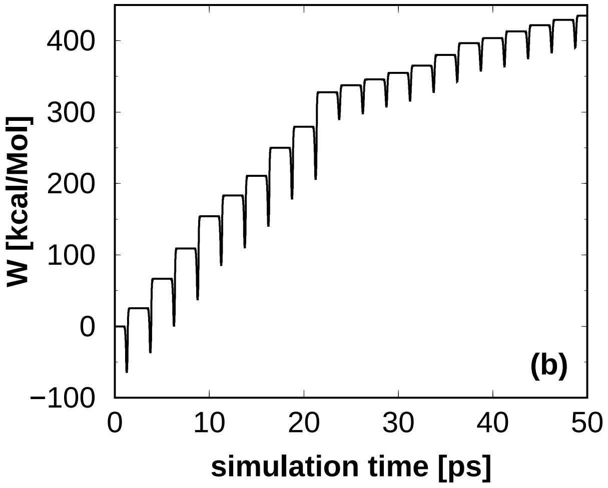

(b) Work done by the tip.

Figure 3.32: Dynamic simulation with a sinusoidally driven tip above an adatom site at 0.4 Thz with an amplitude $A = 20$ Å

As expected, the time-dependent force on the tip consist of a periodic series of narrow pulses of width $T_z\sqrt{\lambda/A}/f$ slightly modulated by thermal fluctuations. Fig. 3.32 illustrates a borderline case where the minimum approach distance is slightly smaller than z_c, so that the center adatom under the tip would be destabilized in a quasistatic scan. In our dynamic simulations a jump to an energetically more favored position on the side of the original site occurs only after the ninth pulse. This can also be seen from the evolution of the force components in Fig. 3.32(a) as well as of the lateral mean-square displacement $\Sigma|r_i^2|$ of all adatoms shown in Fig. 3.33. Under typical experimental conditions the pulse width would be $\approx 1\mu s$ i.e. encompassing more than one million adatom vibrations, a quasistatic situation. Nevertheless, a small amount of energy can be transferred to acoustic phonons, either directly or via anharmonic decay of local vibrations excited by the force pulses. The latter is likely, to open a new energy-loss channel for $d \sim z_c$.

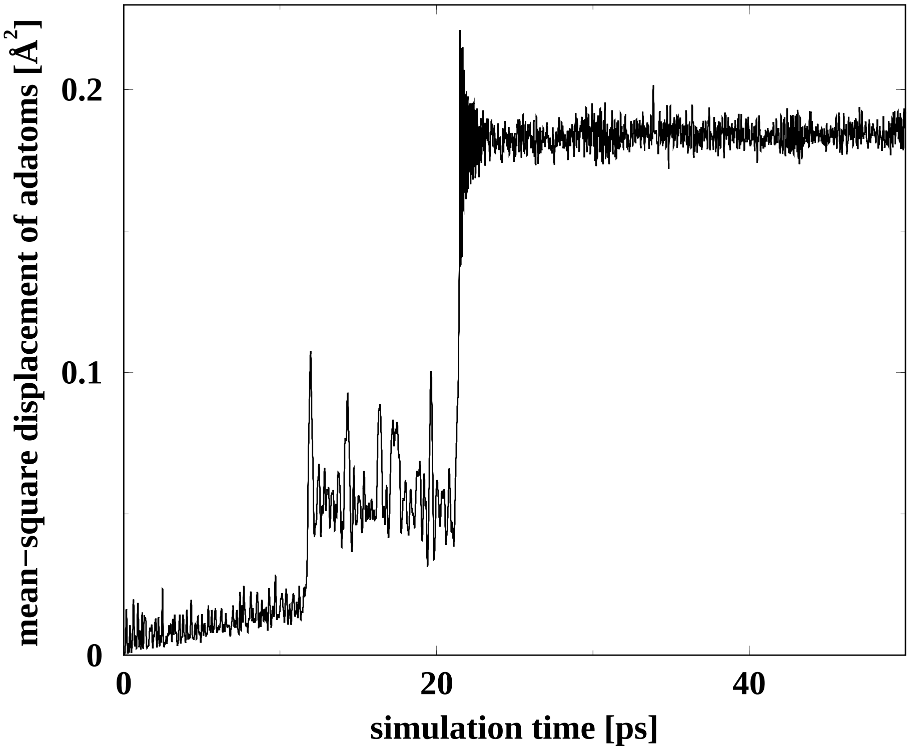

Figure 3.33: Tip-induced lateral mean-square displacement of all adatoms $\Sigma|r_i^2|$

The mean energy transfer per cycle ΔE can be independently estimated from the work done by the tip given by $W = -\int_0^T F_z v_z dt$. To interpret its evolution we show in Fig. 3.34 the force variation during an oscillation cycle. From Fig. 3.32 we see that apart from nearly-reversible spikes accompanying the force pulses, W exhibits an irreversible increase at each cycle corresponding to the shadowed area in Fig. 3.34. This comes about because sample atoms do not quite respond adiabatically, thus producing a slight asymmetry of the force

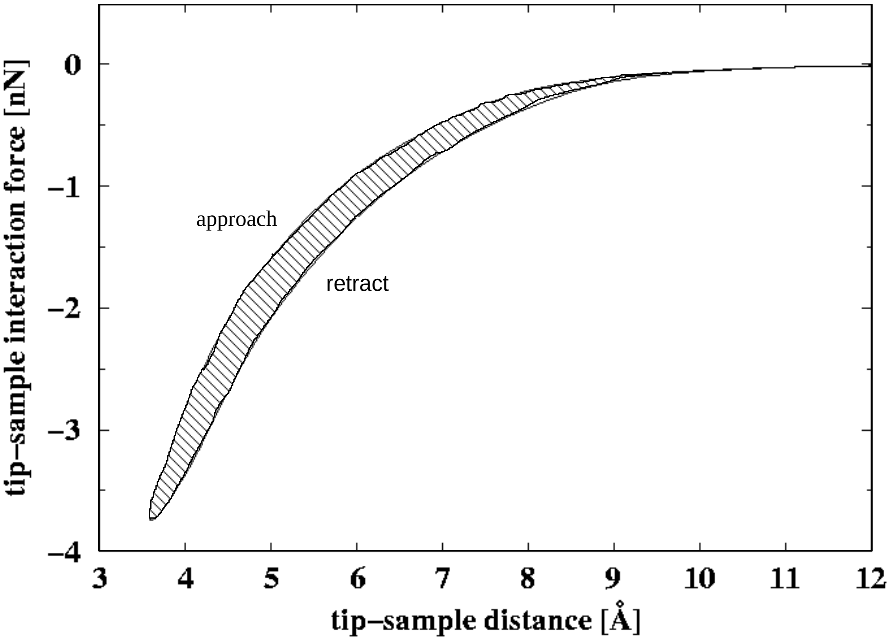

Figure 3.34: Partially nonadiabatic force evolution due to sample relaxation upon rapid approach and retraction of the tip during an oscillation cycle.

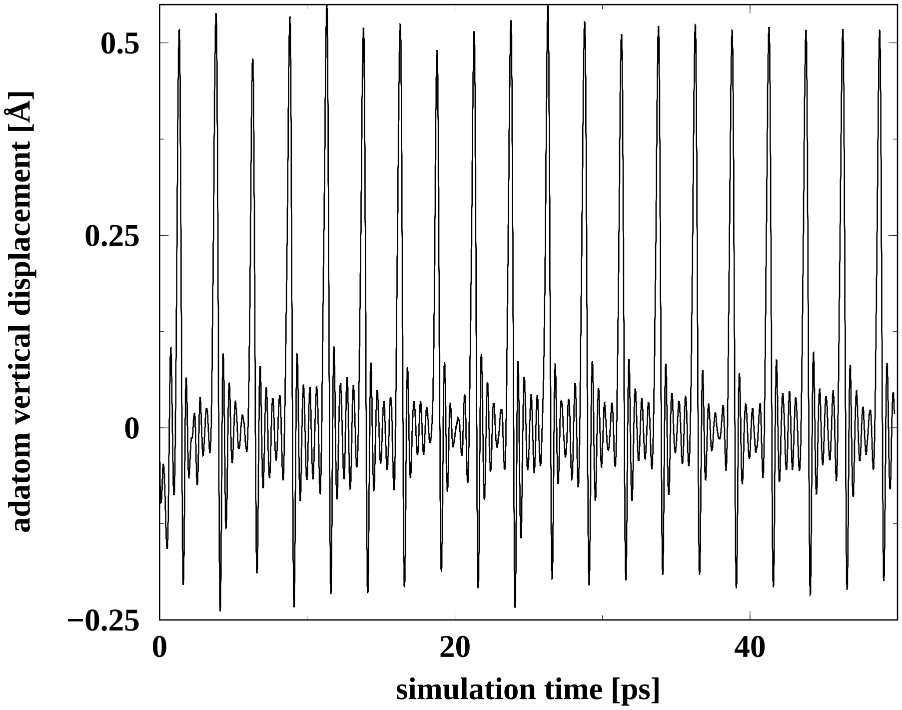

Figure 3.35: Tip-induced relaxation above an adatom site. Minimum tip sample distance is about 3.5 Å, slightly smaller than the critical distance below which the adatom jumps towards the tip in a quasistatic approach.

pulses. The response of the adatom closest to the tip is shown in Fig. 3.35. The asymmetry or nonadiabacity in question should not be associated with quasistatic hysteresis because it increases with the tip oscillation frequency and disappears if $f_{int} < f_{min}$. Moreover, it appears already if d slightly exceeds z_c. If $d < z_c$ more complex phenomena occur, e.g. the adatom jumps to the side or towards the tip. A systematic investigation of such effects, which are very sensitive to the assumed interaction potential, is beyond the scope of this thesis. The irreversible part of the work goes into vibrational energy which is then shared between different modes i.e. turns into heat. In our simulations, this transformation is assisted by the weakly coupled thermostat which regulates the total kinetic energy of all thermalized atoms according to the equipartition rule. We have also calculated the work done by forces on sample atoms close to the tip, and found that it is dominated by the work done by the perpendicular component in the non-contact range.

As discussed above, the thermostat time constant τ_T is chosen shorter than the period so that equilibration is achieved between successive pulses. The heat transferred to the thermostat then looks like a staircase as a function of time, and the average transfer rate coincides with the mean power transferred by the tip (overall energy conservation) [124]. In those early simulations, for a given force $F_{max} = -3.2$ nN at the distance of closest approach d, the energy transfer rate was stronger at the CH site than at the X site, in apparent agreement with the experimentally observed inverted contrast in the damping at constant Δf [8]. On the other hand the damping contrast was weaker at the CH site if the tip was driven with the same amplitude, but coming within the same minimum distance d of the surface. The observation of a contrast in the damping at a constant force $F_z(d)$ is a delicate issue because such a contrast would vanish if the substrate were treated as a continuum subject to delta-function like pulses[98]. Just above z_c we managed to check that damping is roughly proportional to F_{max}^2, as expected for a linear lossy response of the sample [118, 119, 122, 123] by artificially varying the strength of the interaction potential. We found that it is maximum above adatoms, i.e. at sites where the distribution of F_z among nearby atoms is most localized laterally.

In what follows we describe recent simulations performed above the characteristic sites on 7×7 surface indicated in Fig. 3.30 for the following parameters: temperature T=100K, period T_z=2.5ps maximum attractive force F_{max}=-1.2nN. The first 15 of 100ps were skipped to ensure a stationary state. The extracted average energy transfer rate and minimum tip-sample distances are summarized in Table 3.1. From the results we see that the energy transfer is maximum above the adatom and minimum above the hollow site, while the rest atom and corner hole lie in between. We conclude that our predicted damping contrast is neither inverted nor the same as the topography. It is remarkable that the damping above the rest atom is higher than at the hollow site although the local adatom environment is the same, and comparable to that above the corner hole although the latter has a quite different geometry. To understand these differences, one should analyze the site-dependence of the coupling to particular vibrational modes, something beyond the scope of this thesis.

We verified atomic jumps occur more frequently and that the damping in-

	corner hole	adatom	rest atom	hollow site
ΔE [kcal/mol/ps]	0.64	1.3	0.53	0.26
z_{min} [Å]	2.5	3.9	3.3	3.3

Table 3.1: Average energy transfer produced by a tip oscillating above characteristic sites and apparent heights corresponding to a maximum attractive force F_z=-1.2nN of the Si(111)-7×7 reconstructed surface.

creases if we increase the temperature to 300K. Proper comparison with damping measurements requires more simulations, more experiments under carefully controlled conditions and a reliable procedure to predict energy losses under experimental conditions on the basis of those extracted from dynamic simulations performed at much higher frequencies on relatively small samples with a discretized phonon spectrum.

3.7 Interaction energy of selectively moved atoms

To better understand the hysteresis appearing upon approach of the tip above specific surface sites below the critical distance z_c (see section 3.4.3), we calculated the potential energy of an adatom as it is moved above an adatom site away from its equilibrium position. Such simulations are also useful for identifying conditions for controlled manipulations of an adatom which relies on the formation of a potential well in a certain distance range [125]. In a first series of simulations the atoms on the tip but also those of the sample surface, except the adatom under the tip, were kept rigid. The adatom was moved perpendicular to the surface towards the tip. The interaction energy of this atom versus distance from the sample for several tip-sample separations is plotted in Fig. 3.36. In the next series of simulations, similar plots were obtained on the same sample with 6 layers allowed to relax. As shown in Fig. 3.37 the results are remarkably different. At large separations, we observe two potential minima, one close to the sample and one close to the tip, but that closer to the surface is deeper than that closer to the tip. As we reduce the separation, the intervening energy barrier gets smaller and the distance between the two minima reduces, finally the energy barrier vanishes and the two minima merge into a single one. In the case of a rigid sample, the minimum close to the surface remains the deepest one as it continuously merge into the single minimum as the tip-sample separation is decreased. In the case of the deformable sample, the barrier is much lower at the largest separation and, more importantly, the single minimum develops closer to the tip. This implies that the adatom, originally close to the surface, would jump towards the tip below the separation $z_c \simeq 3.7$ Å for which the minimum near the surface disappears. This jump is analogous to the jump-to-contact of a soft cantilever, except that the underlying instability is due to the compliance of the adatom and of the sample, and is favoured by the strong attractive interaction potential used in these simulations. Besides being sensitive to the assumed interaction, the behaviour at small separations is likely to be strongly affected by the deformability of the tip [14] which has not been considered in our work.

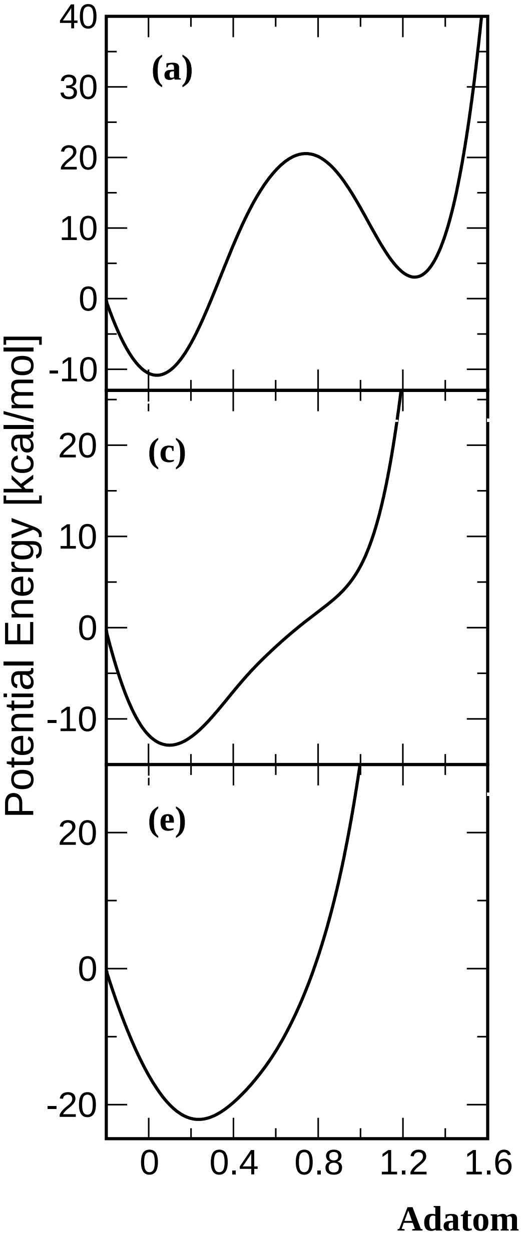

Figure 3.36: Potential energy of an adatom versus height above the surface and with the tip placed above an adatom site at several distances (a) 3.8Å (b) 3.6 Å (c) 3.5 Å (d) 3.4 Å (e) 3.3 Å. The prerelaxed sample with its top adatom layer at height zero was kept rigid.

3.8 Adatom manipulation attempts

3.8.1 Introduction

Originally designed to image surfaces[86, 1, 90], scanning probe techniques have also proved to be efficient for modifying the surface at nanoscopic scales [126].

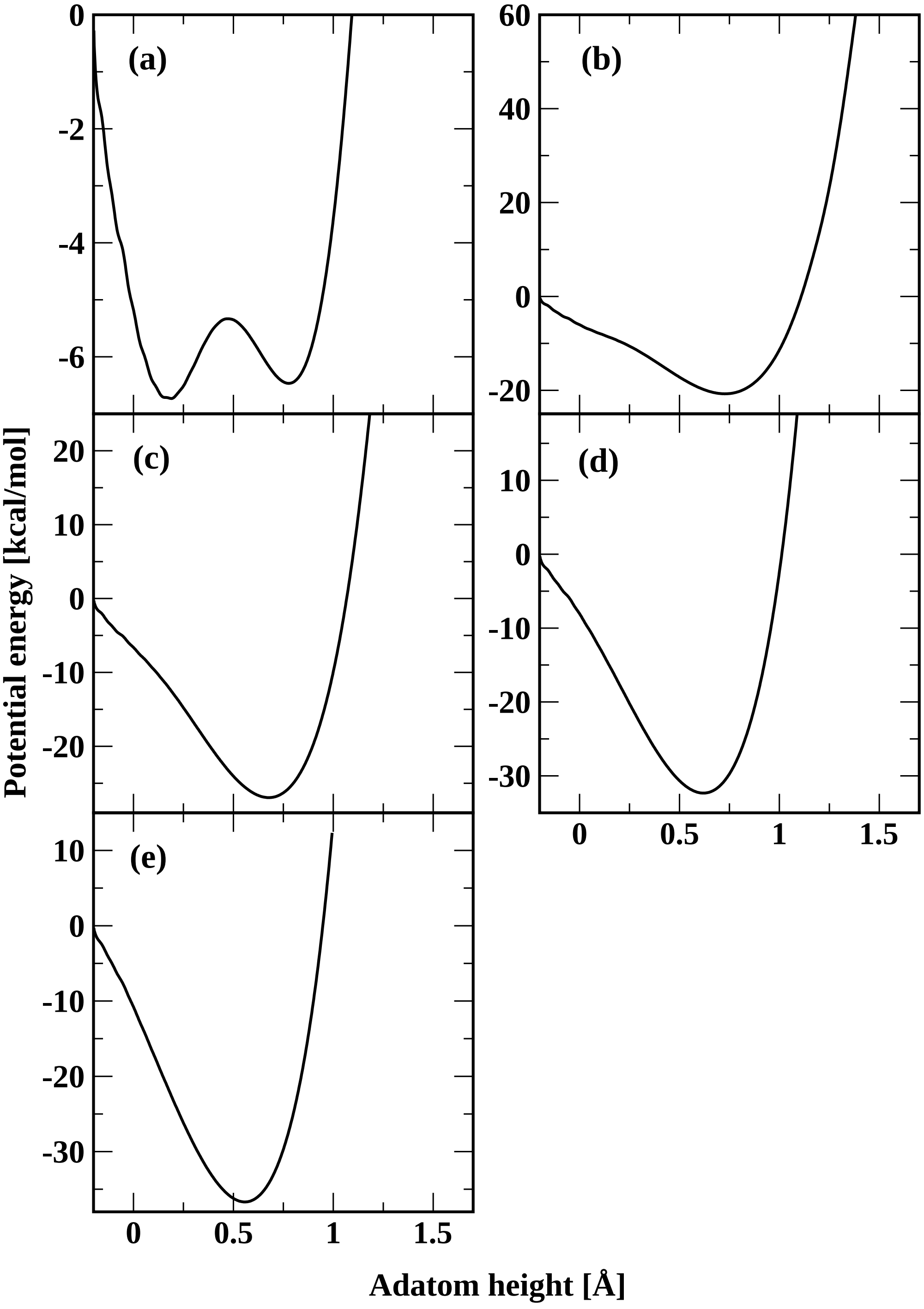

Figure 3.37: Potential energy of adatom versus height between surface and tip above an adatom site at tip-sample distance (a) 3.8Å (b) 3.6 Å (c) 3.5 Å (d) 3.4 Å (e) 3.3 Å. The sample was allowed to deform.

First evidence came from the observation of the consequences of a contact between a scanning probe tip and the studied surface. For instance, Li *et* al [127] observed that the mechanical interaction between a scanning tunneling microscope(STM) tungsten tip and a Au surface led to the creation of nanoscopic pits. Another kind of nano-patterning was achieved by the formation of mounds on the surface by field-emitting atoms from a gold tip [128]. The dimensions of these created nanostructures were typically 100-300Å . Manipulation with a scanning probe made a major step when low-temperature experiments in the group of D. Eigler showed that a STM tip could even control a single adatom with an impressive accuracy [129]. According to the classification of Stroscio and Eigler [130], manipulation processes can be classified in two categories. Vertical processes involve atom transfers between the tip and the surface, voltage pulse or direct tip-surface approach being used for that purpose. Adsorbates or even native surface atoms can be either permanently extracted by the tip [131, 132, 133, 134, 135, 136, 137, 138, 139, 140, 141, 142], or redeposited at another location [143, 144, 145]. This mode has been theoretically studied by several groups [146, 147, 148, 149, 150, 151, 152]. In lateral processes, manipulated atoms, clusters molecules stay on the surface. The scanning probe tip either (i) traps the object in the vicinity of its apex and pulls it [129, 145, 153, 154], (ii) pushes the object along a particular "easy" path [155, 156, 157, 158, 159, 160, 161], or (iii) enhances diffusion via voltage pulses [162, 163].

The potential of lateral manipulation has not been completely explored. Successful experiments have been performed for very small objects, like Xe atoms on Ni(100) [129], CO molecules and Pt atoms on Pt(111) [153], Cu, Pb atoms, and CO, Pb_2, C_2H_4 molecules on Cu(211) [145, 154, 164]. However, in these studies, all supporting substrates are metallic surfaces. Their low diffusion energy barriers make manipulation easier. Theoretically, several calculations of the lateral manipulation of one single atom have been done, and it has been found that single atoms can be manipulated on metallic or insulating substrates. To our knowledge, the manipulation of one unique atom on a surface having a significant technological importance has not been achieved yet. The Si(001) and Si(111) surfaces, heavily used in the electronic industry, are interesting and still unprobed candidates. Recently Pizzagalli *et al* [165, 166] have shown that one single Ag atom deposited on the Si(100) surface may be manipulated by a silicon tip scanned at constant height or constant force in a direction along which diffusion is relatively easy. Such manipulation attempts have hitherto not been performed on the reconstructed Si(111) surfaces either experimentally or theoretically because no such easy directions appear to exist.

In this section we explore the binding energy landscape of an adatom on the Si(111)-7×7 surface and to explain the failure of manipulation attempts.

3.8.2 Binding energy landscape of extra adatom and manipulation attempts

As pointed out in section 3.1 the Si(111)-7×7 surface is still being extensively studied because it exhibits several characteristic feature within its unit cell, namely corner hole, adatoms, restatoms, dimers separating its two inequivalent halves. In the preceding sections, scanlines along the long diagonal of 7×7 reconstructed surface have revealed most of those special features, as well as point defects, in particular extra adatoms. STM studies involving the generation and diffusion [111] of such adatoms and of their role in the growth of the Si(111)-7x7 surface [167, 168] stimulated Cho and Kaxiras [105] to compute the binding energy of an extra adatom at several sites between native adatoms. In that computationally expensive LDA study these authors considered a 4x4 surface unit cell obtained by laterally repeating the 2x2 cell with with nearest neighbour adatoms at the vertices which contains one rest atom in one half and an empty threefold hollow site in the other half. These sites, denoted by R and X in Fig. 3.30 are called T and H_3' by Cho and Kaxiras. Contrary to naive chemical intuition, they found that adsorption on top of native adatoms or of rest atoms, which bear unsaturated dangling bonds, is much less favoured than at higher coordination sites surrounding each rest atoms. Based on the relatively small energy differences between those sites (< 0.6 eV), they predicted fast diffusion at room temperature within the surrounding basins of attraction with rare activated jumps across a 1.26 eV energy barrier at the X site between those basins [169]. In order to access the strong dissimilarities between different

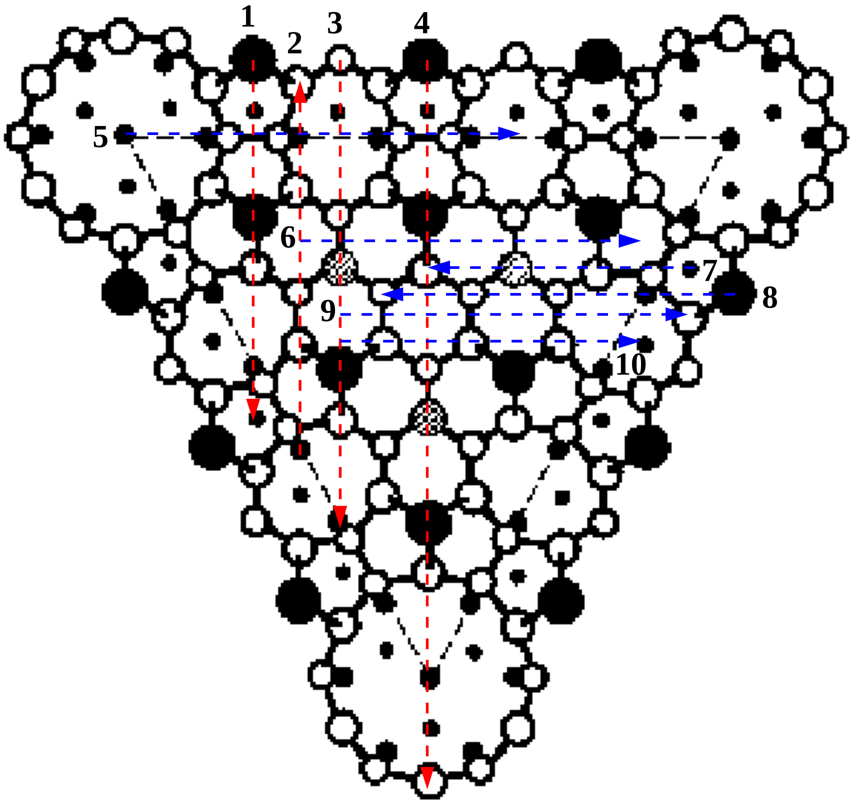

Figure 3.38: (colour) The paths used for determining the potential energy landscape of an extra adatom. They are numbered from left to right and top to bottom; The arrows show the scan direction; long dashed lines encompass the faulted half of the 7x7 unit cell.

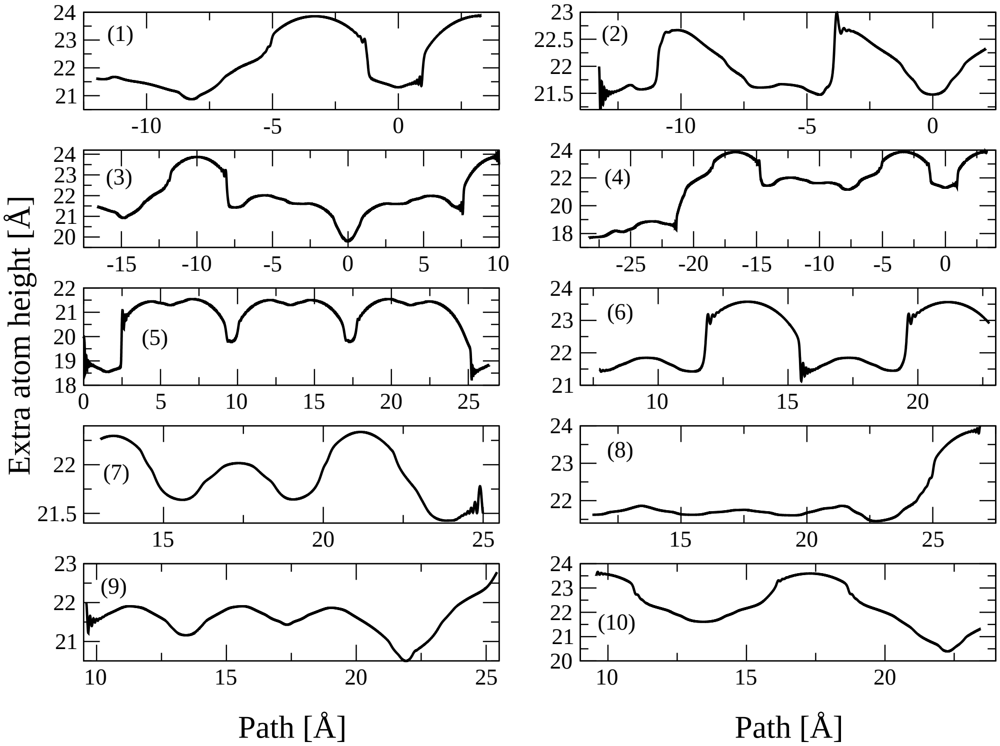

Figure 3.39: Extra atom heights above the top adatom layer of the rigid sample during slow motion at 100m/s along each of the paths shown in Fig. 3.38.

sites on the surface we performed calculations along the scanlines shown in Fig. 3.38 which pass through between all characteristic sites of interest. A good understanding of the binding energy landscape is a prequisite for possible lateral manipulation.

In a first series of calculations the sample atoms were kept in their T=0 prerelaxed positions and the extra atom was allowed to interact with neighbouring atoms via the Stillinger-Weber potential described in section 1.2.2. The extra atom was moved slowly and its coordinates perpendicular to the surface and along the scan direction were allowed to relax using damped MD(see section 1.5.4). As a consequence, the corresponding force components remained almost zero except when the extra atom adsorption configuration suddenly changed. The ensuing vibrations can be easily recognized but still are rapidly damped on the scanning time scale if the time constant δ_T of the thermostat is appropriately close. Such jumps are seen in Fig. 3.39 and are accompanied by temperature spikes which in turn give rise to steplike changes in the heat transferred to the thermostat. Substracting the heat transfer from the internal energy of the sample, we obtained the potential energy variations ΔU of the extra adatom which are plotted in Fig. 3.40. using a common origin corresponding to adsorption above a native adatom. Configuration changes manifest themselves as

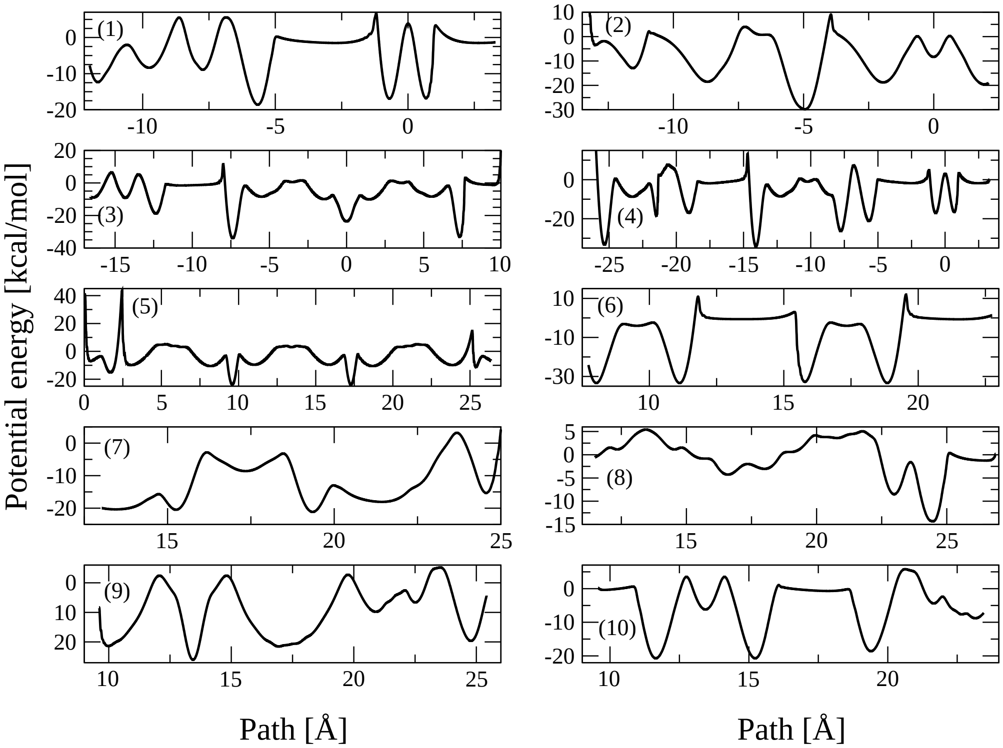

Figure 3.40: Potential energy variations of the extra atom along the paths shown in Figs. 3.38 and 3.39; labels identify specific sites (see text).

spiky cusps in ΔU which are somewhat distorted by the substraction procedure, because the underlying jumps are slightly smeared by the finite τ_T.

By matching the features apparent in Figs. 3.39 and 3.40 to the location of particular sites in Fig. 3.38, one recognizes that the potential energy landscape consists of disjoint dislike minima corresponding to adsorption above native adatoms and above corner hole centers. In addition, numereous minima apparently belong to a single continuous sheet extending between those freatures. The corresponding adsorption heights vary less than ±1Å about that of native adatoms. These minima can be classified as follows:

- deep one (-1.4eV) mainly above the hollow sites surrounding the rest atoms(denoted H_3 as in Ref.[105]),
- slightly higher ones at the center of the half unit cell (X) and of the holes between dimers (DH),
- intermediate ones (-0.8eV) above the 2nd layer sites connected to adatoms (T) and in the pentagons on each side of the dimers (P),
- low ones (-0.35 eV) above rest atoms (R), above 4th layer atoms connected to the dimers (D_4) and on both sides of the holes between dimers (H_5, H_7),

- small ones (~ 0 eV) aboce 3rd layer sites (T_4) surrounding the rest atoms.

The rounded cusps or, rather, ridges separating those minima can be attributed to the rapid onset of the SW potential. Whereas details depend on the assumed interaction, the occurence of a strongly corrugated adsorption energy landscape with disjoint sheets can be expected for the Si(111)-7x7 surface in view of its extensive reconstruction. On the other hand, no noticable differences are apparent between faulted and unfaulted halves of the unit cell i.e. on both sides of O in sections 1 to 4 (except near the above-mentioned jumps). Many of the minima are anisotropic, consistent with the lateral symmetry of the respective sites. In particular, the minima at the H_3 sites, being only symmetric with respect to reflection in the plane passing through the neighbouring adatom and rest atom, are slightly displaced towards the latter. This explains why the appear narrower and deeper in section 3 than in sections 6 and 9. Compared to Cho and Kaxiras, the basin of attraction around each rest aton is split into three bean-shaped valleys because T_4 sites are much less favoured in our case. Moreover, judging from sections 2 and 7, the B_2 bridge sites are saddle points rather than minima. Another discrepancy is the occurence of appreciable minima at the sites labelled T, which appear to be maxima in Fig.2 of Ref. [105].

Besides electronic transfer effects which are known to be important in DAS-type reconstructions [54, 55], but can not be reproduced by the SW potential adopted i this work, some of the above discrepancies could be due to the relaxation of sample atoms around of the extra adatom. We therefore repeated computations similar to those described above, except that atoms, in the top six layers of the sample to relax while the extra adatom was slowly moved along parts of some of the points in Fig. 3.38. Although these paths were intentionally chosen away from native adatoms, we found that the latter tended to be attracted to the extra adatom. This consistent with the foundation of dimers, which was found when the extra adatom was let free (see section 3.4.3). As a consequence, the energy landscape was modified in such a complex fashion that its investigation become difficult without a large number of additional simulations.

We therefore limited subsequent simulations to lateral manipulation of an extra adatom, keeping the sample rigid, using the previously determined landscape as a guide and the first interaction potential with the tip described in section 3.3.

Moreover, we restricted this work to quasistatic manipulation in the interior of one half unit cell. Successful lateral manipulation requires that the force exerted by the profile tip along the scan direction exceeds the maximum restoring force associated with tha binding of the adatoms to the substrate, i.e. the maximum slope of its adsorption energy landscape along that direction.

The condition in question is valid as long as the interactions of the adatom with the tip and the substrate are additive. If it is satisfied, even the adsorption site corresponding to the steepest minimum will be destabilized below a certain distance to the tip apex, and the adatom can then jump towards the tip and follow it in a series of stick-slip events [162].

Estimating maximum slopes along easy directions on the continuous binding energy sheet from lines 7 to 9 in Fig. 3.40, we find critical restoring forces of about 2.5 nN near the minima at B_2 and X sites. This value should be compared to the maximum force in the scan direction on the adatom, which is in turn approximately equal to the corresponding chemical force on the tip in the vicinity of a native adatom. For the noncontact scans at a constant height of 4Å in Fig. 3.15, this maximum force was only 0.25nN while the perpendicular force reached -1.5nN. On the other hand, for the similar scans at 3.5Å, during which the tip picked up and redeposited native adatoms in a rather uncontrolled way, the restoring force in the scan direction reached 2nN in the interval where the perpendicular force was about -5.5nN. This comparison suggests that controlled manipulationn of a Si adatom, if at all feasible, might only be achieved in a narrow range of tip-sample separation along very particular paths. We focused our attention on line 8 because it exhibits the weakest variations in the equilibrium height and energy of the extra adatom. This line actually lies close to a ridge of the adsorption energy landscape, but it may be converted to a minimum with respect to adatom displacements transverse to the path if attraction to the tip apex is sufficiently and localized. We have tried to do manipulate the extra adatom from its relaxed position at one of the T_4 minima by placing our model silicon tip nearby and moving slowly at constant height or perpendicular force using different heights and force values within the range suggested by the preceeding estimates. At the smaller height or stronger force setpoints we observed that the extra adatom soon jumped toward the tip climbed parallel to one of its facets and thus completely decoupled from the sample after sometime. At larger tip height or weaker force setpoints, the tip moved away without pulling the extra atom and extra atom did not change its original relaxed position significantly. By adjusting the height of the tip or the force setpoint we managed to find some optimum values. Although we were able to pull out the extra atom from original relaxed position over a short distance move with the tip, it formed a dimer with an intrinsic adatom as soon as it come to the vicinity of a native adatom site and then stayed at bound close to that position, as the tip moved away. Thus it appears that controlled lateral manipulation of an extra Si adatom is impossible of the $Si(111)-7\times 7$ surface. On one hand, this heavily reconstructed surface exhibits many deep and narrow binding energy minima not connected by any obvious easy diffusion paths like along dimer rows on the $Si(001)$ surface [165]. On the other hand, the interaction with the tip assumed in our manipulation attempts unduly favors adatom jumps towards the tip and further upwards at distances below the rapid onset of the added SW potential. However, the latter favours dimerization with any nearby native adatom. Because these two effects, which preclude successful lateral manipulation, appear to be onset in more accurate DFT calculations [170, 105], different conclusions might emerge if a more adequate interactions were used. Owing to time limitations, this could not be attempted within the framework of this thesis.

General Conclusions and Outlook

Quantum and classical molecular dynamics techniques have been applied and developed to understand the structure of silicon surface reconstructions, defects, model silicon tips, and various aspects of related nc-AFM experiments. Most of the characteristic features of the silicon (111)–7x7 reconstructed surface and typical surface defects are revealed in different simulated operation modes of nc-AFM. Existing experimental and theoretical results are reproduced although there are still some deviations attributed to assumptions underlying the models used.

- **Surface reconstructions**

  Summarizing the results described in chapter 2 and Appendix C, we conclude that the local-orbital based linear scaling TB scheme proposed by Kim *et al*[30] reproduces the correct configurations of representative silicon surface reconstructions. Except for a few discrepancies which can be traced to inadequacies of the tight-binding description itself, satisfactory geometries are obtained with the simpler parametrization of Bowler *et al*[34] and with local orbitals constrained to vanish beyond second nearest neighbours. This even applies to the metallic $Si(111) - 5{\times}5$ surface provided that the computational surface unit cell encompasses an even number of dangling bonds. These encouraging results open the door to applications to larger systems exploiting the linear-scaling capability of this computational scheme, e.g. involving interactions on and between silicon clusters and surfaces exposing different faces with or without passivating hydrogen atoms. Such computations would require more powerful computational resources. However, it is important to keep in mind that a higher level of accuracy appears required to quantitatively describe surface energy differences between alternative (meta)stable structures.

- **Different nc-AFM imaging modes**

  Molecular dynamics simulations can be designed to better understand the origin of true atomic resolution non-contact atomic force microscopy experiments, especially the effect of different tip-sample interactions on the observed atomic resolution. This has been illustrated for the Si(111)-7×7 surface. We used MD calculations to simulate very recent experiments and obtained reasonable agreement using the experimental parameters as inputs to the simulations. Our simulated normal contrast images are consistent with experimental work which has indicated that attractive chemical bonding forces are responsible for this form of contrast. We also conclude that the sometimes observed inverted contrast is due to short range, repulsive tip–sample interactions arising from a chemically non–reactive tip apex. However, stable imaging is more difficult than in the attractive force regime. Non-contact imaging under those conditions is only possible in the presence of a moderate long-range attractive interaction, but is more prone to noise and instabilities, as observed experimentally. Our observation and interpretation of inverted contrast indicates that it should be possible to obtain atomic resolution on non-reactive surfaces. Further work concerning the preparation and modeling of stable chemically non–reactive tips is required.

In our simulations all adatoms in the surface unit cell appeared symmetric and of equal height; this comes about because the assumed interaction potentials cannot describe subtle electronic rearrangements. This is also the reason why we do not image rest atoms in contrast to some experiments. The contrast, i.e. the adatom-corner hole height difference, is very sensitive to the long-range interaction, in other words the overall tip shape plays an important role (except in constant height scans). That might be the reason why the observed height difference often varies between different measurements. We also have verified that the much easier to compute constant $\sqrt{UF_z}$ scanlines almost exactly match constant Δf scanlines with the short-range interaction alone and closely correspond to Δf scanlines if the VdW long-range interaction is also included.

The short-range interaction assumed in most of our simulations tends to unduly favor adatom jumps along the surface and to the tip below a separation z_c which appears somewhat large. A few simulations performed with the interaction matched to the results of first-principles computations Perez et al above an adatom suggest that z_c lies close to the point of zero force, in contrast to our preliminary conclusions in Ref. [171]. At the distances above the force minimum (maximum attraction) our computed noncontact scanlines are mainly sensitive to the range rather than the strength of the tip-sample interaction. Below z_c, stable noncontact operation appears impossible and we predict that irreversible wear of adatoms would then occur in a quasistatic AFM experiment even if the cantilever is prevented from jumping.

- **Energy transfer**

  Promising results have been obtained by oscillating a rigid pyramidal tip with relatively high frequency above specific sites of the Si(111)-7x7 surface. Although the absolute values of energy transfer to the thermostat cannot be compared directly to existing experiments, they indicate maximum energy transfer above adatoms in the case of normal contrast, in apparent agreement with recent experiments [103].

- **Manipulation**

  An extra adatom was moved along selected lines to select a candidate path for controlled lateral manipulation on the Si(111)–7x7 surface by observing the height and potential energy variation. The results showed that such manipulation with an AFM tip alone would be very difficult since very high energy barriers are unavoidable and the tip-sample interaction appears too weak to flatten those barriers.

As suggestions for future work, we propose the following:

i) It would be interesting to repeat computations of different nc-AFM scans with a pyramidal tip with the atoms near the apex allowed to relax. This change should bring computational results closer to the experimental ones since the relaxation of tip atoms is considered to be important [14, 170]. This also might improve comparison with damping measurements;

ii) More simulations should be performed, at least at different values of the set point force along the long diagonal, to better understand and quantify the damping mechanism and the observed site-dependent variations;

iii) Computations with a more reliable short-range interaction potential would be desirable to simulate the physical phenomena occurring at smaller tip-sample separations, in particular the narrow range between noncontact operation and irreversible wear which is in principle suitable for controlled manipulation and monitoring thereof by nc-AFM.

Abbreviations

The following abbreviations are used throughout the thesis:

Abbreviation	Full Name
Å	Ångstrom=10^{-10} meter
AFM	Atomic Force Microscopy
a.u.	atomic unit
BH	Biswas-Hamann
DFM	Dynamic Force Microscopy
DFT	Density Functional Theory
eV	electron Volt=$1.60217733 \times 10^{-19} J$ = 23.049524 kcal/mol
GSP	Goodwin, Skinner, Pettifor
H	Hydrogen
J	Joule
K	Kelvin
LDA	Local Density Approximation
LJ	Lennard-Jones
LO	Localized Orbitals
LR	Localized Region
MD	Molecular Dynamics
NC	Non-Contact
nm	nanometer=10^{-9} meter
nN	nanonewton=10^{-9} Newton
O(N)	Order-N
PBC	Periodic Boundary Conditions
Si	Silicon
SFM	Scanning Force Microscopy
STM	Scanning Tunneling Microscopy
STS	Scanning Tunneling Spectroscopy
SW	Stillinger-Weber
TB	Tight-Binding
VdW	van der Waals

Appendix A

The s-p tight-binding matrix elements

The structure and bonding of carbon and silicon systems in different phases are rather well described in a minimal basis defined in terms of Hamiltonian matrix elements between nominally orthogonal s and p atomic states [43].

On the same atom ($J = J^{'}$), these elements are given by

$$< \alpha_{Jl} | \hat{H}_{TB} | \alpha_{J^{'}l^{'}} >= \begin{cases} E_s & if \quad l = l^{'} = s \\ E_p & if \quad l = l^{'} = p_x, p_y, p_z \\ 0 & if \quad l \neq l^{'} \end{cases}$$

Between nearest neighbours ($J \neq J^{'}$), the matrix elements can be written as,

$$E_{Js,J^{'}s} = V_{ss\sigma}$$

$$E_{Js,J^{'}p_x} = -E_{Jp_x,J^{'}s} = lV_{sp\sigma}$$

$$E_{Js,J^{'}p_y} = -E_{Jp_y,J^{'}s} = mV_{sp\sigma}$$

$$E_{Js,J^{'}p_z} = -E_{Jp_z,J^{'}s} = nV_{sp\sigma}$$

$$E_{Jp_x,J^{'}p_y} = -E_{Jp_y,J^{'}p_x} = lm(V_{pp\sigma} - V_{pp\pi})$$

$$E_{Jp_x,J^{'}p_z} = -E_{Jp_z,J^{'}p_x} = ln(V_{pp\sigma} - V_{pp\pi})$$

$$E_{Jp_y,J^{'}p_z} = -E_{Jp_z,J^{'}p_y} = mn(V_{pp\sigma} - V_{pp\pi})$$

$$E_{Jp_x,J^{'}p_x} = -E_{Jp_x,J^{'}p_x} = l^2V_{pp\sigma} + (1 - l^2)V_{pp\pi}$$

$$E_{Jp_y,J'p_y} = -E_{Jp_y,J'p_y} = m^2V_{pp\sigma} + (1-m^2)V_{pp\pi}$$

$$E_{Jp_z,J'p_z} = -E_{Jp_z,J'p_z} = n^2V_{pp\sigma} + (1-n^2)V_{pp\pi}$$

where l, m, n are the direction cosines of the vector $\mathbf{R}_{J'} - \mathbf{R}_J$, joining neighbours at sites J and J',

$$l = \frac{R_{J'x} - R_{Jx}}{|\mathbf{R}_{J'} - \mathbf{R}_J|}$$

$$m = \frac{R_{J'y} - R_{Jy}}{|\mathbf{R}_{J'} - \mathbf{R}_J|}$$

$$n = \frac{R_{J'z} - R_{Jz}}{|\mathbf{R}_{J'} - \mathbf{R}_J|}$$

Appendix B

The O(N) TB program input variables and options

The tight-binding linear-scaling program used by us was initially developed by Dr Giulia Galli and her coworkers at IRRMA (Institut Romand de Recherche Numérique en Physique des Matériaux), EPFL (École Polytechnique Fédérale de Lausanne), Switzerland. Minor changes have been implemented for better performance and for different parametrizations.

This program can be used for simulating silicon and carbon systems with and without hydrogen atoms. Possible input parameters of the program are described below.

B.1 System specification

n: Number of allowed electronic states per atom; in the present version n can be equal to 2, 3 or 4 but we used 3 following Ref. [30].

nx: Maximum number of states per atom

nb: Number of TB basis functions (e.g. nb=4 for s, p_x, p_y, p_z orbitals of silicon)

na: Total number of atoms in the system including all species

nac: Total number of atoms of the first species(silicon or carbon) in the system.

nfix: Number of fixed atoms in the system

ns: Number of occupied states

natlay: Number of atoms/layer (obsolete)

nfile: Character string (two characters) specifying the names of the input and output files inptb'nfile'.d and outtb'nfile'.d

qi0(1),qi0(2): :
qi0(1): half charge of first species (Si or C)
qi0(2): half charge of second species (H)

Qexact: Total half charge of the system

B.2 Computational cell parameters

alat,blat,clat,abcscal :
alat = x-dimension of the cell (Å)
blat = y-dimension of the cell (Å)
clat = z-dimension of the cell (Å)
abcscal : if greater than 1, then volume is scaled.

ibrav Bravais index of the supercell; either 1 (Simple Cubic) or 8 (Orthorhombic).

tau0(ia,1) tau0(ia,2) tau0(ia,3) ratmv(ia)
ia: atom index
tau0: atomic x,y,z coordinates in Å
ratmv: if equal to 1 the atom can move in a MD simulation; otherwise it remains fixed.

B.3 Control parameters

nbeg: a flag that control the step counting and the initialization of the program
nbeg $\leq$ -3: Input wave function coefficients built up from random numbers
nbeg $>$ -3: Input wave function coefficients at time t_0 read from file inptb'nfile'.d

istart: :
istart = 0: Unformatted read of wave function coefficients from file inptb'nfile'.d (all components).
istart = 1: Unformatted read of wave function coefficients from file inptb'nfile'.d (only non-zero components).
istart $\geq$ 2: Formatted read of wave function coefficients from file inptb'nfile'.d.

iend: same as istart but for writing.

taurd:
taurd = true: Atomic coordinates at time t_0 read from inptb'nfile'.d
taurd = false: Atomic coordinates at time t_0 read from unit 5

trmd: :
trmd = true : Atomic coordinates at time $t_0 - dt$ read from inptb'nfile'.d
trmd = false : Atomic coordinates $t_0 - dt$ read from unit 5

iii: unphysical p orbitals of hydrogen atoms set to zero

neish : Numbers of connected bonds used to define localization region (LR) around each atom

dcut : Cutoff radius for LRs

xmol: Option for output in xyz format ("snapshots")

xmopr: Number of steps between successive snapshots

B.4 Molecular dynamics parameters

tfor,ifor

tfor = true: Ionic motion active.
tfor = false: Ionic motion frozen.
ifor = 1: Constant energy molecular dynamics. Newton equations of motions solved with Verlet algorithm
ifor = 2: Damped molecular dynamics with damping parameter smorzi
ifor = 3: Steepest Descent Minimization '
ifor = 4: Constant temperature molecular dynamics (Nosé thermostat)

deltati,massi,smorzi :

deltati : time step for integration of ionic motion (in atomic unit a.u.)
massi : ionic mass
smorzi : damping parameter

trandi,trandv,arandi :

trandi = true and trandv = true : Randomization of the initial atomic velocities
trandi = true and trandv = false : Randomization of the initial atomic positions
trandi= false and trandv= false : No randomization of atomic positions
arandi: amplitude of the randomization

tscale,rscale,tbyalat :

tscale = true: Velocities are rescaled, $v_{new} = rscale * v_{old}$ with rscale specified in input.
tbyalat= true: Coordinates are multiplied by the cell dim.(alat)
tbyalat= false : Coordinates are NOT multiplied by the cell dim.(alat).

qmass,tkeli,tkelf,ntkel: used when ifor = 4 (Nosé thermostat).

qmass : "mass" associated with the Nosé thermostat variable
tkeli : initial temperature of the system (degree K)
tkelf : final temperature of the system (degree K)
ntkel : number of intermediate T intervals between tkeli and tkelf.

B.5 Electronic parameters

ipur, purrat, text : Purification of wave functions

ipur : index of purification method
purrat : scaling factor of wave function, valid if ipur=2
text : (logical variable) if initial wave function has to be extrapolated

tprint, ieigvec : Diagonalization of Hamiltonian

tprint = true: if Hamiltonian is diagonalized
ieigvec = true: if eigenvectors are calculated

deltat,emass,smorz :

deltat : time step for integration of electronic evolution; active only if tsde

= true
emass : fictitious mass for electronic evolution; active only if tsde = true
smorz : damping parameter for electronic evolution (active only when tsde = false and tcg = false)

nstep,nstcg,iprint :
nstep : number of electronic steps per ionic step for minimization of wave functions
nstcg : number of steps per ionic step for conjugate gradient minimization of wave functions
iprint : number of iterations after which wave function coefficients are written on file.

tsde,tcg(logical): flags for electronic minimization of wave functions
tsde = true and tcg = false : electronic min. by steepest descent
tcg = false and tsde = false : electronic min. by damped molecular dynamics
tcg = true and tsde = false : electronic min. by conjugate gradients.

tbrand,arand :
tbrand = true: initial wave functions are given a random displacement : psi <– psi*(1+arand*(caso-.5)) where caso is the randon number generator.
tbrand= false : no randomization of the wave function coefficients
arand: amplitude of the random displacement

rmu,uh(=uparh),tentropy :
rmu : electronic chemical potential (eV).
uh : strength of the Hubbard-like term (eV).
tentropy : if entropy is introduced at finite temperature (it does not work properly)

trmu,rmurat,mustep : chemical potential adjustment
trmu : (logical variable) if the chemical potential is adjusted at each mustep with first-order proportional feedback
rmurat : strength of the feedback, valid if trmu is true
mustep : step length of adjustment

epss...fc4 : TB parameters

Appendix C

Influence of Various Factors in O(N) TB Simulations

As explained in section 1.3.5, the use of local orbitals assumed to vanish outside finite localization regions is the crucial approximation leading to linear scaling. O(N) TB computations are efficient if the range of TB interactions and size n of the LR(the maximum number of neighbours connected to each central atom by n bonds) can be chosen as small as possible without unduly sacrificing accuracy. For this reason we have performed test calculations with n=2 and n=3 LRs for the two TB parametrizations described in section 1.3.3 and different slabs. Representative bond lengths obtained for the $Si(111) - 5{\times}5$ reconstruction are shown in Table C.1. Column 1 and 2 show the results obtained with the more complex and the simpler parametrizations using a symmetric slab with 8 layers(not counting adatoms) and n=3. Column 3 shows the results obtained with the same LR and using the same TB parameters as in column 2 but for a slab with 6 layers, passivated by hydrogen atoms at the bottom. Column 4 shows results obtained for the same TB parameters and slab as in column 3, but using n=2. From the results one sees that these factors have little influence on the final relaxed geometry.

Table C.1: Comparison of bond lengths in surface layers of the $Si(111) - 5 \times 5$ reconstruction computed for different TB parametrizations, slabs and localization regions; 1 - Adatom-first layer atom; 2 - Adatom-second layer atom; 3 - Rest atom-second layer atom; 4 - Dimer; 5 - Dimer atom-third layer atom; 6 - Corner hole atom-fourth layer atom

	parametrization (symmetric slab, 3 LR)		LR(with H, Bowler *et al*)	
Bonds	Kwon *et al*[33]'s	Bowler *et al*[34]'s	3 LR	2 LR
1	2.545	2.56	2.550	2.545
2	2.58	2.58	2.575	2.580
3	2.44	2.44	2.435	2.446
4	2.41	2.42	2.417	2.414
5	2.39	2.39	2.39	2.39
6	2.44	2.41	2.408	2.410

Appendix D

The Classical Molecular Dynamics Program Options

The molecular dynamics program was written by Thomas Bonner during his PhD study at the Institute of Physics, University of Basel and originally applied to study indentation and friction on self-assembled monolayers with a gold tip. He then started to study non-contact AFM on silicon samples with a single-atom silicon tip. The current author further developed this program for a finite size silicon tip, constant force and frequency shift scans, surface defects; determination of energy landscapes.

Most of the input to the program is done in the file `user.sel`. Hence, the whole program must be recompiled after changing any settings in `user.sel`. A few options are set in `computer.sel`, which tells the program about the computer used(graphics, operating system and compiler etc.). All input is done in form of CPP-macros which means that the source code must be preprocessed by a C-preprocessor or any compatible program (already part of Fortran-compilers under Unix). Global definitions which are not intended to be changed are defined in the file `global.fi`, while other `*.fi`-files hold the common blocks of the program. Whenever one common block is used, the appropriate `*.file` is included with the #include "..."-macro. This ensures that every common-block is only defined at one place and prohibits any misunderstandings between differently defined common blocks in different program parts.

The adjustable parameters in the `user.sel` are described below.

D.1 Computational parameters

GRAPHICS: use online graphics while carrying out the simulation.

BENCHMARK: generate a benchmark version for testing. No in- or output is done.

DEBUG: generates a debug version with checks and tests done in the program during calculation.

SKIP_DATA_FIRST: trajectory sampling is done only after a certain time, thus eliminating any artificial effects from the initialization phase on the output plots.

SKIP_DATA_TIME: picoseconds of data skipped if the previous option is switched on

DO_FIRST_STEPS: initialization steps to be performed before time count.

MOVE_BOX: moves all atoms into the original simulation cell when a pdb-file is written.

D.2 System specifications

simffm moving AFM tip.

SAM self-assembled monolayer sample.

Gold gold tip or surface

Silicon silicon sample

Note: In this work we only presented results on silicon, the results on SAM and Gold were presented elsewhere [172].

D.3 Simulation parameters

Gear: use Gear predictor-corrector algorithm for integration

NO_HOOVER: use Nose-Hoover algorithm

Si001: use Si(001) sample

Si111: use Si(111) sample

VDW: include macroscopic van der Waals interaction in the tip-sample interaction

RIGID: keep the sample rigid

BH_MODIFIED: Biswas-Hamann parameters A_n and λ_n (n=1,2) adjusted so that the force-distance curve fits the curve computed by Perez *et al* [170] above an adatom

DOUBLE_3 :the strength of 3-body part of SW potential is doubled

DT_FS : time step in femtoseconds

TEMP_SI: set temperature T_0 for the sample

QQ_SI: value of $\delta t/\tau_T$ in Berendsen velocity rescaling

QQ: Q-mass in Nose thermostat

MISSING_ATOM: there is a missing adatom on the surface

EXTRA_ATOM: an extra adatom is included

EXTRA_ATOM_FREE: the extra atom is free to move

MOVE_ALONG_Z: the extra adatom is moved along z with a finite constant velocity

XY_RIGID: the x, y coordinates of the extra atom kept fixed

DIRECTION_X: the extra adatom is moved along x is not allowed to relax along y

DIRECTION_Y: same as above but for motion along y

DIRECTION_ARB: the extra adatom is moved along a particular direction in the xy plane

NX: number of unit cells in the x-direction

NY: number of unit cells in the y-direction

NZTOTAL: total number of layers in the z-direction

NZFIX: number of fixed layers in the z-direction

CONST_X: constant X(Force or $\sqrt{|UF_z|}$) scan

FORCE_SCAN: constant force scan

ENER_FORCE: constant frequency shift scan (actually constant $\sqrt{|UF_z|}$ scan).

OTHER_BRANCH: CONST_X scan performed on the repulsive branch

DYNAMIC: the tip is oscillating sinusoidally along z

AMPL: oscillation amplitude

PERIOD: oscillation period

CUT: the tip-sample interaction is switched off when the tip is above a certain height

CUT_RANGE: height of the cut

MOREMASS: tip mass scaling factor (kept equal to one, but kept for historical reasons.)

Bibliography

[1] G. Binnig, C. F. Quate, and Ch. Gerber. Atomic force microscope. *Phys. Rev. Lett.*, 56(9):930, 1986.

[2] F. J. Giessibl. Atomic resolution of the silicon (111)-(7×7) surface by atomic force microscopy. *Science*, 267:68, 1995.

[3] S. Kitamura and H. Iwatsuki. Observation of 7×7 reconstructed structure on the Silicon (111) surface using ultrahigh vacuum noncontact atomic force microscopy. *Jpn. J. Appl. Phys.*, 34:L145, 1995.

[4] T. R. Albrecht, P. Grütter, D. Horne, and D. Rugar. Frequency modulation detection using high-Q cantilevers for enhanced force microscope sensitivity. *J. App. Phys.*, 69:668, 1991.

[5] R. Lüthi, E. Meyer, M. Bammerlin, A. Baratoff, T. Lehmann, L. Howald, Ch. Gerber, and H.-J. Güntherodt. *Z. Phys. B*, 100(165), 1996.

[6] P. Güthner. *Journal of Vacuum Science and Technology B*, 14:2428, 1996.

[7] R. Erlandson, L. Olson, and P. Martenson. *Physical Review B*, 54:8309, 1996.

[8] R. Lüthi, E. Meyer, M. Bammerlin, A. Baratoff, L. Howald, Ch. Gerber, and H.-J. Güntherodt. *Surf. Rev. Lett.*, 4:1025, 1997. The image in Fig. 3(b) of that conference report should represent the topography at a constant frequency shift, it was unfortunately inverted and mislabelled.

[9] N. Nakagiri, M. Suzuki, K. Obiguchi, and M. Sugimura. *Surface Science*, 373:L329, 1997.

[10] T. Uchihashi, Y. Sugawara, T. Tsukamoto, M. Ohta, S. Morita, and M. Suzuki. Role of a covalent bonding interaction in noncontact-mode atomic-force microscopy on Si(111)7×7. *Phys. Rev. B*, 56(15):9834, 1997.

[11] K. Takayanagi, Y. Tanishiro, S. Takahashi, and M. Takahashi. *Journal of Vacuum Science and Technology A*, 3:1502, 1985.

[12] K. Takayanagi, Y. Tanishiro, S. Takahashi, and M. Takahashi. *Surface Science*, 164:367, 1985.

[13] Ruben Pérez, Ivan Štich, Michael C. Payne, and Kiyoyuki Terakura. Surface-tip interactions in noncontact atomic-force microscopy on reactive surfaces: Si(111). *Physical Review B*, 58:10835, 1998.

[14] M. A. Lantz, H. J. Hug, P. J. A. Schendel, R. Hoffmann, S. Martin, A. Baratoff, A. Abdurixit, H.-J. Güntherodt, and Ch. Gerber. Low temperature scanning force microscopy of the Si(111)-7 × 7 surface. *Physical Review Letters*, 84:2642, 2000.

[15] F. J. Giessibl. *Physical Review B*, 56:16010, 1997.

[16] M. P. Allen and D. J. Tildesley. *Computer Simulation of Liquids.* Oxford University Press, Oxford, UK, 1989.

[17] H. Balamane, T. Halicioglu, and W. A. Tiller. Comparative study of silicon emprical interatomic potentials. *Phys. Rev. B*, 46:2250, 1992. and references therein.

[18] J. E. Lennard-Jones. *Trans. Faraday Soc.*, 28:334, 1932.

[19] F. H. Stillinger and T. A. Weber. Computer simulation of local order in condensed phases of silicon. *Phys. Rev. B*, 31(8):5262, 1985.

[20] R. Biswas and D. R. Hamann. *Physical Review Letters*, 55:2001, 1985.

[21] H. C. Hamaker. *Physica*, 4:1058, 1937.

[22] U. Hartmann. *Phys. Rev. B*, 42:1541, 1990.

[23] Jacob N. Israelashvili. *Intermolecular and Surface Forces.* Academic Press, New York edition, 1992.

[24] http://www.nobelprizes.com, 1998.

[25] M. C. Payne, M. P. Teter, D. C. Allan, T. A. Arias, and J. D. Joannopoulos. Iterative minimization techniques for ab initio total-energy calculations: molecular dynamics and conjugate gradients. *Review of Modern Physics*, 64:1045, 1993.

[26] W. Kohn and L. J. Sham. *Phys. Rev.*, 140:A1133, 1965.

[27] G. Galli. *Current Opinion in Solid State and Materials Science*, 1:864, 1996.

[28] D. R. Bowler, M. Aoki, C. M. Goringe, A. P. Horsfield, and D. G. Pettifor. *Modelling Simul. Mat. Sci. Eng.*, 5:199, 1997.

[29] F. Mauri and G. Galli. *Physical Review B*, 50:4316, 1994.

[30] J. Kim, F. Mauri, and G. Galli. Total-energy global optimizations using nonorthogonal localized orbitals. *Physical Review B*, 52:1640, 1995.

[31] D. J. Chadi. *Journal of Vacuum Science and Technology*, 16:1290, 1979.

[32] L. Goodwin, D. R. Skinner, and D. G. Pettifor. *Europhysics Letters*, 9:701, 1989.

[33] I. Kwon, R. Biswas, C. Z. Wang, K. M. Ho, and C. M. Soukoulis. *Physical Review B*, 49:7242, 1994.

[34] D. R. Bowler, M. Fearn, C. M. Goringe, A. P. Horsfield, and D. G. Pettifor. Hydrogen diffusion on Si(001) studied with the local density approximation and tight-binding. *Journal of Physics: Condensed Matter*, 10:3719, 1998.

[35] W. Kohn. *Phys. Rev.*, 115:809, 1959.

[36] N. Marzari and D. Vanderbilt. *Physical Review B*, 56:12847, 1997.

[37] G. Galli and M. Parrinello. *Physical Review Letters*, 69:3547, 1992.

[38] P. Lödwin. On the orthogonality problem connected with the use of atomic wave functions in the theory of molecules and crystals. *Journal of Chemical Physics*, 18:365, 1950.

[39] William H. Press, Saul A. Teukolsky, William T. Vetterling, and Brian P. Flannery. *Numerical Recipes in Fortran: The Art of Scientific Computing.* Cambridge University Press, Cambridge, 1992.

[40] J. C. Slater and G. F. Koster. Simplified LCAO Method for the Periodic Potential Problem. *Physics Review*, 94(6):1498, 6 1954.

[41] M. Born and J. R. Oppenheimer. *Am. J. Phys.*, 84:451, 1927.

[42] O. L. Alerhand and E. J. Mele. Surface reconstruction and vibrational excitations of Si(001). *Physical Review B*, 35:5533, 1987.

[43] Walter A. Harrison. Coulomb interactions in semiconductors and insulators. *Physical Review B*, 31(4):2121, February 1985.

[44] L. Verlet. *Physical Review*, 159:98, 1967.

[45] C. W. Gear. *Numerical Initial Value Problems in Ordinary Differential Equations.* Prentice-Hall, Englewood Cliffs, NJ, 1971.

[46] H. J. C. Berendsen, J. P. M. Potsma, W. F. van Gunsteren, A. DiNola, and J. R. Haak. *Journal of Chemical Physics*, 81:3684, 1984.

[47] Shuichi Nose. A molecular dymanics method for simulations in the canonical ensemble. *Molecular Physics*, 52(2):255, 1984.

[48] Shuichi Nose. Constant temperature molecular dynamics method. *Progr. Theor. Phys. (Japan)*, Suppl. 103(1), 1991.

[49] W. G. Hoover. Canonical dynamics: Equilibrium phase-space distributions. *Phys. Rev. A*, 31(3):1695, 1985.

[50] O. Olson. NANOSENSORS GmbH. *Aidlingen, Germany.*

[51] R. M. Feenstra and M. A. Lutz. *Physical Review B*, 42:5391, 1990.

[52] G. Adams and O. Sankey. Applications of Ab-Initio Quantum Molecular Dynamic Relaxation - Silicon(111)-5 × 5 Surface Reconstruction and Aluminum Deposited on Silicon(100). *Journal of Vacuum Science and Technology A*, 10:2046, 1992.

[53] Guo-Xin Qian and D. J. Chadi. Si(111)-7×7 surface: energy-minimization calculation for the dimer-adatom-stacking-fault model. *Physical Review B*, 35(3):1288, January 1987.

[54] I. Štich, M. C. Payne, R. D. King-Smith, J. S. Lin, and L. J. Clarke. Ab initio total-energy calculations for extremely large systems: application to the Takayanagi reconstruction of Si(111). *Physical Review Letters*, 68:1351, 1992.

[55] Karl D. Brommer, M. Needels, B. E. Larson, and J. D. Joannopoulos. *Ab Initio* Theory of the Si(111)-(7×7) Surface Reconstruction. *Physical Review Letters*, 68:1355, 1992.

[56] Jeongnim Kim, Mei-Ling Yeh, Furrukh S. Khan, and John W. Wilkins. Surface phonons of the Si(111)-7×7 reconstructed surface. *Physical Review B*, 52:14709, November 1995.

[57] R. Car and M. Parrinello. Unified approach for molecular dynamics and density-functional theory. *Phys. Rev. Lett.*, 55(22):2471, 1985.

[58] K. C. Pandey. *Physical Review Letters*, 47:1913, 1981.

[59] K. C. Pandey. *Physical Review Letters*, 49:223, 1982.

[60] F. Ancilotto, W. Andreoni, A. Selloni, R. Car, and M. Parrinello. Structural, Electronic, and Vibrational Properties of Si(111)-2×1 from Ab-initio Molecular Dynamics. *Physical Review Letters*, 65(25):3148, 1990.

[61] J. E. Northrup and M. Cohen. Electronic structure of the pi -bonded chain model and the nonbuckled antiferromagnetic insulator model for the Si(111) surface. *Journal of Vacuum Science and Technology*, 21:333, 1982.

[62] J. E. Northrup and M. Cohen. Reconstruction mechanism and surface-state dispersion for Si(111)-(2×1). *Physical Review Letters*, 49:1349, 1982.

[63] R. I. G. Uhrberg, E. Landemark, and L. S. O. Johansson. *Physical Review B*, 39:13525, 1989.

[64] R. M. Feenstra. *Physical Review B*, 60:4478, 1999.

[65] Michael Rohlfing and Steven G. Louie. Excitons and Optical Spectirum of the Si(111)-2 × 1 Surface. *Physical Review Letters*, 83:856, 1999.

[66] J. E. Northrup, M. S. Hybertsen, and S. G. Louie. Many-Body calculation of the Surface-State Energies for Si(111)2 × 1. *Physical Review Letters*, 66(4):500, January 1991.

[67] J. E. Northrup and M. Cohen. Atomic geometry and surface-state spectrum for Ge(111)-(2 × 1). *Physical Review B*, 27:6553, 1983.

[68] F. J. Himpsel, P.M. Marcus, R. Tromp, I. P. Batra, M. R. Cook, F. Jona, and H. Liu. *Physical Review B*, 30:2257, 1984.

[69] F. Ancilotto, A. Selloni, W. Andreoni, S. Baroni, R. Car, and M. Parrinello. Surface phonons and dipole activity of Si(111)2 × 1 from ab-initio calculations. *Physical Review B*, 43:8930, 1991.

[70] Sung-Hoon Lee and Myung-Ho Kang. Model-Dependent Electronic Structure of the Si(111)2 × 1 Surface. *Physical Review B*, 54:1482, 1996.

[71] D. J. Chadi. Atomic and Electronic Structures of Reconstructed Si(100) surfaces. *Phys. Rev. Lett.*, 43(1):43, 1979.

[72] F. S. Khan and J. Q. Broughton. Simulation of silicon clusters and surfaces via tight-binding molecular dynamics. *Physical Review B*, 39:3688, 1989.

[73] M. T. Yin and M. L. Cohen. *Physical Review B*, 24:2303, 1981.

[74] R. M. Tromp, R. J. Hamers, and J. E. Demuth. *Physical Review Letters*, 55:1303, 1985.

[75] R. E. Schlier and H. E. Farnsworth. *Journal of Chemical Physics*, 30:917, 1959.

[76] A. Ramstad, G. Brocks, and P. J. Kelly. Theoretical study of the Si(100) surface reconstruction. *Physical Review B*, 51(20):14504–14523, 1995.

[77] J. E. Northrup. Electronic structure of Si(100)c(4 × 2) calculated within the GW approximation. *Phys. Rev. B*, 47(15):10032, 1993.

[78] R. J. Hamers and U. K. Köhler. *Journal of Vacuum Science and Technology A*, 7:2854, 1989.

[79] T. Miyazaki, T. Uda, and K. Terakura. Structure models of the C-type defect on Si(001). *Materials Science and Engineering B*, 37:168, 1996.

[80] T. Uda and K. Terakura. Structure model for the type-C defect on the Si(001) surface. *Physical Review B*, 53:6999, 1996.

[81] T. Miyazaki, T. Uda, and K. Terakura. Atomic and electronic origins of a type-C defect on Si(001). *Physical Review Letters*, 84:4128, 2000.

[82] K. Hata, S. Ozawa, Y. Sainoo, K. Miyake, and H. Shigekawa. Electronic structure of the C defects of Si(001) measured by scanning tunneling spetroscope at room and low temperature (80K). *Surf. Sci.*, 447:156, 2000.

[83] G. Adams and O. Sankey. Ab-Initio Molecular Dynamic Relaxation Applied to the Silicon(111)-5×5 Surface Reconstruction. *Physical Review Letters*, 67:867, 1991.

[84] *First NC-AFM Workshop Proceedings, Applied Surface Science*, volume 140. Elsevier Science, 1999.

[85] *The 2^{nd} NC-AFM Workshop Proceedings, Applied Surface Science*, volume 157. Elsevier Science, 2000.

[86] G. Binnig, H. Rohrer, Ch. Gerber, and E. Weibel. Surface studies by scanning tunneling microscopy. *Phys. Rev. Lett.*, 49(1):57, 1982.

[87] G. Binnig, H. Rohrer, Ch. Gerber, and E. Weibel. *Physical Review Letters*, 50:120, 1983.

[88] G. Binnig, H. Rohrer, Ch. Gerber, and E. Weibel. *IBM Journal of Research Development*, 30:355, 1986.

[89] G. Binnig and H. Rohrer. Scanning tunneling microscopy. *Physica*, 127B:37, 1984.

[90] H. Kumar Wickramasinghe. In A. Stroscio and W. J. Kaiser, editors, *Scanning Tunneling Microscopy*, volume 27 of *Methods of Experimental Physics*, chapter 3, page 77. Academic Press, San Diego, 1993.

[91] For an overview of force microscopy see:. Forces in scanning probe methods. In H.-J. Güntheordt, D. Anselmetti, and E. Meyer, editors, *NATO ASI Series E: Applied Science V. 286.* Kluwer Academic Publishers, 1995.

[92] J. Tersoff and D. R. Hamann. Theory and application for the scanning tunneling microscope. *Phys. Rev. Lett.*, 50(25):1998, 1983.

[93] J. Tersoff and D. R. Hamann. Theory of the scanning tunneling microscope. *Phys. Rev. B*, 31(2):805, 1985.

[94] S. Ciraci, A. Baratoff, and I. P. Batra. Tip-sample interaction effects in scanning-tunneling and atomic-force microscopy. *Physical Review B*, 42:7618, 1990.

[95] T. Arai and M. Tomitori. Bias dependence of Si(111)-7×7 images observed by noncontact atomic force microscopy. *Applied Surface Science*, 157:207, 2000.

[96] A. Abdurixit, M. A. Lantz, H. J. Hug, A. Baratoff, P. J. A. van Schendel, R. Hoffmann, P. Kappenberger, S. Martin, and H.-J. Güntherodt. unpublished.

[97] B. Anczykowski, B. Gotsmann, H. Fuchs, J. P. Cleveland, and V. B. Elings. How to Measure Energy Dissipation in Dynamic Mode Atomic Force Microscopy. *Applied Surface Science*, 140:376, 2000.

[98] U. Dürig. *Surf. Interface Anal.*, 27:467, 1999.

[99] U. Dürig. *Applied Physics Letters*, 75:433, 1999.

[100] F. J. Giessibl and H. Bielefeldt. *Physical Review B*, 61:9968, 2000.

[101] S. H. Ke, T. Uda, and K. Terakura. Quantity measured in frequency-shift-mode atomic-force microscopy: An analysis with a numerical model. *Physical Review B*, 59:13267, 1999.

[102] Udo D. Schwarz. *Nanomechanics-Nanochemical Investigations with the Scanning Force Miscroscope*. Habilitationsschrift, University of Hamburg, March 1999.

[103] M. A. Lantz, H. J. Hug, P. J. A. Schendel, R. Hoffmann, S. Martin, A. Baratoff, H.-J. Güntherodt, and Ch. Gerber. *Science*, 291:2580, 2001.

[104] M. Bammerlin et al. *Applied Physics A*, 66:S293, 1998.

[105] K. Cho and E. Kaxiras. Intermittent Diffusion on the Reconstructed Si(111) Surface. *Europhysics Letters*, 39:287–292, 1997.

[106] A. Baratoff and A. Abdurixit. In *presented at First International Workshop on Non-Contact Atomic Force Microscopy*, Osaka, July 21-23, 1998.

[107] C. Argento and R. H. French. Parametric tip model and force-distance relation for Hamaker constant determination from atomic force microscopy. *Journal of Applied Physics*, 80:6081, 1996.

[108] M. Guggisberg, M. Bammerlin, Ch. Loppacher, O. Pfeiffer, A. Abdurixit, V. Barwich, R. Bennewitz, A. Baratoff, and H.-J. Güntherodt. Separation of interactions by noncontact force microscopy. *Physical Review B*, 61:11151, 2000.

[109] T. J. Senten and C. J. Drummond. *Colloids Surf. A*, 94:29, 1995.

[110] N A Burnham, R J Colton, and H M Pollock. Interpretation of force curves in force microscopy. *Nanotechnology*, 4(2):64–80, 1993.

[111] B. C. Stipe, M. A. Rezaei, and W. Ho. Site-Specific Displacement of Si Adatoms on Si(111)-(7×7). *Physical Review Letters*, 79(22):4397, December 1997.

[112] E. Gnecco, R. Bennewitz, T. Gyalog, C. Loppacher, M. Bammerlin, E. Meyer, and H.-J. Güntherodt. *Phys. Rev. Lett.*, 84:1172, 2000. and further references therein.

[113] M. Guggisberg, M. Bammerlin, A. Baratoff, R. Lüthi, Ch. Loppacher, F. M. Battiston, J. Lü, R. Bennewitz, E. Meyer, and H.-J. Güntherodt. Dynamic force microscopy across steps on the si(111)-7×7 surface. *Surface Science*, 461:255, 2000.

[114] Christian Loppacher. *Nichtkontakt Rasterkraftmicroskopie mit Digitalen Phasenregelkreis*. PhD Thesis, University of Basel, 2000.

[115] Ch. Loppacher, R. Bennewitz, M. Guggisberg, O. Pfeiffer, M. Bammerlin, A. Baratoff, and E. Meyer. Experimental aspects of dissipation force microscopy. *Phys. Rev. B*, 62:13674, 2000.

[116] W. Denk and D. Pohl. Local electrical dissipation imaged by scanning force microscopy. *Applied Physics Letters*, 59:2171, 1991.

[117] T. Stowe, T. Kenny, D. Tomson, and D. Rugar. Silicon dopant imaging by dissipation force microscopy. *Appl. Phys. Lett.*, 75:2785, 1999.

[118] J. P. Aime, R. Boisgard, L. Nony, and G. Couturier. Nonlinear dynamic behavior of an oscillating tip-microlever system and contrast at the atomic scale. *Physical Review Letters*, 82:3388, 1999.

[119] J. P. Aime, G. Couturier, R. Boisgard, and L. Nony. Relationship between the nonlinear dynamic behaviour of an oscillating tip-microlever system and the contrast at the atomic scale. *Applied Surface Science*, 140:333, 1999.

[120] B. Gotsmann, C. Seidel, B. Anczykowski, and H. Fuchs. Conservative and Dissipative Tip-Sample Interactions Forces Probed With Dynamic AFM. *Phys. Rev. B*, 60(15):11051, 1999.

[121] U. Dürig. *New Journal of Physics*, 2:5.1, 2000.

[122] U. Dürig. *IBM Research Report*, RZ 3218:#93264, 2000.

[123] Michel Gauthier and Masaru Tsukada. *Physical Review B*, 60:11716, 1999.

[124] A. Abdurixit, T. Bonner, A. Baratoff, and E. Meyer. presented at *The 2nd International Workshop on non-contact Atomic Force Microscopy*, Pontrasina, Sept. 1-4, 1999, and *The 10th International Conference on Scanning Tunneling Microscopy/Spectroscopy and Related Proximal Probe Microscopy*, Seoul, South Korea, July 18-23, 1999.

[125] S. Ciraci, E. Tekman, A. Baratoff, and I. P. Batra. Theoretical study of short- and long-range forces, and atom transfer in scanning force microscopy. *Phys. Rev. B*, 46(16):10411, 1992.

[126] G. Binnig and H. Rohrer. *Rev. Mod. Phys.*, 71:S324, 1999.

[127] Y. Z. Li, L. Vazquez, R. Piner, R. P. Andres, and R. Reifenberger. Writing nanometer-scale symbols in gold using the scanning tunneling microscope. *Appl. Phys. Lett.*, 54:1424, 1989.

[128] H. J. Mamin, P. H. Guethner, and D. Rugar. Atomic emission from a gold scanning-tunneling-microscope tip. *Phys. Rev. Lett.*, 65(19):2418, 1990.

[129] D. M. Eigler and E. K. Schweizer. Positioning single atoms with a scanning tunnelling microsocope. *Nature*, 344:524, 1990.

[130] J. A. Stroscio and D. M. Eigler. Atomic and molecular manipulation with the scanning tunneling microscope. *Science*, 254:1319, 1991.

[131] I.-W. Lyo and Ph. Avouris. Field-Induced Nanometer- to Atomic-Scale Manipulation of Silicon Surfaces with the STM. *Science*, 253:173, 1991.

[132] Ph. Avouris, I.-W. Lyo, and Y. Hasegawa. STM-induced modification and electrical properties of surfaces on the atomic and nanometer scales. In Ph. Avouris, editor, *Atomic and Nanometer-Scale Modification of Materials: Fundamentals and Applications*, volume 239 of *NATO ASI Series E: Applied Sciences*, page 11, Dordrecht, 1993. Kluwer Academic Publisher.

[133] A. Kobayashi, F. Grey, H. Uchida, D.-H. Huang, and M. Aono. Field Ion Evaporation from tip and sample in the STM for atomic-scale surface modification. In Ph. Avouris, editor, *Atomic and Nanometer-Scale Modification of Materials: Fundamentals and Applications*, volume 239 of *NATO ASI Series E: Applied Sciences*, page 37, Dordrecht, 1993. Kluwer Academic Publishers.

[134] F. Grey, D. Huang, and M. Aono. The sound of one atom hopping: atomic manipulation on silicon surfaces by STM. *Phil. Mag. B*, 70(3):711, 1994.

[135] S. Hosaka, S. Hosoki, T. Hasegawa, H. Koyanagi, T. Shintani, and M. Miyamoto. Fabrication of nanostructures using scanning probe microscopes. *J. Vac. Sci. Technol. B*, 13(6):2813, 1995.

[136] T.-C. Shen, C. Wang, G. C. Abeln, J. R. Tucker, J. W. Lyding, Ph. Avouris, and R. E. Walkup. Atomic-scale desorption through electronic and vibrational excitation mechanisms. *Science*, 268:1590, 1995.

[137] P. Avouris. Manipulation of Matter at the Atomic and Molecular Levels. *Acc. Chem. Res.*, 28:95, 1995.

[138] D. Huang, F. Grey, and M. Aono. Role of Diffusion in Atomic Manipulation on Silicon by Scanning Tunneling Microscope. *Jpn. J. Appl. Phys.*, 34:3373, 1995.

[139] C. T. Salling. Direct patterning of Si(001) surfaces by atomic manipulation. *J. Vac. Sci. Technol. B*, 14:1322, 1996.

[140] T.-C. Shen and P. Avouris. Electron stimulated desorption induced by the scanning tunneling microscope. *Surf. Sci.*, 390:35, 1997.

[141] D. H. Huang and M. Aono. STM atom manipulation with different material tips. *J. of Surf. Analysis*, 3(2):264, 1998.

[142] G. Dujardin, A. Mayne, O. Robert, F. Rose, C. Joachim, and H. Tang. Vertical manipulation of individual atoms by a direct STM tip-surface contact on Ge(111). *Phys. Rev. Lett.*, 80(14):3085, 1998.

[143] D. M. Eigler, C. P. Lutz, and W. E. Rudge. An atomic switch realized with the scanning tunnelling microscope. *Nature*, 352:600, 1991.

[144] D. Eigler. Atom manipulation with the scanning tunneling microscope. In Ph. Avouris, editor, *Atomic and Nanometer-Scale Modification of Materials: Fundamentals and Applications*, volume 239 of *NATO ASI Series E: Applied Sciences*, page 1, Dordrecht, 1993. Kluwer Academic Publisher.

[145] G. Meyer and K.-H. Rieder. Controlled manipulation of single atoms and small molecules with the scanning tunneling microscope. *Surf. Sci.*, 377-379:1087, 1997.

[146] C. Joachim, P. Sautet, and P. Lagier. The tip apex structure of the Eigler atomic switch. *Europhys. Lett.*, 20(8):697, 1992.

[147] Ch. Girard, X. Bouju, and C. Joachim. Van der waals interactions between an adsorbate and the tip of an STM. *Chem. Phys.*, 168:203, 1992.

[148] C. Joachim, X. Bouju, and C. Girard. The Eigler Xe switch: its atomic structure from Xe energy minimization and STM image calculations. In V. T. Binh, N. Garcia, and K. Dransfeld, editors, *Nanosources and Manipulations of Atoms Under High Fields and Temperatures: Applications*, volume 235 of *NATO ASI Series E: Applied Sciences*, page 1, Dordrecht, 1993. Kluwer Academic Publisher.

[149] N. Lang. Field-induced transfer of an atom between two closely spaced electrodes. In Ph. Avouris, editor, *Atomic and Nanometer-Scale Modification of Materials: Fundamentals and Applications*, volume 239 of *NATO ASI Series E: Applied Sciences*, page 87, Dordrecht, 1993. Kluwer Academic Publishers.

[150] T. T. Tsong and C.-S. Chang. High field effects and methods useful for transferring atoms in scanning tunneling microscope. *Jpn. J. Appl. Phys.*, 34:3309, 1995.

[151] A. Buldum and S. Ciraci. Controlled lateral and perpendicular motion of atoms on metal surfaces. *Phys. Rev. B*, 54(3):2175, 1996.

[152] K. Stokbro, C. Thirstrup, M. Sakurai, U. Quaade, Ben Yu-Kuang Hu, F. Perez-Murano, and F. Grey. STM-induced hydrogen desorption via a hole resonance. *Phys. Rev. Lett.*, 80(12):2618, 1998.

[153] P. Zeppenfeld, C. P. Lutz, and D. M. Eigler. Manipulating atoms and molecules with a scanning tunneling microscope. *Ultramicroscopy*, 42-44:128, 1992.

[154] L. Bartels, G. Meyer, and K.-H. Rieder. Basics steps of lateral manipulation of single atoms and diatomic clusters with a scanning tunneling microscope tip. *Phys. Rev. Lett.*, 79:697, 1997.

[155] P. H. Beton, A. W. Dunn, and P. Moriarty. Manipulation of C60 molecules on a Si surface. *Appl. Phys. Lett.*, 67(8):1075, 1995.

[156] T. Junno, K. Deppert, L. Montelius, and L. Samuelson. Controlled manipulation of nanoparticles with an atomic force microscope. *Appl. Phys. Lett.*, 66(26):3627, 1995.

[157] T. A. Jung, R. R. Schlittler, J. K. Gimzewski, H. Tang, and C. Joachim. Controlled room-temperature positioning of individual molecules: Molecular flexure and motion. *Science*, 271:181, 1996.

[158] M. T. Cuberes, R. R. Schlittler, and J. K. Gimzewski. Room-temperature repositioning of individual C_{60} molecules at Cu steps: Operation of a molecular counting device. *Appl. Phys. Lett.*, 69(20):3016, 1996.

[159] M. T. Cuberes, R. R. Schlitter, and J. K. Gimzewski. Manipulation of C_{60} molecules on Cu(111) surfaces using a scanning tunneling microscope. *Appl. Phys.A*, 66:S669, 1998.

[160] C. Baur, A. Bugacov, B. E. Koel, A. Madhukar, N. Montoya, T. R. Ramachandran, A. A. G. Requicha, R. Resch, and P. Will. Nanoparticle manipulation by mechanical pushing: Underlying phenomena and real-time monitoring. *Nanotechnology*, 9:360, 1998.

[161] S. Jay Chey, L. Huang, and J. H. Weaver. *Phys. Rev. B*, 59:16033, 1992.

[162] X. Bouju, C. Joachim, and C. Girard. Single adatom motion during a lateral STM manipulation. *Phys. Rev. B*, 59, 1999.

[163] L. J. Whitman, J. A. Stroscio, R. A. Dragoset, and R. J. Celotta. Manipulation of adsorbed atoms and creation of new structures on room-temperature surfaces with a scanning tunneling microscope. *Science*, 251:1206, 1991.

[164] G. Meyer, L. Bartels, S. Zöphel, and K.-H. Rieder. *App. Phys. A*, 68:125, 1999.

[165] L. Pizzagalli, J.C. Okon, and C. Joachim. Moving a silver atom on a Si(001) surface with a Au tip ? *Surf. Sci. Letters*, 384:L852, 1997.

[166] L. Pizzagalli and A. Baratoff. Theory of single atom manipulation with a scanning probe tip: force signatures, constant-height and constant-force scans. *unpublished.*

[167] U. Koehler et al. *JVST*, A7:2860, 1989.

[168] T. Hasegawa, M. Kohno, S. Hosika, and S. Hosoki. *JVST*, B12:2078, 1994.

[169] K. Cho and E. Kaxiras. *Surf. Sci.*, 396:L261, 1998.

[170] Ruben Pérez, Michael C. Payne, Ivan Štich, and Kiyoyuki Terakura. Role of covalent tip-surface interactions in non-contact atomic force microscopy on reactive surfaces. *Physical Review Letters*, 78(4):678, Jan 1997.

[171] A. Abdurixit, A. Baratoff, and E. Meyer. *Applied Surface Science*, 157(4):355, April 2000.

[172] Thomas Bonner. *Rechnungen zur Kraftmikroskopie auf selbstorganisierenden Monoschichten*. PhD thesis, Institute of Physics, University of Basel, 1998.

Publications and Presentations

Publications

- "Progress on studies of quantum multistep theory", Z.-D. Su, A. Abdurixit, T.-G. Cao, Chinese Journal of Nuclear Physics 18, 182(1996)

- "Transition between the P and Q chains in FKK theory", A. Abdurixit, Z.-D. Su and T. Osman, International Conference on Nuclear Data for Science and Technology, edited by G. Reffo, A. Ventura and C. Grandi (Italian Phys. Soc, Bologna, Italy, 1997) p. 296

- "Tight-Binding Linear Scaling Method Applications to Si Surfaces", A. Abdurixit, A. Baratoff and G. Galli, in Modern Research in High Technology and Science, M. Gheni, I. Sheyhidin editors (Tokyo, Japan, 1999), p. 291-302. Also see *http://arxiv.org/abs/cond-mat/0003005*

- "Molecular Dynamics Simulations of Dynamic Force Microscopy: Applications to the Si(111)-7x7 Surface", A. Abdurixit, A. Baratoff and E. Meyer, Applied Surface Science 157, 355(2000). Also see *http://arxiv.org/abs/cond-mat/0003004*

- "Low Temperature Scanning Force Microscopy of the Si(111)-7x7 Surface" M. A. Lantz, H. J. Hug, P. J. A. van Schendel, R. Hoffman, S. Martin, A. Baratoff, A. Abdurixit, H.-J. Güntherodt and Ch. E. Gerber , Physical Review Letters 84, 2642 (2000)

- "Separation of Interactions by Non-contact Force Microscopy" M. Guggisberg, M. Bammerlin, Ch. Loppacher, O. Pfeiffer, A. Abdurixit, V. Barwich, R. Bennewitz, A. Baratoff, E. Meyer, and H.-J. Güntherodt, Physical Review B. 61, 11151 (2000)

- "True Atomic Resolution Force Imaging with Chemically Inert Tip" A. Abdurixit, M. A. Lantz, H. J. Hug, A. Baratoff, Ch. Loppacher, P. J. A. van Schendel, R. Hoffman, P. Kappenberger, S. Martin and H.-J. Güntherodt, (unpublished)

- "Computing images of the Si(111)-7x7 surface in different atomic force miroscopy modes", A. Abdurixit and A. Baratoff, in preparation

Oral Presentations and Posters

- "Perturbation Theory of Large-Amplitude Dynamic Force Microscopy", A. Baratoff, A. Abdurixit, First International Workshop on Non-Contact Atomic Force Microscopy, Osaka University (Japan), July 22 1998.

- "Theory and Issues of Large-Amplitude Dynamic Force Microscopy", A. Baratoff and A. Abdurixit, SXM3, 3^{rd} Conference on Development and Technological Application of Nearfield-Scanning Probe Methods, University of Basel, September 15, 1998.

- "Atomic-Scale Variations of Damping in Non-Contact Atomic Force Microscopy", T. Bonner, A. Baratoff, A. Abdurixit, and E. Meyer, SXM3, 3^{rd} Conference on Development and Technological Application of Nearfield-Scanning Probe Methods, University of Basel, September 16, 1998

- "Separation of Interactions in Large-Amplitude Dynamic Force Microscopy", M. Guggisberg, M. Bammerlin, A. Baratoff, O. Pfeiffer, Ch. Loppacher, A. Abdurixit, R. Bennewitz, E. Meyer, and H.-J. Güntherodt, SXM3, 3^{rd} Conference on Development and Technological Application of Nearfield-Scanning Probe Methods, University of Basel, September 16, 1998.

- "Atomic-Scale Variations of Damping in Noncontact Atomic Force Microscopy", T. Bonner, A. Abdurixit, A. Baratoff, and E. Meyer,3^{rd} Workshop on Nanoscience, Hasliberg, October 14, 1998.

- "Contributions of Different Interactions in Large-Amplitude Dynamic Force Microscopy", M. Guggisberg, M. Bammerlin, A. Baratoff, O. Pfeiffer, Ch. Loppacher, A. Abdurixit, R. Bennewitz, E. Meyer, and H.-J. Güntherodt, 3^{rd} Workshop on Nanoscience, Hasliberg, October 14, 1998.

- "Applications of the Linear-Scaling Tight-Binding Method to Silicon Surfaces", A. Abdurixit, A. Baratoff, and G. Galli, Poster presented at 9^{th} International Workshop on Computational Materials Science: Electronic Structure Theory and Simulations, Trieste (Italy), January 14, 1999.

- "Molecular Dynamics Study of Dynamic Force Microscopy on the Si(111)-7x7 Surface", A. Abdurixit, T. Bonner, A. Baratoff, and E. Meyer, 10^{th} International Conference on Scanning Tunneling Microscopy/Spectroscopy and Related Proximal Probe Microscopy, Seoul (South Korea), July 20, 1999.

- "Atomic-Scale Variations of Damping in Non-Contact AFM", A. Abdurixit and A. Baratoff, 2^{nd} International Workshop on non-contact Atomic Force Microscopy, Pontresina, September 1 1999.

- "Molecular Dynamics Simulations of Dynamic Force Microscopy", A. Baratoff and A. Abdurixit, 2^{nd} International Workshop on non-contact Atomic Force Microscopy, Pontresina, September 2 1999.

- "Molecular Dynamics Study of Dynamic Force Microscopy on the Si(111)-7x7 Surface", A. Abdurixit, T. Bonner, A. Baratoff, and E. Meyer, Swiss-US Nanoforum, Zurich, September 20 1999.
- "Computing images of the Si(111)-7x7 surface in different atomic force miroscopy modes", A. Abdurixit and A. Baratoff, 18th General Conference of the Condensed Matter Division of the European Physical Society, Montreux, Switzerland, 13-17 March 2000.
- "Structures of Silicon surfaces and model AFM tips from O(N) tight-binding calculations", A. Abdurixit and A. Baratoff, 18th General Conference of the Condensed Matter Division of the European Physical Society, Montreux, Switzerland, 13-17 March 2000.
- "Efficient Molecular Dynamics Simulations of Atomic Force Microscopy", A. Baratoff and A. Abdurixit, 18th General Conference of the Condensed Matter Division of the European Physical Society, Montreux, Switzerland, 13-17 March 2000.

Curriculum Vitae

Abduxukur Abdurixit

25.9.1970	Born in Kuqa, Xinjiang Uyghur Autonomous Region, P. R. China Parents: Abdurixit Nur and Aymisahan Kadir
9.1977-7.1982	No.1 Elementary school in Kuqa
9.1982-7.1988	No.1 Middle school in Kuqa
9.1988	Begun university study at Physics department, Xinjiang University in Urumqi, Xinjiang, P.R.China
7.1993	Bachelor of Science
9.1993	Begun study for master of science degree at Physics department of Xinjiang University
7.1996	Master of Science
9.1996	Begin Diploma Course at International Center for Theoretical Physics (ICTP) in Trieste, Italy
9.1997	ICTP Diploma in Condensed Matter Physics
12.1997	Started PhD research at Department of Physics and Astronomy, University of Basel, Switzerland
7.2000	PhD in Condensed Matter Physics at Department of Physics and Astronomy, University of Basel, Switzerland

Folgenden Dozentinnen und Dozenten der Xinjiang University A), International Center for Theoretical Physics B) und der Universitaet Basel C) verdanke ich meine Ausbildung:

A) Turdi Osman, Zongdi Su, Chaozheng Zha, Weicheng Huang, Guangyao Ren, Rizwan, Shawket, Ghappar Gheni, Mahmutjan Obol, Burhan, Perwin.
B) S. R. Shenoy, A. Baldereschi, J. Kohanoff, G. Pastori, I. Krive, Yu Lu, M. Tosi, A. Mookerjee, A. Nersesiyan, I. Vilfan, H. Cerderia, V. Kravtsov, S. Fantoni, H. Cerderia.
C) A. Baratoff, E. Meyer, H.-J. Güntherodt, Ch. Bruder, Ch. Schönenberger.